Reconstructive imaging based on indirect measurements

Boonzajer Flaes, D.E.

2019

document version
Publisher's PDF, also known as Version of record

RECONSTRUCTIVE IMAGING BASED ON INDIRECT MEASUREMENTS

BY

DIRK EWOUD BOONZAJER FLAES

This thesis has been reviewed by: prof.dr. H.P. Urbach
prof.dr. A.P. Mosk
prof.dr. W. Ubachs
prof.dr. C. Moser
dr. I. Akca

Reconstructive imaging based on indirect measurements

Cover design by Jip de Vries.

Printed by Ipskamp Drukkers.

VRIJE UNIVERSITEIT

Reconstructive imaging based on indirect measurements

From lensless imaging to waveguide analysis

ACADEMISCH PROEFSCHRIFT

ter verkrijging van de graad Doctor aan
de Vrije Universiteit Amsterdam,
op gezag van de rector magnificus
prof.dr. V. Subramaniam,
in het openbaar te verdedigen
ten overstaan van de promotiecommissie
van de Faculteit der Bètawetenschappen
op maandag 11 juni 2019 om 13.45 uur
in de aula van de universiteit,
De Boelelaan 1105

door

Dirk Ewoud Boonzajer Flaes

geboren te Amsterdam

promotor: prof.dr. J.F. de Boer
copromotor: dr. S.M. Witte

CONTENTS

1 INTRODUCTION

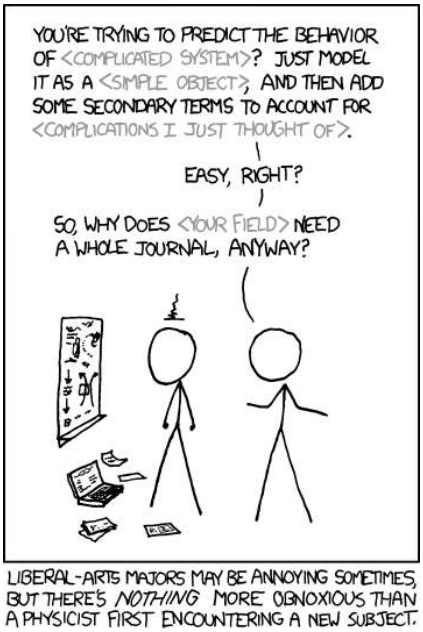

Fig. 1.1: Description of most physicist's reflex to dealing with a new problem. Cartoon courtesy of xkcd.com.

When encountering a new problem, the first instinct of a physicist is to actively look for properties that can be ignored, thus simplifying the problem to an extension of areas well understood. Afterwards, depending on the required level of accuracy, the effect of these properties of less importance can be incorporated again. This more or less standard approach is helpful in solving a lot of different types of problems, although it might lead to new challenges, as shown in Fig. 1.1. An important challenge for the physicist is therefore, to find out which parameters are important to understanding the behavior and which ones are not, thus allowing to make assumptions that simplify the model without ignoring significant effects. Basically - what can we leave out while still accurately analyzing the problem.

In optics - the field of study of this dissertation - most experiments can be performed in a lab with precise control over the experimental conditions. Whenever possible, a setup is built in which results can be measured in the most accurate and direct way possible. In a restricted number of cases,

building a setup capable of controlling all parameters of the experiment is not feasible, either due to more fundamental constraints, such as that the required optical components do not exist or that the quantity cannot be measured directly, or simply because the required space for such an optical system is not available. This is where alternative approaches have to be explored.

In this thesis, we will follow such an alternative approach. Rather than making use of an experimental setup capable of controlling all experimental parameters of interest, indirect measurements of complicated objects are taken with very simple optical setups, usually no more complicated than a laser, a sample and a camera. General knowledge about the object under investigation combined with accurate knowledge about light propagation then allow the experimenter to reconstruct the results based on these indirect measurements, without requiring the degree of control that is usual. The simplicity of the optical setup now becomes a feature as it enables modeling light propagation through the setup. One might liken this approach to a form of reverse engineering.

In part one of this dissertation, we apply these principles to building small and versatile microscopes based on a minimal number of optical elements. In part two of this dissertation, similar principles are applied to study light propagation through a graded-index multimode waveguide. The application area that we have in mind is micro-endoscopy. Although both parts of the thesis can be judged as different studies, they share the same measurement philosophy. This short introduction hopefully clarifies this point.

1.1 OUTLINE OF THIS THESIS

Part one of this thesis (chapters 2 through 4) covers lensless microscopy and computational imaging. Instead of building a classical microscope, very simple optical setups are employed that rely heavily on numerical postprocessing to reconstruct the specimen under investigation, rather than creating a direct image of it. In chapter 2, a general introduction is given into lensless microscopy based on illumination at multiple wavelengths, and the underlying algorithms that are used for the reconstruction are explained. Chapter 3 then describes a small and versatile microscope based on Fresnel diffraction at different wavelengths. At the end of this chapter, four unpublished additions are discussed that form the basis of a conceptual three-dimensional tracker with minimal hardware requirements. Finally, in chapter 4, instead of changing the wavelength of the illumination, the spatial structure of the illumination is changed in a modality called ptychography.

Part two of this thesis (chapters 5 through 8) covers minimally invasive endoscopy, especially multi-mode fiber endoscopy. To see inside a patients body, or to perform imaging in harsh environments, it is desirable to have an endoscope with a minimal footprint and a replacable tip. One of the possible designs is employing a multimode optical fiber. A bare fiber is inserted into the patient until the end touches the area of interest. The fiber is then employed to guide the illumination onto the specimen

and to record the back-propagated light onto the sample. The image of the object is not preserved while the light propagates through the fiber. Therefore a characterization is needed to be able to perform imaging. This characterization of the fiber changes when the fiber is bent. This evidently severely limits many possible application areas. We will therefore investigate the feasibility of employing a multi-mode optical fiber with a parabolic refractive index profile, and explain that these fibers are much more resilient to bending. In chapter 5, background information is given on light propagation through a multimode fiber and experimental verification methods. Chapter 6 then covers a study on bending behavior of parabolic index profile waveguides for imaging applications. The supplement of this study can be found in chapter 7 and covers a more detailed description of the performed experiments and details of the derivation in the preceding chapter. The optimization techniques employed in chapter 6 are extended by an unpublished addition covered in chapter 8.

Part I

PHASE RETRIEVAL TECHNIQUES

2

INTRODUCTION TO LENSLESS MICROSCOPY

In the following chapters, we will discuss various forms of lensless microscopy. The conceptual difference between a classical microscope and a lensless microscope is the way in which the object is recorded. A lens-based microscope typically records an intensity image of an object, and lenses are used to transport an image of the light leaving the sample onto a camera or an eyepiece. As such, the recorded image is usually the final result of a recording. In the lensless microscopes which are discussed in this thesis, a camera typically records an image of light that was scattered by a sample and then propagated over a particular distance. Therefore, this is not a direct image of the sample, and it will require postprocessing in order to retrieve the actual image of the object. While in some cases this can be done analytically [1, 2], most reconstruction algorithms rely on iterative techniques [3–8]. In the next chapters, two new forms of lensless microscopy will be demonstrated. This chapter will provide an introduction on lensless microscopy and outline the underlying algorithms that were used to reconstruct the samples in the next chapter.

2.1 LENS-BASED MICROSCOPES

In order to appreciate the differences between a regular lens-based microscope and a lensless microscope, a conceptual diagram of a lens-based and a lensless microscopy setup is shown in Fig. 2.1(a). A complex object (O) is illuminated by a source with electric field P. It is generally useful to separate the complex object transmission into polar coordinates, $O = A_o \exp(\imath\phi_o)$, where A_o represents the real-valued attenuation coefficient and ϕ_o represents the spatial phase retardation of the object. The electric field leaving the object can be written as $\psi = O \times P$, and is called the exit wave. The exit wave is imaged onto a camera or eyepiece using a series of lenses – usually an objective lens f_{MO} and a tube lens f_T – with a magnification $M = f_T/f_{MO}$. The distance between the object and the microscope objective is tuned in such a way that the object is in focus on the camera, usually close to the focal plane of the objective. The magnification can be tuned by swapping the objective lens for a lens with a different magnification. In principle, the tube lens distance could be changed too but this is not employed in commercial microscopes. The full electric field of the magnified exit wave hits the camera. However, as the processing speed of a single camera pixel is slow compared to optical frequencies, the phase information is lost and only the time-averaged intensity of the object is recorded. The intensity is related to the electric field as $I = EE^* = A_E^2$, where I is the intensity, E is an electric field and A_E is the real-valued amplitude of the elec-

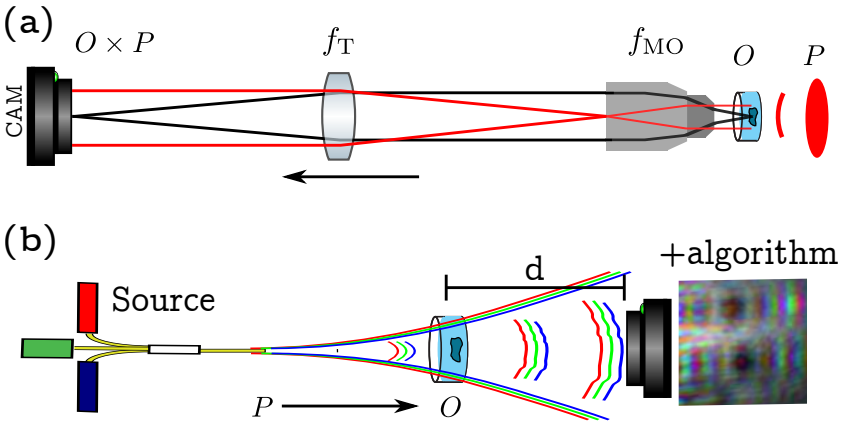

Fig. 2.1: (a) Typical classical microscope, where the object (O) is illuminated by a source (P), and the exit wave is imaged using two lenses, f_{MO} and f_T, onto a detector (CAM). (b) Typical lensless microscope, consisting of a coherent illumination (P) hitting the object (O), and light propagating over a distance d onto a camera where the diffraction pattern is recorded. A point (indicated by the black line) is imaged onto a point on the camera, while a collimated beam is imaged onto a collimated beam (red line). From the diffraction pattern, the sample can be reconstructed using an algorithm. In this case, illumination at different wavelengths is indicated, other measurement diversity schemes can be used as well.

tric field E. Therefore, the phase information is lost. The recorded intensity is now given by

$$I_{\text{meas}} = |O \times P|^2 = \left|\sqrt{I_o I_P}\exp\left(\imath(\varphi_o + \varphi_P)\right)\right|^2 = I_o I_P\,. \tag{2.1}$$

Where I_o, ϕ_o and I_P, ϕ_P are the intensity and phase profiles of the object and illumination beam, respectively, and I_{meas} is the measured intensity. In some cases, intensity information is all that is required to study the object. However, biological samples are usually mostly transparent. Therefore, losing access to the phase information means that information about the structure is lost. It should be noted that this is the most basic form of microscopy. More advanced microscopy techniques, such as Zernike phase contrast [9] or differential interference contrast [10], are sensitive to the phase of the object, although these are not quantitative phase measurements so only an indication of the phase structure is given. In principle, any system with an asymmetric point-spread function will be sensitive to phase information of the object, but not necessarily in a controlled way. For most quantitative phase measurements, multiple measurements are required [11–14].

An interesting intermediate step between phase retrieval and classical microscopy is called digital holography [15], where a single-shot measurement can be used for quantitative phase contrast measurements at the expense of resolution or based on a more complicated setup. It will be discussed after the next section.

2.2 LENSLESS MICROSCOPES

Consider a typical lensless microscope, shown in Fig. 2.1(b). An object O is illuminated with a coherent illumination beam P. The exit wave propagates through the air over a distance d onto a camera, where the intensity is recorded. Throughout this thesis, we will only consider setups where the object is relatively close to the camera. This can be quantified by the so-called Fresnel Number, defined as:

$$F = \frac{a^2}{d\lambda}, \tag{2.2}$$

where a is the largest feature size, d is the propagation distance and λ is the wavelength of the incident light. In the regime where we will operate, F is typically larger than one, and as such we operate in what is called the *Fresnel regime*. In the Fresnel regime, the measured intensity distribution still roughly resembles the object, even though it appears to be out of focus. If the full electric field is known in a particular plane, the electric field of the light after propagating a distance z can be modeled using the angular spectrum method. In case of coherent light at a single wavelength, light transport can be as follows: (Eq. 3-74 in Ref. [16])

$$\begin{aligned} E(x,y,z) &= \mathcal{P}_{\lambda z}\left[E(x,y,0)\right] \\ &= \mathcal{F}^{-1}\left[\mathcal{F}\left[E(x,y,0)\right]\exp\left[\imath 2\pi\frac{z}{\lambda}\gamma(\lambda,f_x,f_y)\right]\right] \end{aligned} \tag{2.3}$$

$$\gamma(\lambda,f_x,f_y) = \sqrt{1-(\lambda f_x)^2-(\lambda f_y)^2} \tag{2.4}$$

Here, $E(x,y,z)$ describes the electric field at a distance z from the origin, the operator $\mathcal{P}_{\lambda z}[\cdot]$ describes propagation over a distance z at wavelength λ, and $\mathcal{F}[\cdot]$ describes a Fourier transform along x and y, and f_x and f_y are the spatial frequencies. From a numerical point of view, Eq. (2.3) is readily implemented using the Fast Fourier Transform (FFT). It should be noted that in order to properly predict the electric field in a different plane, the full electric field has to be known. Therefore, the recorded intensity in a plane away from the object will be dependent on the transmission as well as the phase retardation of the object. An example of the behavior of Eq. (2.3) is shown in Fig. 2.2. Two objects with an identical amplitude but a different phase profile are propagated over a range of distances, and we simulate the recorded intensity profile. First of all, it is apparent that the amplitude distribution at the object plane plays an important role in the recorded intensity profile after some propagation. Furthermore, even though the object appears to be "out of focus", the large features are still visible. Lastly, when propagating to different planes, the intensity distribution changes in a complicated way. When the propagation distance is large, leading to Fresnel numbers much smaller than one, the effect of additional propagation is simply a scaling in transverse size. Therefore, recording far-field diffraction patterns at different propagation distances will not yield additional information, while recording diffraction patterns at different propagation distances in the Fresnel regime could provide additional information about the object.

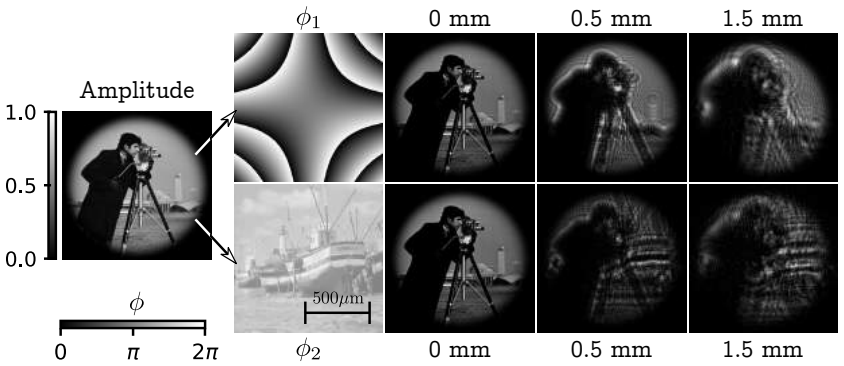

Fig. 2.2: Simulation of light propagating in the Fresnel regime. Two electric fields with an identical amplitude distribution but a different spatial phase profile (ϕ_1, top row and ϕ_2, bottom row) are propagated over a range of distances and the resulting intensity of the diffraction pattern is shown. At the sample ($0\,\mathrm{mm}$), the simulated intensities are identical. The amplitude and phase couple already after propagating $500\,\mu\mathrm{m}$, leading to an intensity profile that is dependent on the phase of the object. At longer propagation distances the resemblance between the original object and the diffraction pattern decreases. Simulation parameters are: wavelength: $405\,\mathrm{nm}$, pixel size: $2.2\,\mu\mathrm{m}$, number of pixels per dimension: 512. The extent of the entire image is $1.1\,\mathrm{mm}$. Image used for phase image ϕ_2 was taken from the USC-SIPI Image Database.

The lensless imaging techniques that we will consider rely on recording multiple intensity patterns of illuminations with different characteristics to reconstruct the electric field of the object on the camera. For instance, the spatial profile or the wavelength of the illuminating light can be altered. Afterwards, the estimate of the object can be retrieved employing Eq. 2.3 to back-propagate the reconstructed electric field onto the object.

A special technique called holographic microscopy should be mentioned, which is an intermediate form between regular microscopy and quantitative phase contrast microscopy. In holography, the electric field of the light hitting a detector is measured in amplitude and phase, after which it can be back-propagated to any plane. In order to be sensitive to the phase of the object, a reference beam can be used in a modality called off-axis holography [17, 18]. The relative phase of the reference beam with respect to the object beam can be stepped in order to reconstruct the phase of the object beam, requiring multiple measurements. Alternatively, the reference beam can be put under an angle with respect to the object beam, leading to an interference pattern. A frequency-domain spatial filtering technique is employed in order to retrieve the electric field. In principle, this only requires a single exposure but unless a advanced optical setups are used it comes at the expense of a factor two in resolution [19]. In the first holographic applications, an empty part of the illuminating beam was used as a reference [20]. The measured diffraction pattern was then back-propagated to a sample plane. This requires just a single illumination, but a twice as defocused image remained visible, essentially because the phase information of the electric field was lost. We

call this defocused background the twin-image. Alternatively, optimization techniques can be used to reconstruct the object [21], usually employing prior knowledge of the object. The reconstruction algorithm that we will use requires three of these inline holograms in order to eliminate the twin image.

2.3 RECONSTRUCTION ALGORITHMS

To reconstruct the object, a technique is required to reconstruct the phase of the electric field on the camera based on the recorded intensity measurements. This is a problem that is known in general as phase retrieval, and it has been used for a wide range of different applications, ranging from beam shaping to the design of antireflection coatings, an overview of which has been given by for instance by Fienup [22]. More recent applications range from imaging through scattering media [23–25] to protein folding and solving a Sudoku puzzle [26]. Unless some stringent assumptions are made about the object, for instance that it is an intensity-only object [27, 28], more than one measurement is generally required in order to uniquely reconstruct the object of interest. The problem is typically formulated as finding the intersection of a set of constraints represented by the different measurements and knowledge about the object.

In chapter 3, we demonstrate a lensless imaging setup where the sample is illuminated with multiple wavelengths, previously published in Optics Express [29]. The phase retrieval algorithm employed to reconstruct the objects - which is only broadly discussed in the publication - is explained in the next section. In chapter 4 we consider a setup which relies on modulating the spatial structure of the illumination beam, in a modality closely related to ptychography [30–33].

2.3.1 *Multi-wavelength phase retrieval*

In order to acquire the input data for the algorithm, a sample is illuminated with coherent laser light at multiple wavelengths. A camera placed a distance d from the camera records the resulting diffraction patterns, see Fig. 2.3(a). An RGB detector is used to detect the diffraction patterns at three different wavelengths in a single shot. As visible in Eq. (2.3), the electric field is dependent on λz. Therefore, as long as the sample is not strongly wavelength-dependent, the measured intensity patterns at different wavelengths closely resemble the measured intensity patterns that would be measured for different propagation distances. Previous work has shown that diffraction patterns at multiple propagation distances are sufficient to reconstruct an object uniquely using various techniques [2, 34]. The advantages of using multiple illumination wavelengths instead of using multiple propagation distances are that no physical scanning is required, and when a color camera and suitable wavelengths are used, a single-shot measurement can be performed, opening up possibilities for imaging of living specimen or otherwise dynamic samples.

To reconstruct the object from the recorded intensities, object constraints are

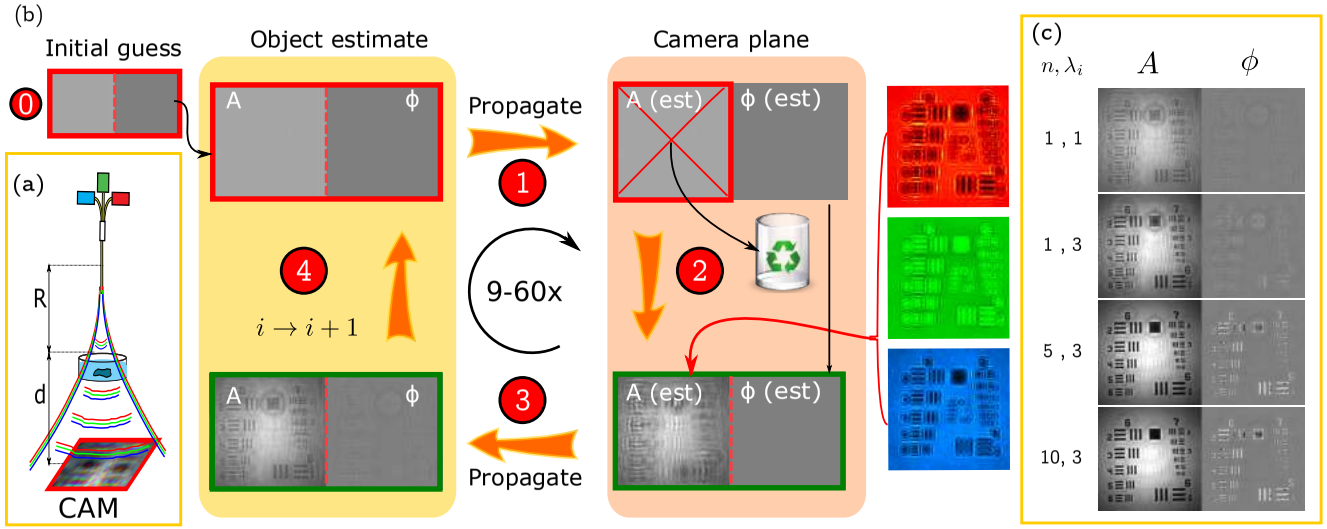

Fig. 2.3: (a): Optical setup. A sample is illuminated with coherent light at three different wavelengths, and the diffraction pattern is recorded at a distance d from the camera. (b): (middle part): multi-wavelength reconstruction algorithm. As an initial guess of the object, unit intensity and a flat phase are used (⓪). The estimate is propagated to the camera (①) at wavelength λ_i. The amplitude of every pixel is scaled in such a way that the expected intensity matches the measured intensity. The phase estimate on the camera plane is kept (②). The corrected field is back-propagated to the object plane, leading to a better estimate of the object (③). The wavelength index is changed to the next wavelength (④) and the procedure is repeated. After all wavelengths have been processed (a full RGB iteration) steps ① – ④ are repeated. (c): Object estimates for different number of iterations, where the first index describes the number of RGB iterations and the second index the number of wavelengths that have been processed for that iteration.

required based on which an algorithm can be derived. Object constraints can either be represented by *a priori* knowledge of the sample, or measured diffraction patterns. The first constraint that we apply is that the spatial structure of the object is independent of the illumination wavelength. Strictly speaking, this is not a correct assumption as even for a sample that is wavelength-independent, the expected phase retardation is related to the optical thickness of the sample which is wavelength dependent. Nevertheless, most samples under consideration are very thin and as such this is still a reasonably accurate assumption. Next, when the exit wave is propagated from the object onto the camera, the modeled intensity pattern on the camera should match the measured intensity pattern for all wavelengths, posing an three additional constraints. The latter constraints are called modulus constraints. If these four constraints are sufficiently strong, there will only be a single solution which will result in an accurate estimate of the object.

Based on these constraints to our solution, an algorithm can be used to reconstruct the object. There is quite a range of different algorithms that are capable of doing such a reconstruction. We will use one of the earliest methods, which is conceptually relatively easy to understand even. Other algorithms might converge faster and are better at avoiding local minima. It is called the Gerchberg-Saxton algorithm, or the error-reduction algorithm and it consists of applying the different constraints sequentially in either the camera plane or the object plane. The error, defined as the difference between the expected intensity on the camera and the measured intensity, will either stay the same or decrease with every iteration [3, 35]. However, in general, this algorithm is prone to get stuck in local minima or stagnate [36], even though we have never observed this in our experiments, which is an indication that we have relatively strong constraints. Other methods, which are specifically designed to finding a global optimum, such as the input-output algorithm [22] or the difference map algorithm [7] could also be adopted, but were not investigated here. Lastly, an interesting alternative reconstruction approach employs the transport of intensity equation [34], which was demonstrated for a setup using a series of defocused images obtained with a microscope. The reconstruction algorithm that we employed was developed independently by Bao et al [37] and by Noom et al [38], applying it to biological samples for the first time.

2.3.2 *Error-reduction algorithm*

The algorithm is schematically depicted in Fig. 2.3. In this algorithm we presume that all illumination beams have the same uniform intensity. In practice this is not completely accurate and the multiplication of O and smallest illumination beam P is reconstructed. The algorithm can be extended to take into account the spatial structure of the illumination beams [6, 39, 40]. As it was not employed for the reconstructions in the next chapter, it is not discussed here. The algorithm proceeds along the following steps:

1. Start out with a random initial estimate of the object, O, at wavelength λ_i. This is depicted by step (0) in the diagram.

2. The expected electric field for wavelength i on the camera is computed, depicted by step (1):

$$E_{\lambda_i} = \mathcal{P}_{d\lambda_i}\left[O^n_{\lambda_i}\right] \tag{2.5}$$

3. The expected intensity on the camera is computed as:

$$I^{\text{exp}}_{\lambda_i} = \left|E_{\lambda_i}\right|^2 \tag{2.6}$$

4. Now, every pixel in E_{λ_i} is scaled in such a way that the expected intensity matches the measured intensity, applying the i-th modulus constraint. The phase estimate is kept, depicted by step (2):

$$E'_{\text{exp}} = E_{\text{exp}}\sqrt{\frac{I^{\text{meas}}_{\lambda_i}}{I^{\text{exp}}_{\lambda_i}}} \tag{2.7}$$

5. We now have an estimate of the exit wave on the camera that matches the observed intensity at wavelength i, combined with the previous estimate of the phase. The updated expected field on the camera is propagated back to the object, leading to a better estimate of the object, step (3).

$$O'_{\lambda_i} = \mathcal{P}_{-d\lambda_i} E'_{\text{exp}} \tag{2.8}$$

6. Due to the aforementioned amplitude-phase-coupling, correcting the amplitude in the camera plane also affects the phase of the retrieved sample. As per the first constraint, we presume that the object looks the same for the next wavelength, λ_{i+1}, step (4).

$$O_{\lambda_{i+1}} = O'_{\lambda_i} \tag{2.9}$$

7. Steps (1) – (4) are repeated for all wavelengths, arriving at the next object estimate $O^{(n+1)}$
8. All steps are repeated for n iterations.

The object estimate is shown in Fig. 2.3(c), showing that the object estimate improves with more iterations. This algorithm can be written in a very compact way, recognizing that steps (1) – (3) are essentially an update of the object based on a single intensity measurement, which is called applying the modulus constraint. Therefore the algorithm can be compressed into two equations:

$$\mathcal{P}_{\text{mod},\lambda_i}[O] = \mathcal{P}_{-\lambda_i d}\left[\mathcal{P}_{\lambda_i d}[O]\sqrt{\frac{I^{\text{meas}}_{\lambda_j}}{\left|\mathcal{P}_{\lambda_i d}[O]\right|^2}}\right] \tag{2.10}$$

$$O^{(n+1)} = \mathcal{P}_{\text{mod},\lambda_3}\left[\mathcal{P}_{\text{mod},\lambda_2}\left[\mathcal{P}_{\text{mod},\lambda_1}\left[O^{(n)}\right]\right]\right] \quad . \tag{2.11}$$

Here, $O^{(n)}$ denotes the n-th estimate of the object. In practice, the order of the wavelengths is shuffled after every iteration. The algorithm can be sped

up considerably, combining steps (3), (4) and (1). As Eq. (2.3) is linear both in wavelength and in propagation distance, it is possible to propagate directly from the diffraction pattern at wavelength i to the diffraction pattern at wavelength $i+1$:

$$E_{\lambda_{i+1}} = \mathcal{P}_{d,\lambda_{i+1}}\left[\mathcal{P}_{-d,\lambda_i}\left[E_{\lambda_i}\right]\right] = \mathcal{P}_{d(\lambda_{i+1}-\lambda_i)}\left[E_{\lambda_i}\right] \tag{2.12}$$

As a single Fresnel propagation involves computing two fast Fourier transforms (FFT's), which consume the majority of the reconstruction time, this saves about half of the reconstruction time. Usually, a complete retrieval requires a few tens of iterations, where every iteration over all wavelengths takes on the order of 30 ms for an image with 1024×1024 pixels when programmed on a graphics card (GPU), or about 600 ms on a laptop CPU.

This is the basis of the algorithm of which concrete results will be discussed in the next chapter. In the explanation of the algorithm, we presumed that the object-camera distance is known. Currently, this back-propagation distance is chosen by visual inspection. Essentially, the setup records three inline holograms. As the phase information of the object is not yet known, a flat phase is assumed with which the object is back-propagated to a range of distances. The optimal back-propagation distance is chosen by hand, based on image sharpness, similar to the first sub-iteration of the algorithm. Similar to the original paper by Gabor [20], in addition to a sharp image, a defocused twin image appears. This is essentially a manifestation of the fact that the spatial phase profile at the camera is not known. In Section 3.2.1, an automated method to determine the back-propagation distance will be discussed. From this focusing metric, a new reconstruction method naturally appears which will be discussed in Section 3.2.2. Combining this new reconstruction algorithm and the automated focusing, a proof-of-concept three-dimensional tracker for extended objects can be created, which is outlined in Section 3.2.3. Lastly, color cameras are widely available for visible light, but not for other wavelengths. Nevertheless, we found a method to employ a visible-light camera to do near-infrared experiments by careful examination of the coupling of different wavelengths to different color channels, at the expense of increased noise in the reconstruction. In Section 3.2.4, we demonstrate infrared imaging with an RGB camera employing three novel reconstruction algorithms.

2.4 APPLICATIONS OF LENSLESS MICROSCOPY

With the huge amount of different microscopy methods available, the question arises whether there is any need for a lensless microscopy system at all. However, some limitations of lens-based microscopy are so common that they are hardly considered limitations anymore, but rather fundamental limits of microscopy. One of these is that the object under investigation has to be in focus, and as such the focal distance to the microscope objective needs to be known in advance. In some experimental settings the focal plane might not be known in advance. An example would be investigating a live moving

organism, where forcing it to move only in a specific plane might lead to artificial results [41].

In a lensless microscope, the back-propagation distance d is just a parameter of the reconstruction algorithm, and it can be chosen after acquiring the images. Also, as knowledge of the the electric field on the camera is required in order to be able to back-propagate onto the sample, the reconstructed exit wave will have inherent quantitative phase contrast. However, if quantitative phase information is not needed, it can be sacrificed in order to reduce the number of required measurements [28]. Furthermore, the algorithms can be extended to incorporate known features of the object, such as atomicity or the fact that the object is surrounded by an empty region. Furthermore, lensless microscopes generally pose fewer requirements on the optical setup and as such they lend themselves very well for a parallel setup, where lots of different objects can be investigated at the same time. Lastly, for other parts of the spectrum, such as (extreme) ultraviolet, high quality lenses are not readily available, and the methods presented in the next chapters readily extend into other wavelength regimes.

3

MULTI-WAVELENGTH FRESNEL DIFFRACTION IMAGING

Section 3.1 has been published as: "Noom, D. W.*, Boonzajer Flaes, D. E.*, Labordus, E., Eikema, K. S. E., & Witte, S. (2014). High-speed multi-wavelength Fresnel diffraction imaging. Opt. Express, 22(25), 30504–30511" [29]. Only minimal changes have been made to the original text of the publication: the references to supplemental material have been updated and two typos have been corrected.

At the end of the chapter new methods are shown which represent additional methods of processing the same input data and open new opportunities based on a similar principle, but which have not been published yet. Together with a technique to employ a visible-light camera for infrared imaging, these open the way to a new 3D flow-cytometric system or an extremely low-cost object tracker.

3.1 HIGH-SPEED MULTI-WAVELENGTH FRESNEL DIFFRACTION IMAGING

Daniel W.E. Noom, Dirk E. Boonzajer Flaes*,*
Elias Labordus, Kjeld S.E. Eikema and Stefan Witte
* These authors contributed equally.

Abstract

We demonstrate a compact lensless microscope which can capture video-rate phase contrast images of moving objects and allows numerical scanning of the focal distance after recording. Using only an RGB-detector and illumination from a single mode fiber, diffraction patterns at three wavelengths are recorded simultaneously, enabling high-speed data collection and reconstruction of phase and amplitude. The technique is used for imaging of a moving test target, beads in a flow cell, and imaging of *Caenorhabditis elegans* moving in a droplet of liquid.

Compact microscopes consisting of few parts are very desirable for many applications. One can think of microscopy in difficult to reach places or harsh environments, or applications where one would like to employ many microscopes in parallel. It is therefore important to get the most information out of the most basic imaging setups [42–46]. We describe a system for fast lensless phase-contrast microscopy that requires only a three-wavelength source, an RGB-detector and a computer, but is still able to reconstruct the complex refractive index of a sample using images taken in a single shot.

We have already shown that it is possible to use diffraction patterns at three different wavelengths to retrieve phase and amplitude information from a

sample with very little constraints on the imaging setup [38]. That method required multiple images to be taken of a sample while it was illuminated with different wavelengths transmitted through the same optical fiber. Here we show that the method can be used to take single shot images by using an RGB-detector and light sources at suitable wavelengths, thus enabling the imaging of moving objects. Three diffraction patterns are measured at the same time and a few iterations of a phase retrieval algorithm reconstruct the phase and amplitude of the sample.

3.1.1 *Fresnel Diffractive Imaging*

An RGB image detector only measures the intensity at different pixels, but for image reconstruction, the phase is also needed. Retrieval of the phase of the electric field is possible using holographic methods [17], intensity changes in different planes [1], or iterative retrieval algorithms [3]. The change in intensity when the light field propagates, or when the illuminating wavelength changes, depends on the complex phase curvature of the wavefront. This information can be extracted from multiple diffraction patterns using a phase reconstruction algorithm. One way to do this is by recording propagation effects of the diffraction pattern from an object by taking multiple images at different distances [34, 47]. However, in Fresnel diffraction, the distance from the sample to the detector and the wavelength of the illuminating source play a similar role [48, 49]. By measuring diffraction patterns at different *wavelengths* we can measure how the intensity propagates without changing the position of the detector. The requirement for this to work is that the sample has only a limited wavelength dependence of both the refractive index and absorption.

While there are many other algorithms used for phase reconstruction, our multi-wavelength approach requires no additional information and converges robustly for many different samples. The sample does not need to be isolated from its surroundings and we show it can even be a complex target moving in a fluid. The only information required for a reconstruction, except for the images, is the approximate wavelengths of the light used to illuminate the sample. After reconstruction the images can be refocused to any plane because of the quantitative phase information.

3.1.2 *Setup*

To reconstruct an image, we need diffraction patterns at three different wavelengths. With a monochrome image sensor this requires three detected frames, but using an RGB image sensor and suitable laser wavelengths this can be done in a single shot. To get an RGB-source we used fiber-coupled diode lasers at wavelengths of 402 nm, 519 nm and 636 nm, and employed fiber-coupled 50/50 beamsplitters as a simple way of beam combining. While this approach introduced losses, the laser intensities are still high enough to allow fast imaging. The combined beams are coupled into a single mode fiber, which could be directed at a sample. We put our RGB image sensor, an IDS UI-5582LE-C

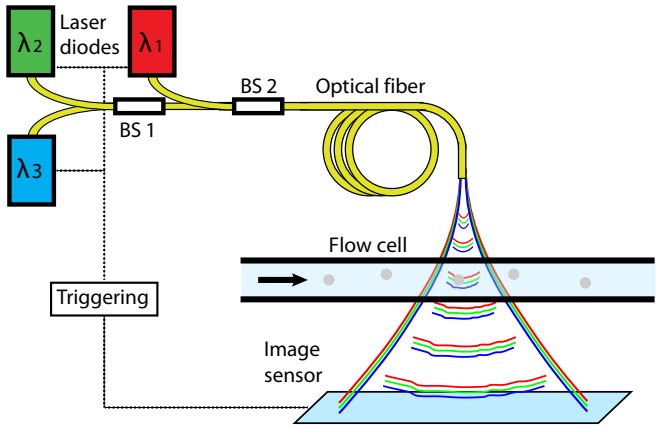

Fig. 3.1: The imaging setup, where a flow cell with beads is taken as an example sample. The wavelengths λ_1, λ_2, λ_3 are obtained from laser diodes at 636 nm, 519 nm, and 402 nm, respectively, coupled in a single-mode fiber. BS: fiber beamsplitter/combiner.

CMOS camera with 2560x1920 pixels of size 2.2 µm and a color depth of 12 bits, after the sample to record diffraction patterns in transmission. A schematic of the setup is shown in Fig. 3.1. Only 3 microwatt of power per wavelength illuminates the sample, which requires an exposure time of 1 ms to achieve image saturation when the image sensor is placed 5 mm from the fiber. To obtain the phase of the electric field from an RGB image, we split the image into its three channels. With the three separate images we then apply the same reconstruction procedure as in Ref. [38].

CMOS sensors require extra care when triggered operation is required. Our chip has a "rolling shutter", where bottom pixel rows stop readout later than top rows. The readout of each horizontal row of pixels can be started simultaneously by using a "global start" option. This means the bottom rows will have a shorter exposure time than the top rows, making it harder to optimize exposure for a good dynamic range and a maximum signal to noise ratio. Furthermore, to reduce motion-induced blurring we want to have the shortest exposure time possible. To meet this demand, and to get an even exposure over the whole chip we pulse the lasers for a much shorter time than the shortest gate time of the CMOS chip. The framerate of the measurements is limited by the readout rate of the camera, and the exposure time for a single frame is limited by the amount of light needed for a good image (typically requiring a laser pulse length of 1 ms).

The algorithm is implemented in Python on a graphics processing unit (GPU) using pyCUDA. A single iteration of the algorithm for an image of 1 megapixel takes about 35 ms on a Geforce GTX780 GPU. Processing the images with two RGB iterations – which suffices for raw alignment - takes 82 ms, including overhead for transferring images from the host to the GPU memory. In theory

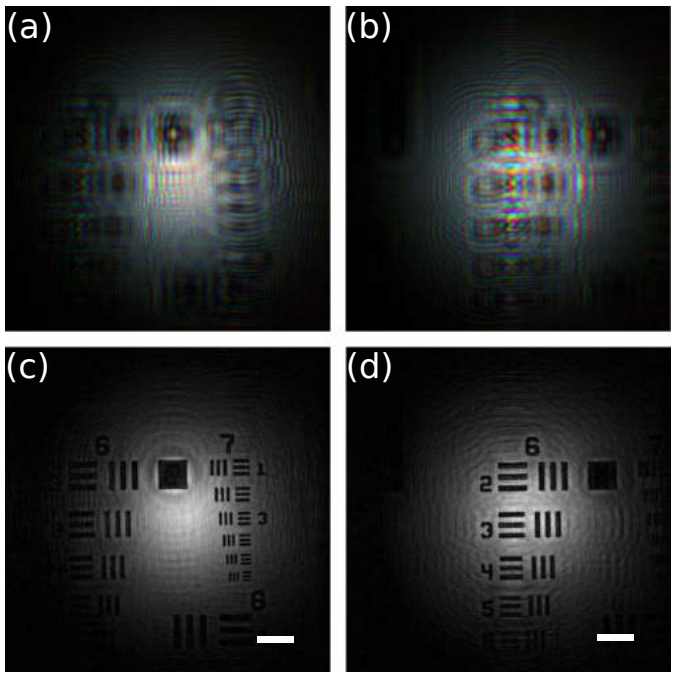

Fig. 3.2: High speed refocusable lensless imaging of a moving USAF test target. (a), (b): Single shot images at different times. (c), (d): Reconstructed image at different times. In (c), the smallest features of group seven, 2.19 µm wide, are clearly visible. The scale bars are 50 µm wide. See Media 1, [50] for the reconstructed video.

this enables reconstruction at 12 Hz. The speed could be further optimized by writing the source in a programming language like C++, or by using a faster graphics card.

3.1.3 *Moving USAF Test Target and beads in a flow cell*

In our first experiment we show images of a fast moving target with high resolution. We mounted a USAF test target on a piezo stage and let it move with a sinusoidal pattern at 0.5 Hz with an amplitude of 100 µm. To achieve a high resolution we put the fiber tip close to the sample so it would be illuminated with a curved wavefront and project an enlarged diffraction pattern on the camera. In Fig. 3.2 we show two frames from the video which was captured at 18.5 Hz. From these images it is clear the movement does not blur the sample significantly, and high resolution images can be rendered at video rate with a lensless setup.

The refocusing ability on moving particles is demonstrated by using beads passing through a flow cell. The height of this flow cell is 1 mm, which exceeds the depth of field of a single refocused image by more than an order of magni-

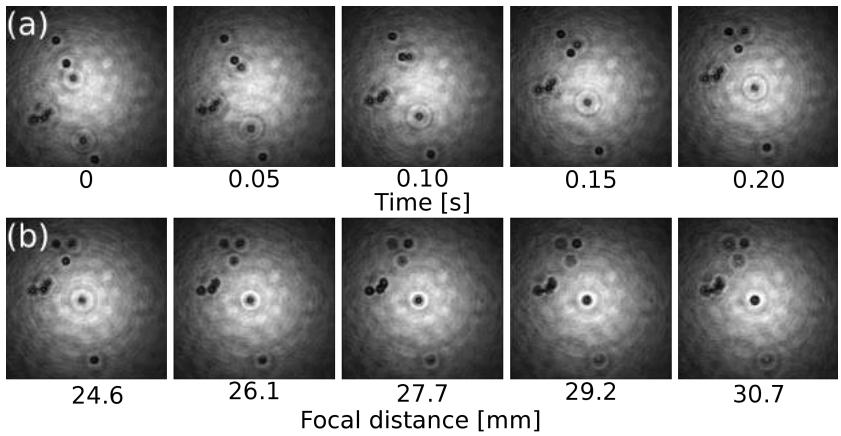

Fig. 3.3: Beads with a diameter of 20 µm in a flow cell. (a) Images at different times at a single focal distance. (b) Images at different focal distances at a single point in time. The indicated focal distances are the numbers that have been used in the phase retrieval algorithm, which correspond to the geometric distance between object and camera scaled by a factor $(1 + d/R)$ because of the finite wavefront curvature (see Discussion section for details). Media 2 [51] shows a video of the moving beads with refocusing at a single time frame.

tude. In Fig. 3.3(a), five different time frames are shown at a single focal distance. Then in Fig. 3.3(b), we show five different focal distances at a single time frame. This shows that our presented method enables a full 2D scan over focal distance and time.

3.1.4 *Refocusable Imaging of C. elegans*

To demonstrate our method in a more complex environment, and make use of the refocusing capabilities, we used a sample of *C. elegans* swimming in a solution, shown in Fig. 3.4. The single-shot measurement is shown in Fig. 3.4(a), where the sample is illuminated with three lasers at the same time. In Fig. 3.4(b), a reconstruction using data obtained with the three wavelengths is shown. In this image, several reconstruction artifacts are visible. Fig. 3.4(c) shows a reconstruction from the same data set, but now using only the red and green wavelength channels. This two-wavelength reconstruction leads to a better image compared to the three-wavelength result. This indicates that the assumption of a small wavelength dependence of the complex refractive index is invalid for this sample. Fig. 3.4(d) shows the reconstructed phase image for the two-wavelength reconstruction. In Figs. 3.4(c,d), it can be seen that not all nematodes are in focus, and Figs. 3.4(e,f) show an amplitude and phase reconstruction at a different focal plane. The obtained phase reconstructions provide quantitative information of the optical thickness of the sample, which is made especially clear by the nematode at the top of the image which is folded back onto itself. With this object, a whole refocusable

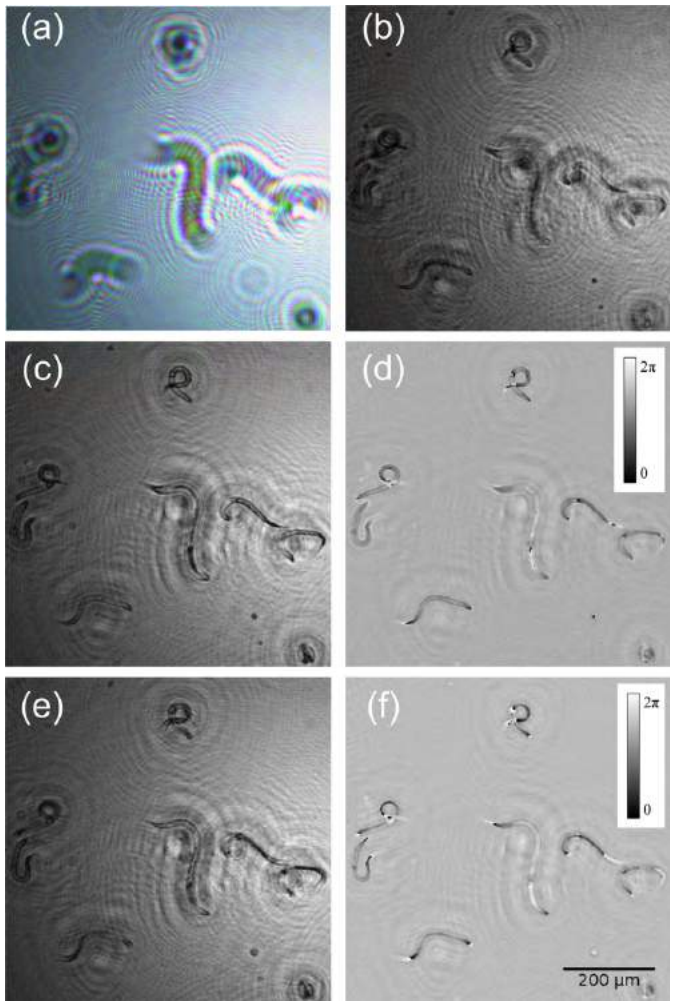

Fig. 3.4: (a) Single shot diffraction pattern of C. Elegans. (b) Reconstructed intensity image using data at three wavelengths as input for the reconstruction algorithm. (c) Reconstructed intensity image using only the red and green wavelength channels. (d) Reconstructed phase image at the same focal distance as (c). (e) Intensity image at different focal plane, using the red and green wavelength channels for reconstruction. (f) Phase image at the same focal distance as (e).

movie has been captured; a video using the two-wavelength reconstruction and the focal distance of Fig. 3.4(c) is shown in Media 3 [52].

3.1.5 *Discussion*

As shown in the previous sections, diffraction imaging using just a single mode fiber as light source and an RGB chip for detection works very well. However, there are a few aspects that need closer inspection. One issue is that the technique requires coherent sources, which also means that diffraction patterns are visible from elements in the image that are not in focus. As a result, anything out of the focus plane will lead to clearly visible spurious diffraction rings in the reconstructed image.

Another potential issue is related to the use of an RGB-detector: pixels of different color are positioned next to each other, and therefore detect slightly shifted diffraction patterns on the scale of a pixel size. Furthermore, the different colored pixels have a significant detection efficiency for more than one source wavelength. However, we have seen no problems with reconstructions up to the smallest structures of our USAF test-sample, which have a width of 2.19 µm. When the detected images at different RGB-channels differ significantly because of effects other than propagation, like a color-dependent absorption and refractive index, it is possible the phase reconstruction fails. In this case, two out of three colors can be used to limit these effects.

Since our microscope geometry involves a curved wavefront for illumination, this curvature should be taken into account in the reconstruction algorithm. An interesting property that we find for the propagated diffraction patterns, is that a given diffraction pattern can either result from an object illuminated with a curved wavefront, or from a scaled version of the object located at a different distance. We looked into this aspect by using ray matrices [53], which have this form:

$$\begin{pmatrix} x_2 \\ x_2' \end{pmatrix} = \begin{pmatrix} A & B \\ C & D \end{pmatrix} \begin{pmatrix} x_1 \\ x_1' \end{pmatrix}, \tag{3.1}$$

where x_1 and x_1' are the input rays' position and slope, respectively, and the outputs of an optical system are given by x_2 and x_2'. If we use a wavefront with radius of curvature R and propagate by a distance d, we get the following matrix equation:

$$\begin{pmatrix} 1 & d \\ 0 & 1 \end{pmatrix} \begin{pmatrix} 1 & 0 \\ \frac{1}{R} & 1 \end{pmatrix} = \begin{pmatrix} 1+\frac{d}{R} & d \\ \frac{1}{R} & 1 \end{pmatrix}. \tag{3.2}$$

This situation is illustrated in Fig. 3.5(a).

We can instead consider a parallel beam of the same size by simulating a infinitesimally small telescope by multiplying the A term with $1+\frac{d}{R}$ and the D term with A^{-1}. If we then propagate by a distance $d(1+\frac{d}{R})$:

$$\begin{pmatrix} 1 & d(1+\frac{d}{R}) \\ 0 & 1 \end{pmatrix} \begin{pmatrix} 1+\frac{d}{R} & 0 \\ 0 & (1+\frac{d}{R})^{-1} \end{pmatrix} = \begin{pmatrix} 1+\frac{d}{R} & d \\ 0 & (1+\frac{d}{R})^{-1} \end{pmatrix}, \tag{3.3}$$

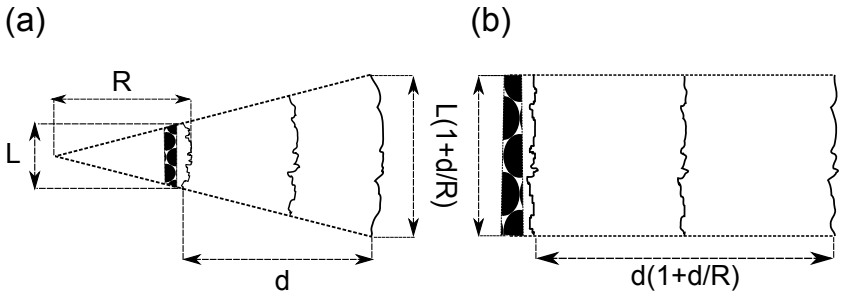

Fig. 3.5: (a) Illumination of a sample of size L with a wavefront with a radius of curvature R and propagation by a distance d, which will have the same intensity distribution as (b), where the sample is illuminated by a flat wavefront and the sample size and propagation distance are magnified by (1+d/R).

we get the same A and B terms in the final matrix, or the same intensity distribution of the beam at the detector plane, illustrated in Fig. 3.5(b). Because of this similarity, the reconstruction will often converge to the latter situation, even though the first situation would describe the experiment. This still yields the correct image, but the true scale needs to be determined from the experimental geometry or a calibration measurement. In practice, we therefore calibrate this scaling factor $(1 + d/R)$ from the recorded images, as this is equivalent to determining the wavefront curvature, but more convenient to implement numerically.

The known size of a sample can be used to calculate the magnification of the objects in focus. For the beads shown in Fig. 3.3 the magnification depends on the distance of the bead to the camera: because of the thickness of the flow cell, individual beads need to be refocused using different propagation distances. This leads to a higher magnification for beads that are further away from the camera. In this experiment, beads are observed with a magnification ranging from 4.1 to 4.4.

3.1.6 *Conclusion*

We have demonstrated a compact lensless microscope, employing a bare RGB-detector and three different illumination wavelengths delivered
through a single-mode fiber, which has the capability to generate refocusable video images of complex objects with better than 2.2 µm resolution and video-like framerate. The exposure time is only limited by the intensity of the illuminating source, which makes it possible to view images of moving samples and live *C. elegans* without motion-induced artifacts. These refocusable video setups can be very useful when size constraints are an issue or when many cameras are to be used simultaneously, which is a situation that is often encountered in high-throughput imaging applications such as imaging flow cytometry. The present lensless RGB microscope can provide an alignment-free, cost-effective solution for various applications in life science and medical

diagnostics.

3.1.7 *Acknowledgments*

This work is supported by the Foundation for Fundamental Research on Matter (FOM), which is part of the Netherlands Organisation for Scientific Research (NWO).

3.2 FURTHER DIRECTIONS BASED ON RGB PHASE RETRIEVAL

In the following sections we present four extensions to the published paper which have not been published yet. We first discuss an autofocusing method, we then show alternative reconstruction algorithms that perform better in case of noise, and we apply this to look at biological samples in the infrared with an RGB detector. Lastly, we integrate the autofocusing method and a new processing algorithm into a conceptual three-dimensional tracker for extended objects.

3.2.1 *Wavelength-diversity based autofocus*

One of the main advantages of lensless microscopy is the freedom to determine the reconstruction distance *a posteriori*, instead of being limited to a particular distance which is set before acquisition. Especially for sparse three-dimensional samples, it can be of great benefit to be able to reconstruct samples at different distances even within a single camera frame, as shown in Secs. 3.1.3 to 3.1.4 on pages 15–16. Nevertheless, most microscopic samples are prepared to be flat. The backfocal distance can be estimated based on an back-focused image at a single wavelength for a sparse sample, such as a USAF resolution target, shown in Fig. 3.6(a_0-c_2) on the facing page. When the sample becomes increasingly dense, this will become much more challenging. For instance, it is difficult to properly predict the optimal back-propagation distance of sample consisting of the root of a lily-of-the-valley (*Convallaria* majalis) based on the back-propagated at a single wavelength alone, shown in Fig. 3.7. Therefore, an automated focusing procedure could be very useful. In this section a promising new approach for automated focusing based on the amount of overlap between back-propagated images at different wavelengths will be presented.

When an image is back-focused, in addition to a sharp image, a blurred twin image appears. The sharp part of the back-focused images should be the same for all wavelengths. Therefore the three images in an RGB measurement will have a large common component. When the object is not in focus, the three different object estimates will be more or less unrelated. When only two images are considered, the cross-correlation between the two images might offer a good metric, but as in this case three images are required, we require a slightly more elaborate approach. As a metric for the focusing quality, we

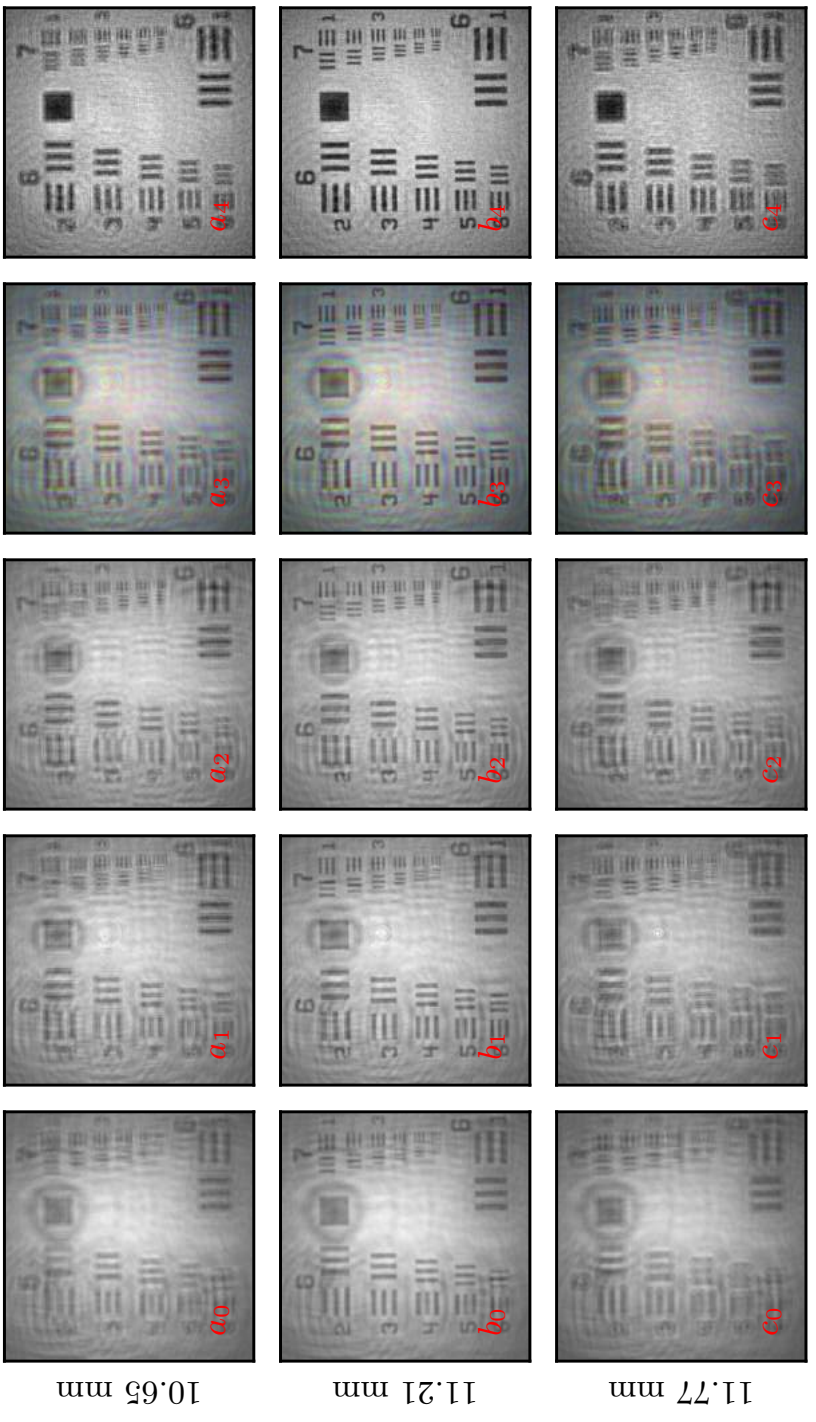

Fig. 3.6: Back-focusing diagram of a USAF target for three different back-propagation distances (10.65 mm, 11.21 mm, and 11.77 mm) shown in rows ($a-c$). The first three columns show back-propagated intensity estimates based on the individual channels of the camera. Column four (RGB) shows the back-propagated images overlayed in the different color channels. Right collumn shows the reconstructed intensity by the phase-retrieval algorithm. In this case, the back-propagation distance can be estimated from any individual image as the sample is sparse and it has clear edges. A larger part of the original image was processed in order not to suffer from edge effects.

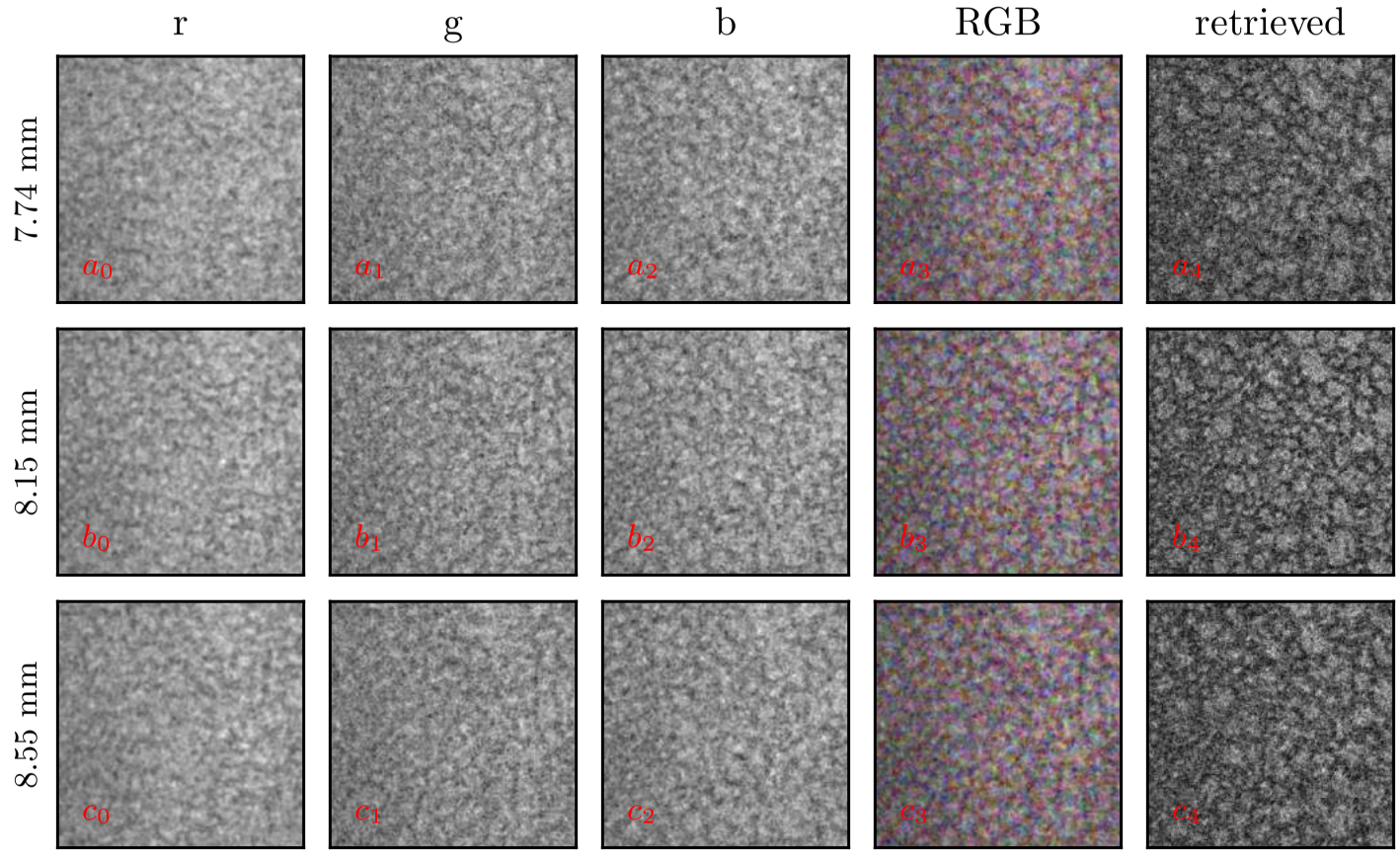

Fig. 3.7: Same as Fig. 3.6, but for a more dense *Convallaria majalis* biological sample. In this case, it is not straightforward to assess the focusing quality from one of the individual images in $a_0 - c_3$.

compute the relative magnitude of the largest singular vector of the three back-focused images. This is a measure indicating how similar the object estimates are, up to an arbitrary intensity scaling, meaning that the method does not rely on illuminating beams with exactly the same intensity. As the singular vector itself is not required, it suffices to compute the eigenvalues of the covariance matrix of all back-propagated images. Therefore, the focusing score p_z for back-propagation distance z can be computed as:

$$Y_z = E_z E_z^T \tag{3.4}$$

$$s_z = \sqrt{\text{eigval}\,(Y_z)} \tag{3.5}$$

$$p_z = s_{z,0} / \sum_i s_{z,i}\,. \tag{3.6}$$

Here, Y_z is the covariance matrix of the three back-propagated images, $\text{eigval}(\cdot)$ is a function returning the eigenvalues of a matrix. s_z are the singular values of E_z. Lastly, p_z is a normalized score between zero and one indicating the amount of signal that can be explained by a single object estimate shared between the three different images, which we presume to be proportional to the focusing quality. E_z is a matrix containing the back-propagated fields of the individually measured diffraction patterns at all wavelengths, back-propagated by distance z, where all the columns have been flattened into a single array, or more explicitly:

$$E_z = \begin{pmatrix} E_{\lambda_1 z}(0,0) & E_{\lambda_2 z}(0,0) & E_{\lambda_3 z}(0,0) \\ \vdots & \vdots & \vdots \\ E_{\lambda_1 z}(0,N_y) & E_{\lambda_2 z}(0,N_y) & E_{\lambda_3 z}(0,N_y) \\ E_{\lambda_1 z}(1,0) & E_{\lambda_2 z}(1,0) & E_{\lambda_3 z}(1,0) \\ \vdots & \vdots & \vdots \\ E_{\lambda_1 z}(N_x,N_y) & E_{\lambda_2 z}(N_x,N_y) & E_{\lambda_3 z}(N_x,N_y) \end{pmatrix} \tag{3.7}$$

Where $E_{\lambda_{1,2,3} z}(x,y)$ is the electric field estimate of pixel (x,y) at wavelength $\lambda_{1,2,3}$ back-propagated by distance z, and N_x and N_y are the number of pixels in the horizontal and the vertical direction.

To demonstrate that the largest singular vector indeed corresponds to the common part in the three back-propagated estimates of the object, all three singular vectors are shown in Fig. 3.8 for two images back-propagated to a distance at which they appear to be in focus. In both cases, the first image clearly seems to contain most of the object features, although the smallest singular vector from the USAF sample seems to contain a few sharp features too.

When attempting to autofocus using our metric, it will have to be evaluated for a range of different trial back-propagation distances. In order to compute this in a fast way, we note that it is possible to significantly speed up computation of s_z. The angular spectrum method, covered in Eq. (2.3) on page 4 involves two Fourier transforms and a multiplication with a phase factor. First of all,

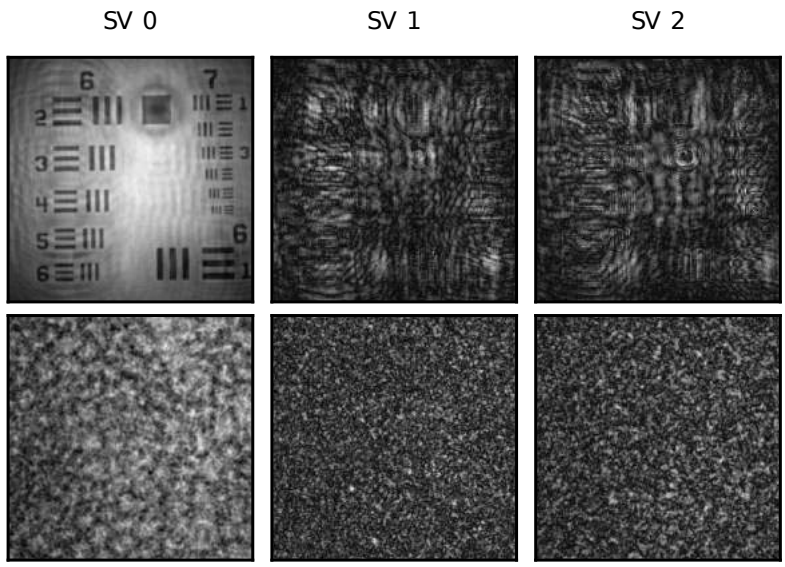

Fig. 3.8: The singular vectors of the USAF (top) and convollaria (bottom) sample, showing that the first singular vector indeed resembles the object whereas the latter two look mainly noisy.

the first Fourier transform can be precomputed once and then kept in memory, so propagation to a different plane only consists of multiplication with a phase factor and an inverse Fourier transform. However, the Fourier transform is a linear operator, and as such the outer Fourier transform in Eq. (2.3) does not affect the result of Eq. (3.6). Therefore it can be omitted when computing s_z. After employing these algorithmic optimizations, finding the optimal back-focusing plane only requires optimizing the steepness of a quadratic phase factor.

Plotting p_z for different samples (Figs. 3.9a and 3.9b) reveals that the metric resembles a monotonic function with a clear global maximum, even for complicated samples where visual inspection makes it difficult to asses the optimal location. In order to find the optimal focal position, we maximize p_z as a function of z. The optimal back-propagation distances in Figs. 3.6 to 3.7 on pages 21–22, row b, were found using our optimization metric, and appear to be perfectly in focus. A bounded optimization search with limits between zero and five centimeters back-propagation distance typically requires only about 10 iterations to find the focus.

One limitation that we encounter is that the area to focus in needs to have small structures. If not, the maximum value of p_z is close to the maximum but not exactly in focus. For samples with relatively large intensity variations, this limitation can be overcome by investigating the back-propagated intensity rather than the electric field, and only looking at edges by introducing a high-pass filtering operation on the intensity images before computing the covariance matrix. However, this will not be a suitable metric for phase-only

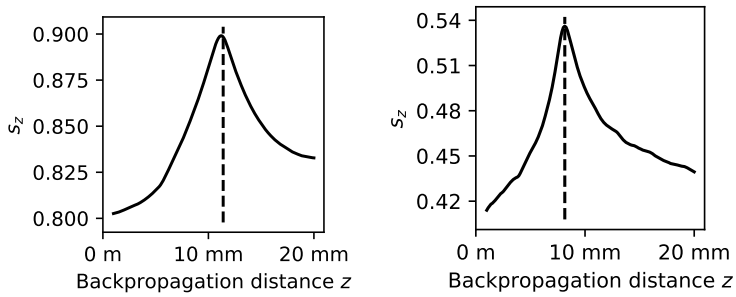

(a) USAF sample (b) Convollaria sample

Fig. 3.9: Performance of the focusing metric defined in Eq. (3.6) for two different samples. The back-propagation distance found by visual inspection is indicated by a vertical dashed line. For the convollaria sample, with a much more complicated structure, the first singular vector has a relatively low power.

samples as there will essentially be no intensity variation in the focus. Also, measuring a reference image with the sample removed and subtracting this from the diffraction pattern seems to improve the accuracy.

Autofocusing for digital holographic microscopy is not a new field, and numerous other metrics exist. An overview of the performance of different metrics for digital holography was given by Ilhan et al. [54]. Most of these techniques rely on setups where the optical phase can be measured using an external reference beam, and as such they do not have to deal with the twin image problem. The performance of our metric compared to other metrics has not been investigated yet. Nevertheless, our metric explicitly takes into account the expected overlap between object estimates obtained at different wavelengths, and as such we mainly expect it to work very well for complex extended samples, where we expect that other methods will suffer from the twin image that is unavoidable in our setup. The optimization metric is a very smooth function, which is useful for a fast initial estimate of the optimal backfocusing position, but it could be that after an initial estimate the best position could be found by other means. Also, an initial investigation revealed that the metric performs similarly well for phase-only samples, such as the neurons in the original multi-wavelength paper (Noom et al. [38], Fig. 3). Most other sharpness estimates will perform differently for a phase-only estimate, for instance leading to a minimum instead of a maximum, which requires user knowledge about the sample for the metric to perform well. It remains to be seen if this focusing metric will compare favorably to other focusing techniques for different objects, but it seems to give a very accurate estimate of the optimal focusing position. Similar to other focusing metrics, we expect that an initial estimate can be obtained rapidly by downsampling the raw input images. Another interesting approach that appeared recently was to train a neural network to recognize the optimal backfocusing distance

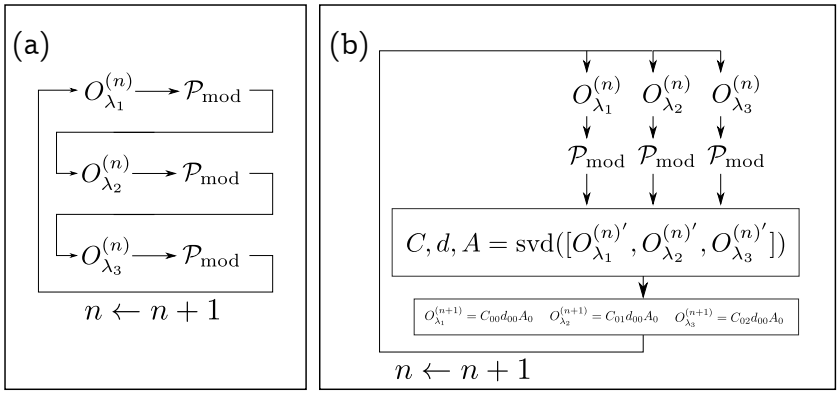

Fig. 3.10: (a) Original RGB phase retrieval scheme. The modulus constraint is applied sequentially onto the object for different wavelengths. The modulus constraint consists of propagating from the object plane to the camera plane, scaling the intensity such that it matches the expected intensity and propagating back to the object plane. In practice, the order of the wavelengths is shuffled after every iteration. A random initial estimate is inserted in the top left. (b) SVD-based reconstruction algorithm. The modulus constraint is applied to three object estimates at three different wavelengths. Afterwards, the corrected object estimates O'_{λ_i} at the three different wavelengths are forced to be the same up to an overall scaling, implemented by computing the largest singular vector. A random initial estimate can be inserted in the top.

[55]. Also in that work, an external reference beam was used to illuminate the sample, but it is probable that the neural network can be trained to ignore what appears to be a twin image.

3.2.2 *Alternative reconstruction algorithms*

As visible in Fig. 3.8, the largest singular vector of the diffraction patterns back-propagated onto the object plane seems to give quite a good approximation of the object. We investigated a slight alteration of the original phase retrieval algorithm, which takes advantage of this estimate. In the original reconstruction algorithm, Fig. 3.10a, the object is updated after processing every individual wavelength diffraction pattern. In our new algorithm, we compute three object estimates based on the diffraction patterns measured at three different wavelengths. A new estimate of the object is then computed based on the largest singular vector of the object. An overview of the algorithm is shown in Fig. 3.10b. This algorithm converges for all data that were investigated. A USAF target reconstruction, shown in Fig. 3.11a appears to be slightly better. The smallest features of group 7.6 are still discernible, but the background appears to be much less noisy. However, it is difficult to determine which algorithm performs better in case of the more complicated convollaria sample, shown in Fig. 3.11b. More research is needed to investigate this retrieval technique fully, which we will call the GS-SVD algorithm. To investigate how well

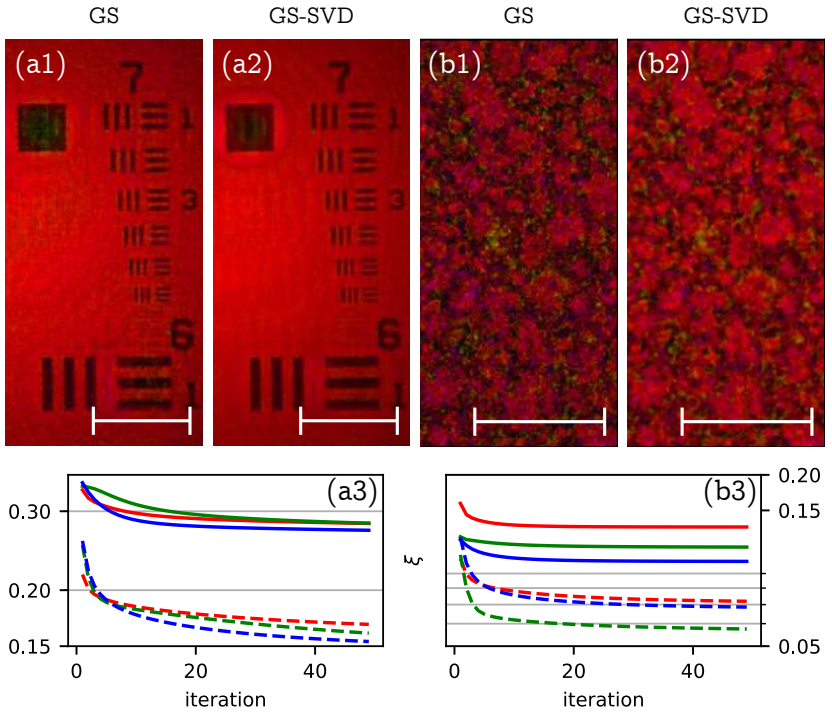

Fig. 3.11: Comparison of reconstruction performance for original algorithm (a1, b1) and new SVD-based algorithm (a2, b2) for a USAF target (a) and a convollaria sample (b). In both cases, 50 iterations were used to retrieve the sample. The GS-SVD algorithm seems to suffer less from noise in the reconstruction. Scalebar corresponds to 70 µm. (a3, b3): Error metric ξ for every color per iteration for the original GS-algorithm (solid lines, color represents color channel), and the new GS-SVD algorithm (dashed lines). In both cases, the error metric is lower for the GS-SVD based algorithm. The error metric at the first iteration corresponds to a large difference and has not been plotted.

the GS-SVD algorithm matches the observed camera intensities, we investigate the normalized difference between the expected camera intensities and the measured camera intensities, defined as:

$$\xi_{n,i} = \left\| \frac{I_{n,i}}{\|I_{n,i}\|_2} - \frac{I_{\lambda_i}}{\|I_{\lambda_i}\|_2} \right\|_2 \tag{3.8}$$

$$I_{n,i} = \mathcal{P}_{d\lambda_i}\left[O^{(n)}\right] \tag{3.9}$$

Where $\xi_{n,i}$ is the error metric at iteration n for wavelength i, $\|\cdot\|_2$ indicates the l_2 norm, and $I_{n,i}$ is the expected camera intensity. For a perfectly retrieved object the error metric should be zero. For the two samples under investigation, the GS-SVD algorithm results in a reconstruction with a smaller error metric than the original algorithm, shown in Fig. 3.11.

The GS-SVD algorithm can be expected to require more iterations than the

original Gerchberg-Saxton algorithm, as within every iteration, the object is only updated once. In the original implementation, the object is updated after processing every individual diffraction pattern. Especially in more complicated samples, we observe that smaller features require more iterations. However, the GS-SVD algorithm lends itself naturally for parallelization as the back-propagation steps are independent and as such convergence time is not be affected as much using an implementation on a graphics card. The GS algorithm could be sped significantly up by avoiding back-propagation to the object. A similar optimization can be made in this algorithm. Therefore we expect that the GS-SVD based algorithm should be only marginally slower than the original algorithm.

In the original GS-algorithm, the three different channels need to have the same intensity. However, in the SVD-based algorithm, an overall scaling of the intensity of the object for every wavelength is automatically taken into account by the coefficient matrix C as shown in the diagram. In most cases, ensuring similar intensities for the different wavelengths is trivial but in some cases, such as when the wavelengths are detuned in such a way that a single diffraction pattern bleeds into different channels, this can be a useful addition. Sanz et al. [56, 57] showed a similar algorithm based on averaging the estimates at the three different wavelengths and a high-pass filtering operation on the object. We expect that these algorithms perform similar in cases where the intensity of the illuminating beams all have a similar intensity. In cases where the intensity of the illuminating beams cannot be fully controlled we expect our algorithm to perform better.

An interesting extension could be made when a large number of wavelengths are available. Instead of only keeping the largest singular vector, all of the estimates at the different wavelengths are reconstructed based on a reduced number of empirical orthogonal functions, for instance by using a truncated SVD reconstruction, similar to ptychographic probe translation retrieval as described by Odstrcil et al. [58]. That way, an object estimate can be obtained at different wavelengths, relaxing the requirement that the object has to appear exactly the same for different wavelengths. However, this was not investigated at the time of writing this thesis.

3.2.3 *Tracking an object in three dimensions*

The GS-SVD reconstruction was combined with the autofocusing method into a first prototype of a tracker of an extended sample in three dimensions. For a proof-of-concept experiment, a fixed mosquito wing was inserted at a distance of roughly 1 cm from the camera, mounted on a translation stage. While a video was recorded, the object was first moved away from the camera (Fig. 3.12a), and then moved parallel to the camera (Fig. 3.12b). While moving the sample away from the camera, the lensless magnification changed as described by Eq. (3.3), and the back-propagation distance is scaled in a similar way. Unfortunately, the camera-fiber distance was not measured. Therefore, the absolute back-propagation distance could not be computed. In the second

part of the movie, the back-propagation distance stayed the same, and even though the scaling is not known, using FFT-based phase correlation of the gradient of the raw diffraction images [59, 60] , the $x - y$ position could be tracked from frame to frame. The algorithm seems to be well capable of providing a good estimated back-propagated distance, even for large displacements such as at the end of the first video. Unfortunately, some camera settings were incorrectly set and as such the reconstruction quality of the individual frames is rather poor. More experiments are needed to determine if this method indeed works robustly enough to enable 3D-tracking of a smaller sample, such as a moving *C. elegans* nematode.

3.2.4 *RGB imaging with IRGB diodes*[1]

One of the main assumptions of the original reconstruction algorithm is that the sample appears to be the same for all wavelengths. As discussed in Sec. 3.1.4, many biological samples appear to be wavelength-dependent and as such the reconstruction suffers from artifacts. However, most biological samples have a much more similar appearance in the infrared rather than visible wavelengths. We studied back-focused images of a stationary *C. elegans* at five different wavelengths to investigate if it would appear to be more similar for infrared wavelengths, shown in Fig. 3.13. It should be noted that these individuals are much bigger than the nematodes studied in Sec. 3.1.4 and as such we expect the wavelength-dependent aberrations to be worse. Under visible illumination, visible in the top row, the structure of the nematodes appears to be strongly wavelength-dependent. In the near infrared, visible in the bottom row, the nematodes have a very similar internal structure for all wavelengths. Unfortunately, while changing the illumination settings which took a few minutes, the appearance of the nematodes changed quite drastically, which is why the two images at 660 nm look different even though they would ideally be identical. Therefore, a natural extension of the algorithm would be to repeat the experiment but with more suitable infrared wavelengths and a suitably adapted camera. However, the color filter array of an RGB camera is not easily adapted to a new wavelength, although recently RGB-IR cameras have appeared on the market [61].

Instead of attempting to build a specialized camera, we observed that infrared light incident on the detector will be detected by all camera channels in different ratios, shown in Fig. 3.14. We refer to this as channel mixing. When the camera is illuminated with three different infrared wavelengths, a linear combination of the different diffraction patterns will be measured. Choosing a suitable combination of wavelengths allows to invert this mixing and retrieve the single-wavelength diffraction patterns. The object can then be reconstructed with the previously mentioned RGB phase retrieval algorithms,

1 Parts of this work was done in collaboration with Carlijn Bos, a bachelor student who implemented the initial algorithm and was responsible for building the optical setup. Subsequent SVD and forward-model reconstructions were developed at a later stage.

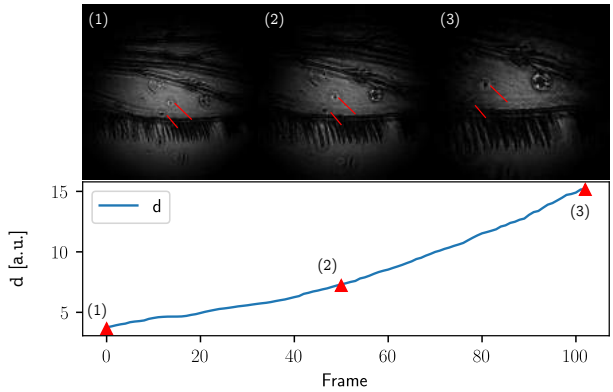

(a) A mosquito wing is translated away from the camera position, leading to varying lensless magnification. As the fiber-to-camera distance was not calibrated, the $x-y$ translation could not be tracked and the lateral position is not tracked.

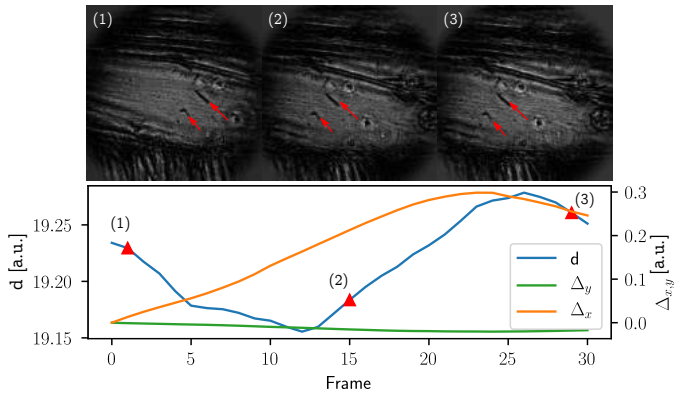

(b) A mosquito wing translated mainly parallel to the camera. Based on features on the sample, the estimated field of view is around $300 \pm 100\mu$m. The back-propagation distance should be almost constant and appears to vary very little during the measurement.

Fig. 3.12: Initial results of tracking a complicated structure in 3D using an RGB setup. The automated focusing method kept the sample in focus throughout the entire movie. Red arrows indicate the same features throughout the three frames in each subfigure. Bottom graphs: estimated back-propagation distance (a) and x-y translations (b) of a mosquito wing that was moved during acquisition. Top: Three typical reconstructed intensity frames, back-propagation distances indicated in graph below. As the camera to fiber distance was not calibrated, an absolute value for lateral displacement cannot be given. Background levels appear to be different as the intensity of the illuminating beams was taken into account in (b).

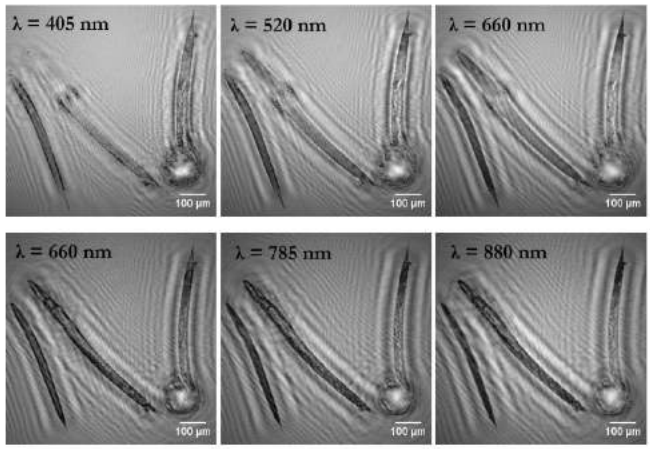

Fig. 3.13: Back-propagated image of a *C. elegans* nematode for five different wavelengths. The intestines of the nematode show clear differences for different visible light wavelengths, but appear much more similar for the infrared wavelengths.

at the expense of an increased level of noise in the input data and therefore in the resulting images.

Recovering single-wavelength diffraction patterns

The intensity in every channel of every pixel on the camera can be described by an intensity-based transmission matrix.

$$\begin{pmatrix} r \\ g \\ b \end{pmatrix} = M \begin{pmatrix} I_{\lambda 1} \\ I_{\lambda 2} \\ I_{\lambda 3} \end{pmatrix} = \begin{pmatrix} m_{r\lambda 1} & m_{r\lambda_2} & m_{r\lambda_3} \\ m_{g\lambda 1} & m_{g\lambda_2} & m_{g\lambda_3} \\ m_{b\lambda 1} & m_{b\lambda_2} & m_{b\lambda_3} \end{pmatrix} \begin{pmatrix} I_{\lambda 1} \\ I_{\lambda 2} \\ I_{\lambda 3} \end{pmatrix} \tag{3.10}$$

Where r, g, and b are the detected pixel values in the "red", "green" and "blue" channels, and $I_{\lambda(1,2,3)}$ are the incident intensities on the pixel for wavelengths $\lambda_1, \lambda_2, \lambda_3$. M is a 3×3 matrix describing the sensitivity of every wavelength to every channel. For instance $m_{r\lambda 1}$ describes the sensitivity of the first wavelength to the red channel. This relation can be inverted to reconstruct the intensities of the individual diffraction patterns.

$$\begin{pmatrix} I_{\lambda 1} \\ I_{\lambda 2} \\ I_{\lambda 3} \end{pmatrix} = M^{-1} \begin{pmatrix} r \\ g \\ b \end{pmatrix} \tag{3.11}$$

It is important that this inverse exists and that it is numerically stable. Furthermore, because of the limited bit depth of the camera, all channels should have a similar intensity. In practice this is difficult to realize as the red channel is more sensitive to almost all infrared wavelengths, but at least there has to be significant intensity in the other channels. To ensure a similar reaction to biological material, all wavelengths should be longer than 600 nm. The

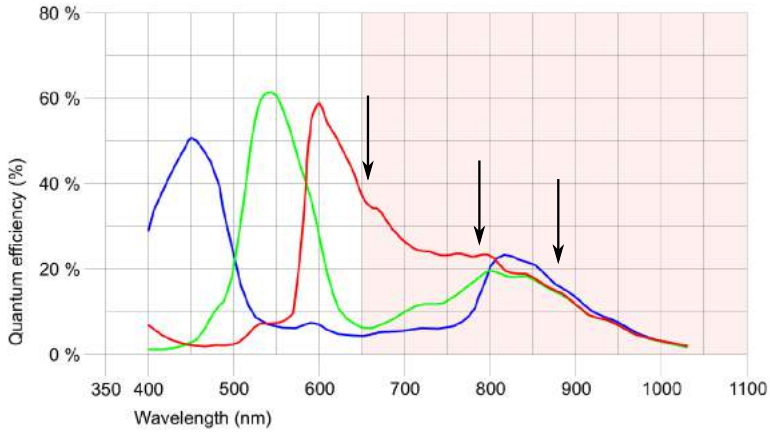

Fig. 3.14: Spectral response of the camera, as per the manufacturer's specifications. Arrows indicate the chosen wavelengths.

three wavelengths should be sufficiently different that the detected diffraction patterns are different. This is dependent on the sample but as a minimum we took a wavelength separation of 50 nm. After some initial investigations we ended up with an illumination at 880, 785, and 660 nm. All color channels are similarly sensitive to illumination at 880 nm, and 660 nm is mainly sensitive to the red channel. The channel mixing matrix was measured by turning on the laser diodes one by one and recording the average intensity in the central area of the chip for all channels.

$$M=\begin{pmatrix} 0.49 & 1.0 & 0.90 \\ 0.47 & 0.66 & 0.01 \\ 0.59 & 0.37 & 0.08 \end{pmatrix} \quad , \quad M^{-1}=\begin{pmatrix} -0.26 & -1.27 & 2.95 \\ 0.18 & 2.45 & -2.13 \\ 1.07 & -2.03 & 0.77 \end{pmatrix}$$

Where the columns correspond to 880, 785 and 660 nm. The rows of M^{-1} show that the single-wavelength diffraction patterns correspond to subtracting different channels from each other, increasing the noise level significantly. For instance, the diffraction pattern at 880 nm is computed as the difference between the green (-1.27) and the blue (2.95) channel. Therefore, the noise level in this reconstruction is significantly increased. However, the reconstructed diffraction patterns correspond to the single-wavelength diffraction patterns and as such they can be fed directly into the original algorithm.

In order to demonstrate that raw data cannot be reconstructed using the original algorithm, the GS-reconstruction algorithm was run on the input data without applying any channel demixing, visible in Fig. 3.15a. Even though some sharp features appear, the image suffers from severe aberrations, and a strong twin image appears. After applying M^{-1} on every pixel in the input images and running the GS-reconstruction algorithm again, shown in Fig. 3.15b, the twin image seems to be reduced, and image is sharper. However, the noise levels are severely increased, leading to an image that appears to

be worse than the original reconstruction where the channel mixing was not taken into account. Therefore, it can be concluded that direct inversion of the coupling matrix does not result in a better image in general. As a projection-based algorithm, the Gerchberg-Saxton algorithm is sensitive to noise [62] and as such the input images are of insufficient quality to retrieve the object. Different methods that are designed to cope with noisy measurement data could provide with a more suitable reconstruction algorithm, for instance based on extended complex Kalman filtering [63]. Alternatively, the algorithm could work for a camera with a higher bit depth and reduced noise levels.

As a straightforward extension of this basic reconstruction algorithm, we applied the GS-SVD reconstruction algorithm to the same demixed input data, Fig. 3.15c. This resulted in a much improved object estimate. We expect that the singular vector estimate is reasonably efficient at suppressing noise from the individual wavelength-dependent diffraction patterns. Furthermore, when M is not perfectly measured, the input data could still contain some shadows from the original diffraction patterns. However, they will appear to be "wavelength-dependent" as their back-propagation distance is incorrect, and therefore they will mainly show up in the higher order singular vectors, and therefore be suppressed.

A different research group reported on building a field-portable microscope prototype using a related algorithm and a very similar setup [57]. Instead of replacing the object estimate with the largest singular vector, they average the three images and employ what is essentially a high-pass filter over the reconstructed images. In their implementation, the wavelength differences are much bigger and range from the UV to the infrared. Therefore, crosstalk seems to be less of an issue. Nevertheless, their reconstructions images appear to suffer from aggravated noise levels as well, but it does seem to work slightly better than in our case. For biological samples these large wavelength differences will induce wavelength-dependent features similar to the nematodes. Therefore, for most biological specimen infrared wavelengths are a more suitable choice.

Forward model

One of the main limitations of the previously mentioned reconstruction method is that the noise levels are high in the reconstructed input data. The camera noise between different channels appears to be uncorrelated and as such subtracting two channels leads to an image with a higher noise level. Even though this could partially be solved by switching to the SVD-based reconstruction, the reconstruction will still be much noisier. Instead of attempting to directly alter the input data, the reconstruction algorithm can also be changed in order to take into account the channel mixing explicitly. As will be shown, this leads to a further reduction of the noise level, at the expense of an increase in computation time. The main difference with the original method is that we explicitly incorporate a forward model to predict the intensity on the camera, based on the object estimate, and as such we avoid having to invert the channel mixing matrix. The steps involved are:

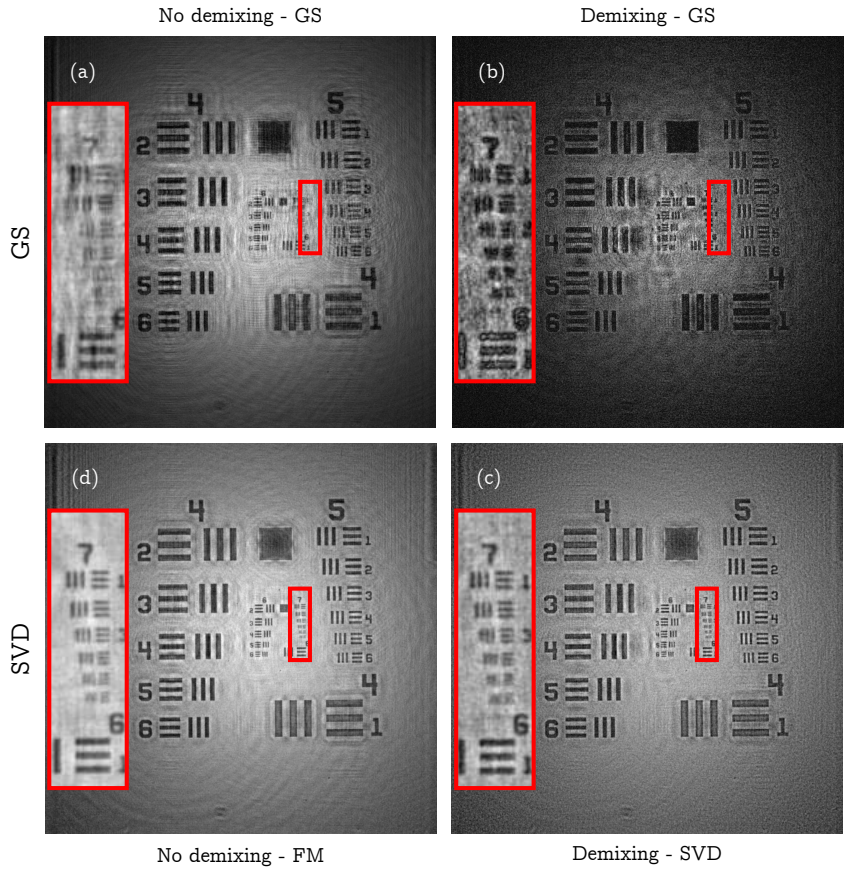

Fig. 3.15: (a): Uncorrected reconstruction, (b): Reconstruction using original algorithm with demixed input images, (c): SVD-based reconstruction on demixed channels, (d) Forward-model (FM) reconstruction. Inset shows features that can be resolved from group seven. Both SVD-based and FM reconstruction are much less noisy, but the FM seems to result in the best reconstruction.

1. The exit wave of the object is propagated to the camera at all wavelengths:

$$\psi_{\lambda_{1,2,3}} = \mathcal{P}_{p\lambda_{1,2,3}}[O] \tag{3.12}$$

2. The measured channel-mixing matrix is used to compute the expected intensity in a single channel.

$$I_i^{mod} = M_i \cdot \begin{pmatrix} |\psi_{\lambda_1}|^2 \\ |\psi_{\lambda_2}|^2 \\ |\psi_{\lambda_2}|^2 \end{pmatrix} \tag{3.13}$$

Here, I_i^{mod} is the expected intensity for color channel i, M_i is the row corresponding to the sensitivities of channel i to every wavelength.

3. The amplitudes of the estimates at the camera plane are adjusted to make sure that the intensity measured in channel i matches the expected intensity. As the channel intensity is a linear combination of the intensities of the different wavelengths, any linear combination of scalings for all wavelengths could be used but we employ the most simple update, which is scaling all fields by the same factor. This is an update that has also been used for instance in mixed-state ptychography [39, 64].

$$\psi'_{\lambda_{1,2,3}} = \sqrt{\frac{I_i^{\text{meas}}}{I_i^{\text{mod}}}}\psi_{\lambda_{1,2,3}} \tag{3.14}$$

4. Back-propagating these estimates leads to a corrected estimate of the object at all wavelengths:

$$O'_{\lambda_{1,2,3}} = \mathcal{P}_{-d\lambda_{1,2,3}}\left[\psi'_{\lambda_{1,2,3}}\right] \tag{3.15}$$

5. Not all of these estimates are equally useful. If the first channel ($i = 0$) is exclusively sensitive to the red wavelength, the altered estimates to the second and third wavelength will not yield useful information. In order to suppress estimates based on a low intensity on the camera, we update the object estimates by the difference between the original object estimate and the corrected object estimate weighted by the strength of that component on the camera.

$$O''_{\lambda_j} = O_{\lambda_j} + M_{i,j}\left(O'_{\lambda_j} - O_{\lambda_j}\right) \tag{3.16}$$

   Where j iterates over all wavelengths.

6. After this operation, there are three different estimates of O, for different wavelengths. We employ a truncated singular value decomposition (svd) to compute a good estimate of the actual object.

$$C \cdot D \cdot A = \text{svd}\left(\left[O''_{\lambda_1}, O''_{\lambda_2}, O''_{\lambda_3}\right]\right) \tag{3.17}$$

   Where C is a coefficients matrix, D is a diagonal matrix specifying the relative strength of the different components and A corresponds to the singular vectors. In order to keep only the largest singular vector we set all elements in D to zero except the first, and we call it d'

$$\psi_{\lambda_{1,2,3}} = C \cdot d' \cdot A \tag{3.18}$$

$$j \in \{1,2,3\} \tag{3.19}$$

   Therefore, after this operation the object estimates for all wavelengths are the same up to an overall scaling defined by C.

7. Repeat step 1–6 for all channels.
8. Repeat step 1–7 for n iterations.

This algorithm will require more updates and every update is computationally more expensive, as it requires six Fresnel propagations for every iteration, but it avoids inverting the channel mixing matrix.

As visible in Fig. 3.15, the reconstructed field of a USAF target resulting from the forward model is significantly better than any reconstruction relying on decomposing the diffraction patterns a priori. In a related field, called Fourier ptychography, it was shown that noise plays an important role in reconstructing high-quality images and that an algorithm employing a proper noise model will lead to a better reconstruction [65].

To demonstrate the feasibility for the original goal, imaging biological samples with a wavelength-dependent structure, single-shot three-wavelength diffraction patterns were recorded for the same sample as in Fig. 3.13, and the object was reconstructed using the three algorithms that are available. To make sure that a steady state was achieved, all algorithms were run for 500 iterations. All visible-light reconstructions suffer from twin image artifacts, visible as artificial fringes parallel to every nematode. The original GS algorithm seems to suffer the least from these artifacts but the features within the nematode also seem to be mostly unsharp. The infrared reconstruction provides an improvement, the structure within the nematodes is revealed and most of the twin image features are removed. In this case, the original GS algorithm leads to slightly more artificial fringes than the forward model. All methods reveal the same intestines in the central nematode.

A further increase in reconstruction quality for this type of algorithm could likely be obtained taking into account the exact layout of the color-sensitive pixels on the camera. Color cameras have a Bayer frame with pixels that are only sensitive to a single channel. The final image is reconstructed using interpolation of the missing values. Currently a large lensless magnification is required to achieve a resolution on a similar level as the pixel size, which limits the field of view. It would be interesting to investigate if taking into account the exact pixel layout could allow for a better resolution even with lower lensless magnifications. Also, using some adoptions of the forward model it might be possible to reconstruct the transmission matrix together with the object. Together with the autofocusing, the new infrared system could have a clear application in flow cytometry or tracking of the swimming behavior of microscopic organisms.

In this chapter we have demonstrated the original RGB-based multi-wavelength Fresnel microscope, along with a few new developments indicating different ways in which the processing of the original diffraction patterns can be improved and further automated. Together, these new developments could lead to a cost-effective and versatile 3D-tracker of biological specimen.

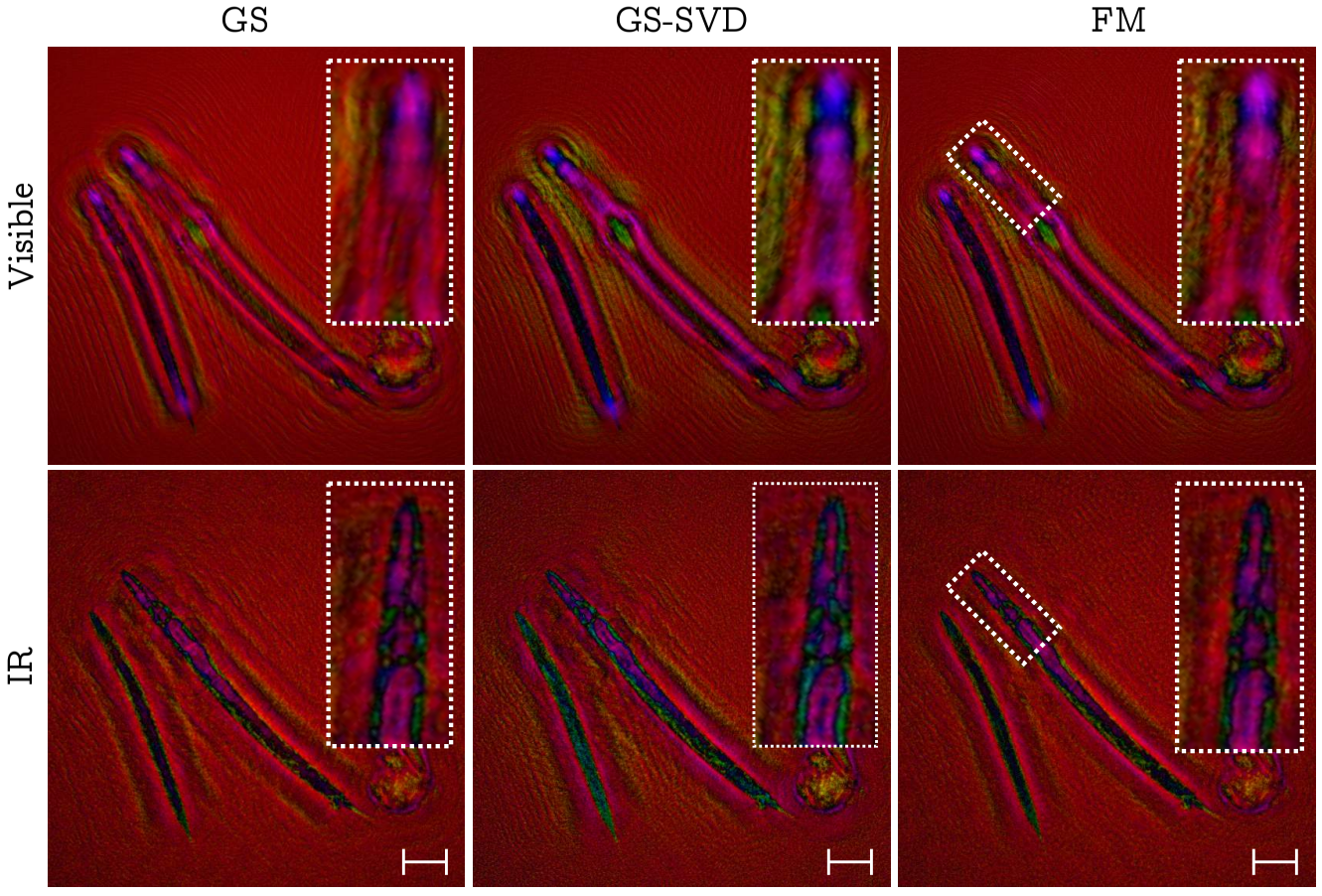

Fig. 3.16: Top row: RGB reconstruction of a *C. elegans* sample using (left) GS algorithm with unmixed channels, (middle) GS-SVD algorithm with unmixed channels and (right) forward model. Inset shows nematode head, position indicated by white dashed rectangle. All reconstruction algorithms fail as the nematodes have wavelength-dependent features. Bottom: Same reconstruction in the infrared. Overall, the reconstruction artifacts seem to be reduced, with the least amount of spurious twin images in the forward model reconstruction. Details in the nematode anatomy can be extracted, especially visible in the inset. Scalebar represents $100\,\mu\mathrm{m}$.

4

INTERFERENCE PROBE PTYCHOGRAPHY FOR COMPUTATIONAL AMPLITUDE AND PHASE MICROSCOPY

Dirk E. Boonzajer Flaes, Stefan Witte

This chapter has been published as: "Boonzajer Flaes, D.E., and Witte, S. (2018). Interference probe ptychography for computational amplitude and phase microscopy. Opt. Express 26, 31372" [66]. The supplemental material is presented at the end of the chapter. No changes have been made to the published text.

ABSTRACT

We have developed an approach to Fresnel domain ptychography in which the illumination consists of an interference pattern. This pattern is conveniently created by overlapping two coherent beams at an angle. Only the phase and orientation of the interferometric fringe pattern needs to be scanned to reconstruct a high-fidelity object image, which alleviates the requirements for accurate sample positioning and system stability. As such, the resulting imaging systems can be constructed in an extremely simple and robust way. Object images are reconstructed from recorded Fresnel diffraction data using a modified ptychographical iterative engine. We demonstrate the capabilities of this imaging system by recording images of various biological samples, demonstrating quantitative phase contrast as well as a spatial resolution better than 2.2 µm.

4.1 INTRODUCTION

Lensless or computational imaging is an upcoming imaging method, in which numerical algorithms are used to replace (part of) the conventional optical components to achieve image formation in a microscope system. The central challenge in lensless imaging is the need to numerically retrieve a phase associated with a measured diffraction pattern, as the full electric field of a diffraction pattern needs to be known to numerically propagate the wave field back to the position where the object was located [5, 22, 28, 67]. Various forms of lensless imaging have been introduced in recent years [29, 33, 38, 56, 68, 69]. One of the most promising approaches is known as ptychography, which uses translational diversity to robustly retrieve the phase associated with measured diffraction patterns. The main implementation of ptychography is through spatial translation of the object through a spatially constrained beam profile [6].

This approach can typically retrieve both the fields associated with object and the illumination. While the initial version required high coherence and exact knowledge of the different illumination positions, more recent work has relaxed these requirements and enabled position correction [70, 71], as well as illumination with partially coherent beams and even speckle patterns [8, 39, 72, 73]. However, such additions do come at the cost of increased computational complexity, or with the need for a higher degree of measurement diversity, thus increasing measurement time.

Recent work has shown that interference patterns are a viable tool for structured illumination coherent diffractive imaging (CDI) [74–76]. Interference pattern illumination is an interesting approach to introducing measurement diversity in CDI, as it can be readily implemented, and accurate scanning interference patterns over a large field-of-view is possible with relatively simple optical setups. In a practical realization, a sample is illuminated with two overlapping coherent beams at an angle which generate an interference pattern on the sample. The resulting diffraction pattern is measured directly on a camera located close to the sample, employing no further imaging optics. To ensure sufficient measurement diversity, the propagation distance between camera and sample [74] or the orientation of the fringes [75, 76] can be scanned to collect a series of probe-response measurements. From this measurement set, an object is reconstructed using a phase retrieval algorithm.

In this work, we demonstrate a new approach to interference-based diffractive imaging, shifting the illumination fringes over the sample as well as changing the orientation to a few different orientations, but keeping the propagation distance constant. This setup minimizes the amount of mechanical movement needed for data acquisition, and does not require interferometric stability on timescales longer than a single camera frame acquisition. This enables us to create a very compact setup. We also show - for the first time to our knowledge - that a dataset consisting of only interference patterns and the resulting diffraction patterns can be used for a ptychographical reconstruction using the ptychographical iterative engine (PIE), and we show that some of the common extensions to regular ptychography, such as superresolution-ptychography (SR-PIE)[77] and translation position correction [70] can be employed as well. Furthermore, we systematically investigate the amount of measurement diversity needed for accurate image reconstruction, and find that the amount of measurements can be kept quite limited. We demonstrate this technique using a USAF target and two biological specimen, a mosquito wing containing many microscopic features, and a thick biological nematode (*Caenorhabditis Elegans*) sample, and obtain high-resolution amplitude and quantitative phase images for each of them.

4.2 OPTICAL SETUP

While there are numerous ways of creating an interference pattern, we chose to employ a transmission-grating-based setup, because of its simple and robust nature. An overview of the setup is shown in Fig. 4.1. A grating is imaged

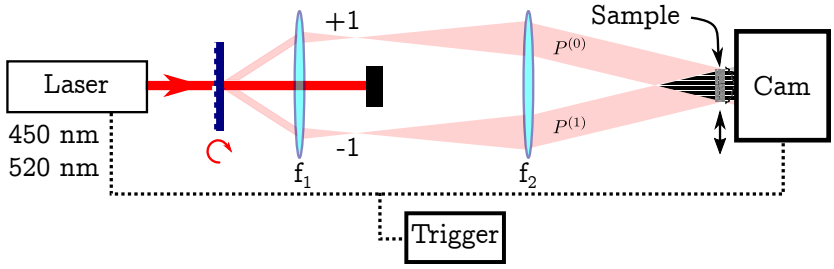

Fig. 4.1: Optical setup for interference probe ptychography. A laser (450 nm, Thorlabs LP450-SF15 or 520 nm, Thorlabs LP520-SF15) illuminates a grating (120 lp/mm, Edmund optics, #66-342), which is imaged onto the sample using a 4f-imaging system (f1=25 mm, f2=100mm), while blocking the zero order diffraction. The camera (IDS UI-5482LE-M) is positioned a short distance (approximately 1 mm) behind the sample. The illumination beams are called $P^{(0)}$ and $P^{(1)}$, at the sample plane. The grating is mounted on a rotatable mount to allow easy changing of the orientation of the fringes. The sample is mounted on a transition stage in order to repeatedly remove and insert it for the reference measurement. In order to shift the illumination pattern over the sample, the setup is mechanically disturbed. The laser is triggered to the camera to minimize motion blurring.

onto a sample whilst suppressing the zero order transmission, as indicated. To enable changing the orientation of the fringes, the rotation of the grating can be controlled. It should be noted that neither the optical quality of the imaging lens, nor the quality of the grating are particularly important for the imaging performance. The magnification of the lens-based system was chosen such that maxima of the fringe pattern are separated by roughly four pixels on the camera. In this proof-of-concept experiment, adjusting the path length difference of the interferometer (which determines the position of the maxima of the fringes) was performed by a mechanical disturbance to the setup during image acquisition. Even though this does not allow deterministic control of the path length differences, these parameters can be extracted from the measured diffraction patterns a posteriori.

A measurement consists of illuminating the object with fringe patterns under a limited number of orientations, while scanning the pathlength differences, and recording the resulting diffraction patterns. As our setup does not support deterministic control over the pathlength differences, we record 50 camera frames even though we only require about four for every orientation to do the reconstruction. From this series of measurements, the relevant frames are extracted in the processing routine based on minimal overlap, as described in the Appendix, Sec. 4.6.1. Additionally, a reference measurement is taken for each grating orientation while the sample is removed, consisting of the individual beams and a single interference pattern. This is done immediately after the sample measurement, but it could also be done as a separate reference measurement. To allow straightforward insertion and removal of the object, it was mounted on a translation stage. A typical diffraction image is shown in Fig. 4.3a.

4.3 NUMERICAL IMAGE RECONSTRUCTION

4.3.1 *Overview of the reconstruction algorithm*

The reconstruction process relies mainly on the standard ptychographical iterative engine (PIE) algorithm [40], with some changes applied to speed up convergence as described in [31] by Maiden et al. As with any ptychographical experiment, accurate knowledge of the illumination function P is very important. As this is slightly more involved in our setup, it will be discussed extensively in the next section, and for now we presume that electric field illuminating the sample is known for all measurements. Throughout this paper, all variables in capitals represent 2D functions, where X is a field at the object plane and $\widetilde{X}$ represents a field at the camera plane. Lowercase variables represent (complex) scalars. The only exception is the measured intensity, which is represented by I.

The measurement set that we acquired consists of a series of diffraction patterns $I_{i,j}$ for a few different pathlength differences and a few different grating orientations, where index i indicates the grating orientation and index j indicates the measurement number. Furthermore, using a calibration measurement, we have access to the electric field of both illumination beams $P_i^{(0)}$, $P_i^{(1)}$ for every fringe orientation and their relative pathlength difference δ for every measurement i, j. The guess of the exit wave at the object location $\Psi_{g,n,i,j}$ is computed for both beams separately using the current guess of the object $O_{g,n}$.

$$\Psi_{g,n,i,j} = \Psi^{(0)}_{g,n,i,j} + \Psi^{(1)}_{g,n,i,j} \tag{4.1}$$

$$\Psi^{(0)}_{g,n,i,j} = P_i^{(0)} O_{g,n} \exp(+\imath\delta_{i,j}/2) \tag{4.2}$$

$$\Psi^{(1)}_{g,n,i,j} = P_i^{(1)} O_{g,n} \exp(-\imath\delta_{i,j}/2) \tag{4.3}$$

Where the subscript g stands for guess, n is the iteration number, and i, j are grating orientation and measurement number, respectively. $P^{(0)}$ is the electric field of the first beam, and $P^{(1)}$ is the electric field of the second beam at the object location. $O_{g,n}$ is the current object guess. $\delta_{i,j}$ is determined by path length difference between the two arms of the interferometer. The two beams are propagated to the camera:

$$\widetilde{\Psi}_{g,n,i,j} = \widetilde{\Psi}^{(0)}_{g,n,i,j} + \widetilde{\Psi}^{(1)}_{g,n,i,j} \tag{4.4}$$

$$\widetilde{\Psi}^{(0)}_{g,n,i,j} = \mathcal{P}_d \left[\Psi^{(0)}_{g,n,i,j} \right] \tag{4.5}$$

$$\widetilde{\Psi}^{(1)}_{g,n,i,j} = \mathcal{P}_d \left[\Psi^{(1)}_{g,n,i,j} \right] \tag{4.6}$$

Using operator notation where $\mathcal{P}_d[\cdot]$ stands for Fresnel propagation from the object to the camera. In regular ptychography, the modulus constraint is now applied, scaling the amplitude of every pixel in $\widetilde{\Psi}_{g,n,i,j}$ with the measured

amplitude $\sqrt{I_{i,j}}$ and the resulting field is numerically propagated back to the object. However, this presumes a laser with perfect coherence. Our setup is sensitive to a path length difference between the two arms of the interferometer and therefore it is important to take into account the limited mutual coherence of the two probe beams. Otherwise, the fringe contrast on the camera will be overestimated and this leads to a large overestimation of the electric field in areas of the probe with low intensity, resulting in artifacts in the reconstruction. However, it is possible to extract the mutual intensity C_i from the same reference measurement as was used to characterize both of the probes. To take this effect into account, a forward model is employed to compute the expected intensity profile on the camera, and a similar update as in [72, Eq. 5] was implemented. In general, the modulus constraint for a function $\widetilde{\Psi}$ can be written as:

$$\widetilde{\Psi}' = \widetilde{\Psi}\sqrt{\frac{I_{\text{measured}}}{\widetilde{I}_{\text{expected}}}} \tag{4.7}$$

Where I_{measured} is the measured intensity on the camera, and $\widetilde{I}_{\text{expected}}$ is the expected camera intensity. To account for imperfect incoherence we compute $\widetilde{I}_{\text{expected}}$ in the following way:

$$\widetilde{J}_{g,n,i,j} = |\widetilde{\Psi}^{(0)}_{g,n,i,j}|^2 + |\widetilde{\Psi}^{(1)}_{g,n,i,j}|^2 + 2\gamma C_i \Re\left(\widetilde{\Psi}^{(0)}_{g,n,i,j}\widetilde{\Psi}^{(1)*}_{g,n,i,j}\right) \tag{4.8}$$

Which explicitly writes out the expected intensity of two beams with imperfect mutual coherence. Here, $\widetilde{J}_{g,n,i,j}$ is the expected intensity on the camera and C_i is the mutual intensity function as extracted from a reference measurement for fringe orientation i. In a perfectly coherent system, C should be unity but in our measurements it is usually on the order of 0.85-0.9. γ is a constant which allows to scale the mutual intensity function and is usually kept at one. Updating the object estimate then proceeds as follows:

$$\Psi_{c,n,i,j} = \mathcal{P}_{-d}\left[\widetilde{\Psi}_{g,n,i,j}\sqrt{\frac{I_{i,j}}{\widetilde{J}_{g,n,i,j}}}\right] \tag{4.9}$$

Where $\mathcal{P}_{-d}[\cdot]$ stands for Fresnel propagation from the camera to the object, $\Psi_{c,n,i,j}$ is the corrected exit wavefront. Now the object still needs to be updated with the additional information present in $\Psi_{c,n,i,j}$. However, $\Psi_{c,n,i,j}$ represents an updated estimate to $O \times P$. An intuitive approach to estimate the object would be to divide out the probe, but as the illumination pattern contains a large number of zeroes this is not a fruitful approach. However, there are numerous ways to do this, and we choose the rPIE update function [31]:

$$\begin{aligned} P_{i,j} &= P_i^{(0)}\exp(+\imath\delta_{i,j}/2) + P_i^{(1)}\exp(-\imath\delta_{i,j}/2) \\ O_{c,n} &= O_{g,n} + \frac{P^*_{i,j}}{(1-\alpha)|P_{i,j}|^2 + \alpha|P_{i,j}|_{\max}}(\Psi_{c,n,i,j} - \Psi_{g,n,i,j})\,. \end{aligned} \tag{4.10}$$

Where $O_{c,n}$ is a corrected object estimate, $P^*_{i,j}$ the conjugated expected field of the combined probes, and α is a regularization parameter. In the original

rPIE implementation, α was set at 0.15. In our case, the the entire area will be very evenly illuminated and as such the first term in the denominator, which scales the intensity of areas with a low intensity is not particularly valuable. Therefore we chose to set α slightly higher, at 0.5.

In classical PIE, the object is updated with this guess and the next diffraction pattern is taken. However, as there is a lot of spatial overlap in between our probes, it turned out that computing the update for all fringe positions of one orientation and averaging them leads to more robust results, especially when assessing a limited number of fringe orientations. We will call this averaging approach meanPIE, and it is similar to a parallel PIE [30] algorithm. Averaging all of the updates for all orientations resulted in a very stable image, but with artifacts for more complicated structures. An overview of results for different update methods is given in Appendix 4.8. After iterating over all of the orientations, we arrive at a new guess of the object, $O_{g,n+1}$.

4.3.2 *Determination of the reconstruction parameters*

For a proper ptychographical reconstruction, multiple parameters need to be known. These are the back-propagation distance d, the electric field of all the probes $P_i^{(0,1)}$, the relative pathlength differences $\delta_{i,j}$, and the mutual coherence functions C_i.

As mentioned in the preceding section, an accurate estimation of the illuminating fields ($P_i^{(0)}$ and $P_i^{(1)}$) at the object plane is required. In standard ptychography, the probe is moved with respect to the object and its contribution can be separated from the object, enabling to reconstruct the probe along with the object[30, 58]. As the probe does not move with respect to the object, it is much harder to distinguish between feedback on the probe and feedback on the object in our case. Luckily, the process by which the probes are formed is well known and enables us to create a very accurate prediction of the illumination pattern. Furthermore, the path length difference between the probes has to be estimated as this cannot be controlled during the measurement.

Reconstructing probe beams

From a reference measurement, consisting of the intensity of both individual beams and a measurement of the interference pattern between the two reference beams, the spatial phase profile corresponding to the difference in phase curvature $\Phi_i = \Phi_i(x, y)$ between the two beams is reconstructed using off-axis holography [17]. Other methods, such as principal component analysis [78] could be employed as well. This phase difference contains a large linear phase slant corresponding to the angle between the two beams, and a nonlinear part corresponding to grating imperfections or imperfections in the imaging system. To make sure that the object is propagated back perpendicular to the camera and not in the direction of one of the two beams, the linear part of the phase slant is divided over the two beams. Additionally the fringe contrast C_i is extracted. Afterwards, we will need an additional alignment procedure to

align the probes of different orientations, which is why we call this intermediate probe estimation $\widetilde{Q}$ instead of $\widetilde{P}$. The expected field on the camera of the two probes for every orientation can be written as:

$$\widetilde{Q}_i^{(0)} = \sqrt{I_i^{r(0)}} \exp\left(-\frac{\imath}{2}(k_x x + k_y y)\right) \tag{4.11}$$

$$\widetilde{Q}_i^{(1)} = \sqrt{I_i^{r(1)}} \exp\left(-\frac{\imath}{2}(k_x x + k_y y) + \imath\Phi_i\right). \tag{4.12}$$

Where $\widetilde{Q}$ represents the electric field on the camera. k_x and k_y are the average direction of the phase map, found by locating the maximum of the FFT of $\exp(\imath\Phi)$. $I_i^{r(0,1)}$ are the measured intensity profiles on the camera of reference beams 0 and 1, with the sample removed.

Automated retrieval of the focus position

As an optional step in the measurement preparation procedure, our method lends itself very naturally for a form of "autofocusing", where the camera-sample distance is found automatically based on a parallax measurement. If in addition to the interference patterns, the intensity images of the separate beams illuminating the sample have been retrieved, the propagation distance can be estimated by propagating back both beams under their appropriate angles. The optimal back-propagation distance is found when the two images overlap. The refocused images are computed as:

$$D_i^{(0)}(z) = \left|\mathcal{P}_{-z}\left[\left(\sqrt{I_i^{(0)}} - \sqrt{I_i^{r(0)}}\right)\right]\right|^2 \tag{4.13}$$

$$D_i^{(1)}(z) = \left|\mathcal{P}_{-z}\left[\left(\sqrt{I_i^{(1)}} - \sqrt{I_i^{r(1)}}\right) e^{+\imath\Phi_i}\right]\right|^2 \tag{4.14}$$

$D_i^{(0)}$ can be seen as the object estimate of the individual beams, suffering from a twin image. When the back-propagation distance is found, $D_i^{(0)}$ and $D_i^{(1)}$ overlap, and the l_2-norm of the difference will be minimal:

$$d_i = \mathbf{argmin}_z \|D_i^{(0)}(z) - D_i^{(1)}(z)\|_2 \tag{4.15}$$

Where $\mathbf{argmin}_z[\cdot]$ returns the z for which $[\cdot]$ is minimal. In principle, the back-propagation distance should be the same for all grating orientations. The optimal d_i is retrieved for all grating angles and the mean distance d is used. Typically, the relative error in the back-propagation distance is on the order of 4%. If the probe beams have a different intensity, the normalized crosscorrelation between $D_i^{(0)}(z)$ and $D_i^{(1)}(z)$ could be used as well. Even though this is a convenient technique, it requires an additional measuring step in which the diffraction patterns of the sample illuminated by both individual probes are measured.

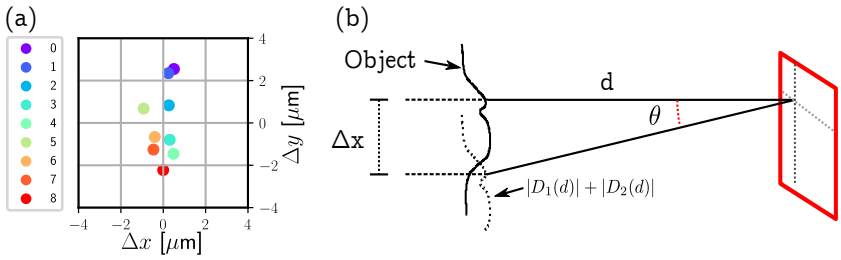

Fig. 4.2: (a): estimated object shifts for probe orientations 1-8 of the USAF target. Most of the shifts are in the vertical direction, indicating that the object was slowly drifting down. (b): Geometrical indication of tilting a probe in order to shift the location of the reconstructed object without affecting the measured intensity patterns. If for a particular orientation i the initial back-propagated image is shifted by Δx with respect to the required position, the overall angle of the two probes $P_i^{(0)}$, $P_i^{(1)}$ is tilted by angle $-\theta$, such that after a new back-propagation using Eq. (4.14), the object estimate is shifted to the desired position.

Aligning measurements sets of different fringe orientations

Taking a reference measurement requires insertion and removal of the sample. Due to instabilities in the setup, the object might not move back to exactly the same location. Additionally, the lenses f_1 and f_2 might suffer from aberrations, and rotating the grating might lead to a rotation of the average direction of the incident beams. Lastly, the average direction of k_y is rounded to the nearest integer FFT bin, leading to slight roundoff errors. To estimate this effect, we computed $D_i(d) = D_i^{(0)}(d) + D_i^{(1)}(d)$ as an estimate for the object after retrieval for all grating orientations i. We then compute the optimal translation of all measurements to make them overlap with the central fringe orientation, using FFT-based phase correlation on the gradient of the images using a DFT based sub-pixel registration method [59, 74]. Typically, the estimated object shift is on the order of a few pixels, as shown in Fig. 4.2a.

One way of aligning the different measurements with respect to each other would be to resample the measured diffraction patterns on the camera. However, as the camera records an interference pattern, it contains modulations at relatively high spatial frequencies and this might lead to sampling artefacts if the required shift is not an entire pixel. Therefore we numerically tilt the probe in such a way that the expected intensity on the camera does not have to be altered. The procedure is indicated in Fig. 4.2(b).

Using a basic geometrical argument, we derive the required additional angle that needs to be applied to Q_i to retrieve the object at a shifted location Δx_i in 1D, after which the same procedure can be applied for the 2D case. Both probe beams need to be tilted by an angle θ defined as

$$\tan\theta = \frac{\Delta x_i p}{d} = Y \tag{4.16}$$

$$Y = \Delta x_i p / d, \tag{4.17}$$

where Δx_i is the required shift in pixels for the object retrieved at angle i, the pixel size is defined by p and the back-propagation distance is given by d. To tilt a wavefront by angle θ, the beam needs to be multiplied with a linear phase slant of steepness $T(\theta)$:

$$T(\theta) = \frac{2\pi}{\lambda} \tan\theta. \tag{4.18}$$

Inserting the required phase slant from Eq. (4.16) leads to

$$\Delta k_{\Delta x_i}(x) = \frac{2\pi}{\lambda} \frac{p^2 \Delta\, x_i}{d} \frac{x}{2N} \tag{4.19}$$

where $\Delta k_{\Delta x_i}(x)$ is the phase retardation that needs to be applied in pixel number x, and N is the number of pixels. This slant is added to the probe estimate $\widetilde{Q}_i$ at the location of the camera. The estimate of the probe at the object location is now given by propagating the corrected probe estimates back to the object location.

$$P_i^{(0)} = \mathcal{P}_{-d}\left[\widetilde{Q}_i^{(0)} \exp\left(\imath\left(\Delta k_{\Delta y_i}(y) + \Delta k_{\Delta x_i}(x)\right)\right)\right] \tag{4.20}$$

$$P_i^{(1)} = \mathcal{P}_{-d}\left[\widetilde{Q}_i^{(1)} \exp\left(\imath\left(\Delta k_{\Delta y_i}(y) + \Delta k_{\Delta x_i}(x)\right)\right)\right] \tag{4.21}$$

Where $\Delta k_{\Delta y}$ is an equivalent term to Eq. (4.19) in the y-direction.

Even after this alignment, there might be a remaining misalignment at the sub-pixel level between probes of different orientations. Therefore, after computing the object update for all measurements j in a particular orientation i, an iterative position update procedure similar to Ref. [70] is used. After all measurements of a particular probe orientation have been processed, the new object estimate and the old object estimate are aligned using 2D crosscorrelation in the Fourier domain. The average probe direction is then updated using Eqs. (4.20)–(4.21). Related techniques based on e.g. intensity gradients [71] can be used as well. Additional details on the alignment optimization procedure can be found in Appendix 4.7.

Probe pattern phase determination

After a reasonable estimate of the individual probe beams has been obtained, the path length difference between the two arms, which determines the position of the maxima of the probe interference pattern, still has to be found for all images. As visible in Fig. 4.3a, the individual fringes are visible in the measured diffraction patterns. However, the position of the fringes will in general be shifted because of the interaction with the probe. Therefore, an accurate estimate of the path length difference requires an accurate description of the object. Therefore, the path length difference estimates are refined after every ptychographical iteration.

To estimate the path length difference between the two probes, we optimize the resemblance between the measured intensity on the camera and the expected

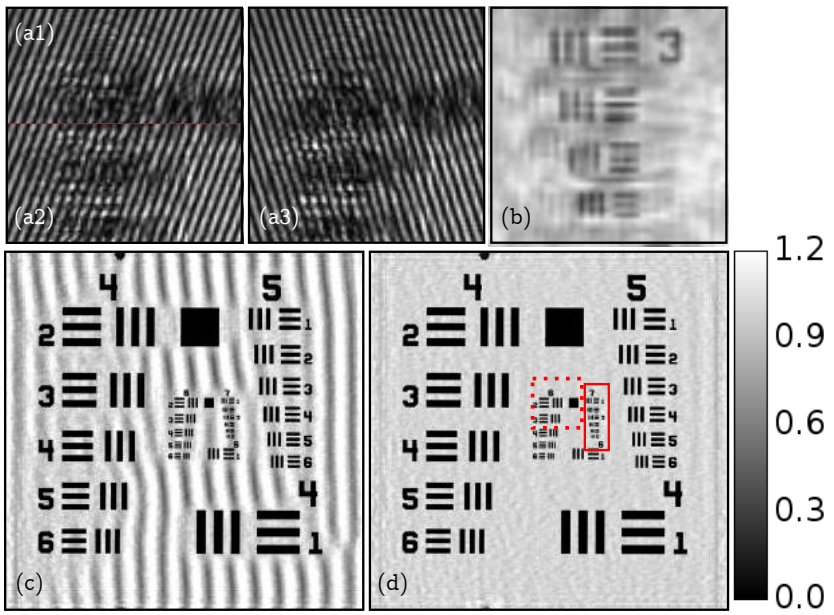

Fig. 4.3: (a1-a3) Measured diffraction patterns for different path length differences (a1-a2) and different orientations (a3). (b) Back-focused image of group 7.3-7.6, using a single diffraction pattern of a single beam, showing artifacts created by the twin image. (c) Reconstructed intensity without taking into account the forward model as defined in Eq. 4.8. The area shown in a1-3 is roughly indicated by the red dashed area. (d) Reconstructed intensity including the forward model to account for imperfect mutual coherence.

intensity given by the current estimate of the object. As only the modulated part is dependent on the path length difference, the background caused by the contributions from the individual beams $I_{i,j}$ is subtracted using the current estimate of these background contributions.

$$I_{i,j}^{\text{mod}} = I_{i,j} - \left|\widetilde{\Psi}_i^{(0)}\right|^2 + \left|\widetilde{\Psi}_i^{(1)}\right|^2 \tag{4.22}$$

Alternatively, the individual measured beams $(I_i^{(0)}, I_i^{(1)})$ can be used if they are available. For a particular measured diffraction pattern $I_{i,j}$ and probes $P_i^{(0)}$ and $P_i^{(1)}$, the pathlength difference $\delta_{i,j}$ can be optimized as follows:

$$\delta_{i,j} = \mathbf{argmax}_\delta \left(F_{i,j}(\delta)\right) \tag{4.23}$$

$$f_{i,j}(\delta) = \langle K_i(\delta) | I_{i,j}^{\text{mod}} \rangle \tag{4.24}$$

$$K_i(\delta) = 2C_i \Re\left(\widetilde{\Psi}_i^{(0)} \widetilde{\Psi}_i^{(1)*} \exp \imath\delta\right) \tag{4.25}$$

Where $K_i(\delta)$ is an estimate of the modulated part of the diffraction pattern, $f_{i,j}(\delta)$ computes the overlap between the modeled intensity and the modulated part of the intensity using the dot product, and $\Re$ means taking the real part.

A further simplification is possible, as $f_{i,j}(\delta)$ is a sinusoidal function. For every pixel in $K_i(\delta)(x,y)$, the expected intensity can be written as a sinusoidal function with an unknown phase $\delta(x,y)$, which is dependent on the phase difference between the two estimates of the camera field for that particular pixel and an overall path length difference. As $f_{i,j}(\delta)$ is essentially a weighted average of all individual (x,y) positions, it will be sinusoidal as well for any reasonable estimate of the camera exit waves $\widetilde{\Psi}_i^{(0)}$ and $\widetilde{\Psi}_i^{(1)}$. Finding the optimal δ is then reduced to finding the maximum of a sinusoidal function with a known period. Using the definition of a discrete Fourier transform, the optimal path length difference can be computed using

$$\delta_{i,j} = \mathbf{Arg}\left(\frac{1}{N}\sum_{i=0}^{N} f_{i,j}(\delta)\exp \imath\delta\right) \quad . \tag{4.26}$$

Where $\mathbf{Arg}[\cdot]$ returns the argument of a complex phasor. Similar techniques are also used for the estimation of fields exiting complex media [79, 80] and digital holography [67], and it is similar to lock-in techniques. For an accurate estimate, N needs to be at least four, but we chose $N = 8$ for a slightly more robust result. In practice it turns out that this gives an accurate estimate of the phase difference after the first few iterations of the ptychography algorithm. Rearranging Eq. (4.24), the estimated phase can be extracted for all frames of a particular fringe orientation in parallel. This is done after processing every full ptychographic iteration. For the first estimate, a random complex initial guess of the object is used.

Fringe frequency adaptation

From the methods described in the previous subsections, in principle all the parameters required for reconstruction can be determined. One additional optimization step, which is not strictly necessary but is found to aid convergence is the adaptation of the probe fringe frequency.

Inserting the sample alters the optical path length between the grating and the camera. While this is a rather small path length difference, it may alter the fringe frequency of the interferogram if the probe beams are not perfectly collimated. Furthermore, in between the acquisition of the reference measurements and the sample measurements for a particular orientation,the grating might rotate by a tiny amount. Even though both of these effects are subtle, the algorithm converges faster if their influence is characterized once before the retrieval routine is started. If these effects are not taken into account, a quadratic phase term may appear in the object, corresponding to the additional path length.

To properly deal with these effects before reconstruction, the measured probe patterns are fitted to Eq. (4.25) while allowing for an additional linear phase

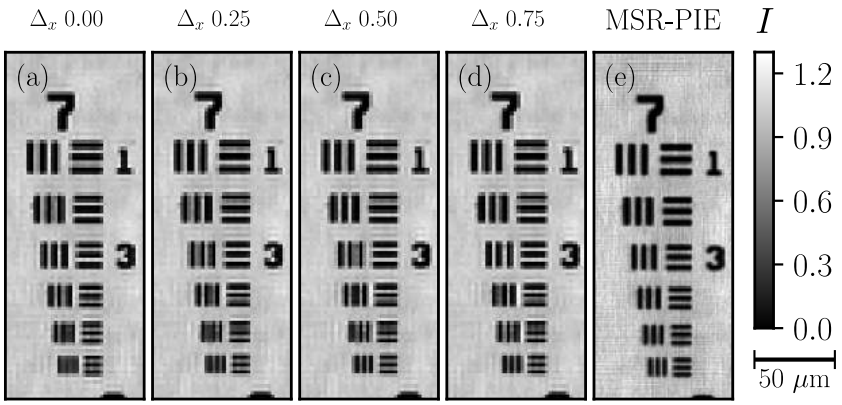

Fig. 4.4: (a-d) Intensity reconstruction of group 7 from a retrieved USAF sample, for a reconstruction with a numerical wavefront tilt corresponding to an object shift of 0, 0.25, 0.50, and 0.75 pixel. The smallest features that can be resolved are dependent on the numerical shift, even though the input data is exactly the same. Reconstructing the data using MSR-PIE (e), reveals that the bars in group 7.6 with a width of 2.2 µm can now be separated.

term to both probe beams with opposite signs, leading to a slight change of the fringe frequency.

4.4 RESULTS

4.4.1 *Performance assessment*

To demonstrate the proposed method and characterize the attainable resolution, a USAF target has been illuminated with laser light at a wavelength of 450 nm, and the resulting diffraction is recorded on a camera with a pixel pitch of 2.2 µm. Nine different fringe orientations are used, in steps of 10 degrees. Four different path length differences are selected for every fringe orientation. Typical measured diffraction patterns are shown in Fig. 4.3(a1)-4.3(a3), and an individual directly back-focussed image is shown in Fig. 4.3(b). The reconstructed intensity is shown in Fig. 4.3(d). The image is sharp and the ptychographic reconstruction manages to completely suppress the twin image visible in Fig. 4.3(c). Some variation in the brightness level of the object is caused by imperfect knowledge of the illumination function. In this case, special care is taken to optimize the modulation contrast of the probe beams. This modulation contrast C_i is about 91±3%. Although this might appear to be so close to unity that the forward model defined in Eq. (4.8) might not be crucial, when the measured modulation contrast is not taken into account the reconstructed intensity is found to suffer from artefacts. This occurs specifically in sparse areas of the object, as shown in Fig. 4.3(c).

To assess the attainable resolution, the area indicated in red in Fig. 4.3(d) is magnified in Fig. 4.3(a). The smallest features that are resolvable in this image

are roughly in group 7, element 4, with a width of about 2.7 µm. However, because the width of the bars is similar to the size of a single pixel on the camera (2.2 µm), the apparent resolution may be limited by the finite pixel size. To investigate the resolution in more detail, we employ Eqs. (4.20) and (4.21) to shift the location of the retrieved object by numerically tilting the incidence angle of all probes by the same amount. The tilt was taken such that the object was only shifted by a fraction of a pixel. We observe a large effect on the width of the smaller bars and which features can be resolved, Fig. 4.4(b)-4.4(d), which is a confirmation that the image quality suffers from pixel size effects. Therefore, the algorithm does not yet take full advantage of the information that is present in the measured diffraction patterns, as is to be expected given the fact that the geometrical detection NA of up to 0.75 should give rise to a resolution well below the pixel pitch.

4.4.2 *Achieving sub-pixel resolution: the mean-SR-PIE algorithm*

For collimated illumination, the ultimate resolution achievable in the Fresnel domain is determined by the pixel pitch of the camera. However, the type of illumination that we employed lends itself very well to subpixel localisation of the position of the fringes [44, 45]. Also, the illumination pattern closely resembles the illumination pattern used in white light structured illumination microscopy, where a periodic illumination is employed to gain op to a factor two in resolution based on the aliasing of higher frequency features[81, 82]. The algorithm that we employ is adopted from the subpixel–PIE, or sPIE algorithm, and is closely related to subpixel ptychography in the farfield as described in [77] and [64, Chapter 4] by Maiden et al and Batey et al. To overcome the limitations imposed by the finite pixel size on the camera, every camera pixel is divided into 2 x 2 sub-pixels. Instead of constraining the intensity of every individual sub-pixel using Eq. (4.8), another forward model is employed to compute the expected camera intensity, by incoherently adding the intensities of all 2x2 sub-pixels. Afterwards the relative intensities of the sub-pixels are scaled by the required factor to ensure that the estimated camera intensity matches the measured camera intensity. However, the relative ratio of the intensity within the sub-pixels is allowed to be almost completely free. The expected camera intensity is computed as:

$$\widetilde{J}'_{g,n,i,j}(x,y) = \widetilde{J}_{g,n,i,j}(2x+0,2y+0) + \widetilde{J}_{g,n,i,j}(2x+0,2y+1) + \widetilde{J}_{g,n,i,j}(2x+1,2y+0) + \widetilde{J}_{g,n,i,j}(2x+1,2y+1) \quad (4.27)$$

where $\widetilde{J}'_{g,n,i,j}(x,y)$ is the expected intensity on the camera, consisting of the incoherent addition of the fields on the sub-pixels. It will have the same dimensions as the original measured diffraction pattern. Similar to previous implementations [77], the highest frequencies in the resulting image have been suppressed to limit noise, for which we use an eighth-order super-Gaussian filter with a width of 95% of image.

Additionally, sometimes the reconstruction may improve by choosing γ slightly lower than one. This feature is not used for Fig. 4.4, but has been taken into account in the data sets discussed in the following sections. When using the mean-SR-PIE algorithm on the same data, the smallest features in group 7 can be easily resolved, corresponding to a resolution of 2.19 µm, as can be seen in Fig. 4.4(e). Increasing the oversampling condition to more than two did not lead to an increase in resolution.

4.4.3 *Imaging complex biological samples: mosquito wing*

To demonstrate the feasibility of the method for larger and more complicated samples, we proceed with a measurement of an entire mosquito (Culcidae) wing on a microscope slide submerged in water. Nine different orientations were scanned with a spacing of 20°, and four path length differences were selected from every image. The back-propagation distance is automatically retrieved at 1.053±0.002 mm. In these measurements only a single lens was used with a focal distance of 25 mm and a grating with a pitch of 630 lp/mm, arranged to provide with fringes at a spatial resolution of roughly four pixels on the camera. The reference measurement employed the empty area next to the mosquito wing, providing a clean view of the probe interference pattern. In order to minimize multiple reflections from the cover glass, the laser power was tuned down to reduce the coherence length. As a result, C_i was typically as low as 62.5±3.6%. The mean-SR-PIE algorithm was used to reconstruct the object, using 50 ptychographic iterations of the algorithm. This approach results in a high-quality reconstruction of both object field and intensity, which are shown in Fig. 4.5. In the phase reconstruction, it is apparent that close the wing has a varying optical thickness close to the veins. The algorithm successfully reconstructs tiny feathers on the edge of the mosquito wing, and even indicates that there are tiny features on the wing structure, which are also visible under a classical intensity microscope. In the central part of the mosquito wing, a vein is visible that seems to gradually disappear. However, in the phase contrast image, it is quite apparent that it continues. This is confirmed by the miscroscope image, where it is hard to track the vein but it remains visible. The different colors of the wing in the microscope image are caused by thin-film interference. In empty areas of the cells, very small feathers are present, which are just about resolved in the reconstruction, as shown in the inset in Fig. 4.5(c1-c3). The reconstructed orientation of the hairs matches the orientation seen in a classical microscope.

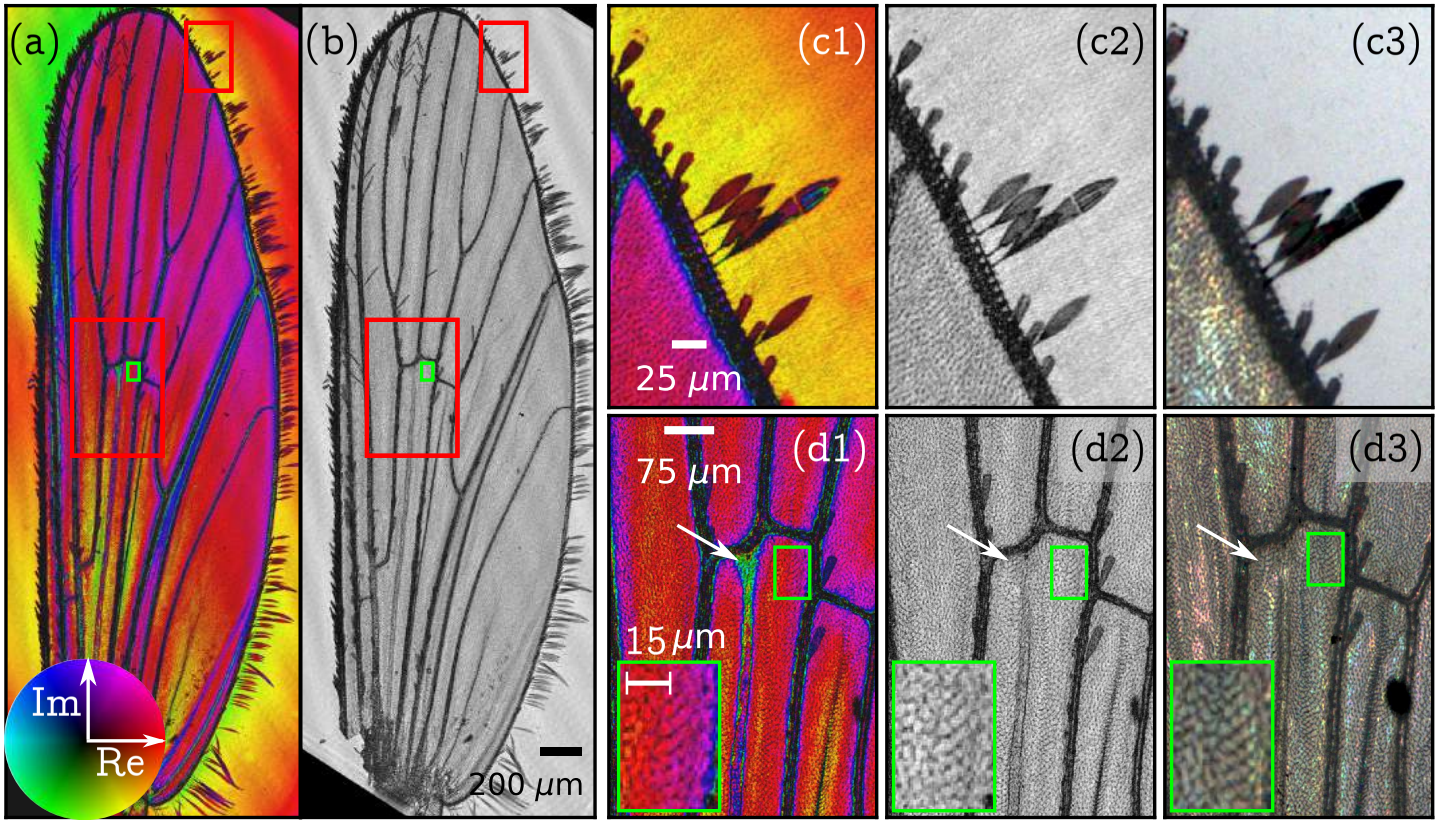

Fig. 4.5: (a) Amplitude-phase reconstruction of a mosquito wing, color represents phase as indicated in the lower left corner. (b) Amplitude of reconstructed field. (c1) A detail of the edge of the wing shows that the optical thickness increases from the edge to the center of the cell. (c2) Amplitude contrast closely resembles the smallest features visible with a microscope at similar resolution (c3). (d1) A thin vein in the center (indicated by the white arrow) can easily be tracked with the amplitude-phase reconstruction but is hardly visible in the amplitude reconstruction (d2) or under the microscope (d3). The structure within each cell is caused by tiny hairs and is properly reconstructed as shown in the green inset.

4.4.4 *Live animal imaging:* C. elegans

The mosquito wing lends itself very well to ptychographical imaging because it is a very thin sample. To show that our system is capable of imaging thicker samples, we also image a biological specimen of living anesthesised *C. elegans*, with a typical diameter of 35 µm, suspended in a thick layer of agar. The resulting reconstructed object images are shown in Fig. 4.6. The internal structure of the nematode is too small to be imaged effectively with the standard PIE routine. Again, using the mean-SR-PIE leads to restoration of image features that are also visible in the microscope image. Especially the edge of the worm can suddenly be resolved much more clearly, and details can be seen in the uterus that were not there before and which seem to match a conventional bright-field microscope image (Fig. 4.6(c)). However, the microscope image is not fully identical to the reconstructed results. This is mainly because of the optical sectioning intrinsic to incoherent bright-field detection, which is more challenging in our setup based on on coherent illumination. Instead, the reconstructed intensity resembles an overall attenuation throughout the entire worm.

4.5 DISCUSSION AND CONCLUSIONS

We have demonstrated a high-resolution computational imaging system based on ptychography with interference pattern illumination. The optical hardware involved is straightforward to implement, requires no careful alignment, yet the microscope is able to achieve quantitative phase contrast with a high resolution and a fast convergence rate. Moreover, experimental variations such as sample drift can be compensated during the post-processing of the measurements.

It would clearly be advantageous to remove the need to measure the individual beams $I_i^{(0)}$ and $I_i^{(1)}$ separately, as it would allow more straightforward data acquisition and measurement automation. In the current preprocessing routine this is not possible. However, the ptychographical reconstruction procedure itself does not rely on these individual beam images, and it should be possible to obtain the calibration measurements without relying on the individual beams. Currently, the individual images are required for auto-focusing and obtaining the object shifts for different grating orientations.

The autofocusing method can be extended not to require the individual diffraction images. An estimate of the incoherent background can be obtained by looking at the largest singular vector of all measured

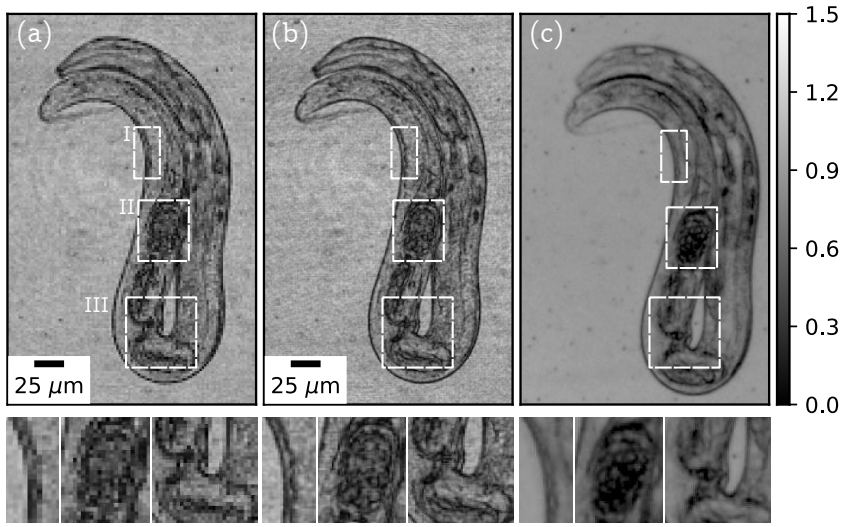

Figure 4.6: (a) Reconstructed amplitude image of an anesthesized *C. elegans* worm, with three insets, showing the edge of the worm (I), eggs (II) and the uterus (III). While the uterus can be recognized, most of the other features are not resolved. (b) Same dataset reconstructed with the s-PIE algorithm. The increase in resolution allows to see that the edge of the worm consists of two layers (I). Some egg-like features are visible (II), and more detail can be seen in the uterus. (c) Conventional bright-field microscope image of the same worm. In order to enhance the contrast in dark parts of the worm, the amplitude is shown instead of the intensity.

diffraction patterns for a particular orientation i. This will closely resemble $I_i^{(0)} + I_i^{(1)}$, leading to an image with two displaced objects. From the internal symmetry in this image, the back-propagation distance could be extracted too. In order to determine the average object shifts between measurement sets at different orientations, the meanPIE algorithm can be run for only a few iterations using only patterns corresponding to a single grating orientation, and the object estimates can be used to determine the shifts. These enhancements will mainly benefit a setup where the probe beams can be turned on and off repeatedly, for instance when using a spatial light modulator to create the probe beams.

FUNDING

Netherlands Organisation for Scientific Research (NWO) (project nr 13934); European Research Council (ERC) (ERC Starting Grant 637476).

ACKNOWLEDGMENTS

We thank Joleen Traets and Jeroen van Zon for providing us with the *C. elegans* sample.

DISCLOSURES

The authors declare that there are no conflicts of interest related to this article.

4.6 APPENDIX

4.6.1 *Selecting phase-shifted measurements*

The limited stability of the measurement system prevented accurate control over the phase of the interference pattern in these experiments. Therefore, the camera records 50 frames with an a priori unknown fringe phase (optical path length difference between the two beams) for every fringe orientation. Only two to four out of these 50 images are required for the final analysis, provided that images at the correct phases are selected, such that each area of the sample is illuminated by least one image. Also, if a new intensity image can be written as the linear combination of two measurements that are already included in the analysis, it will not provide with useful additional information that can be obtained from the new measurement.

The fringes in the illumination beam are visible in the measured diffraction patterns. Therefore, one way of selecting the measurements would be to extract the overall path length difference δ for every individual measurement and select the measurements that are closest to an equidistant set ranging from 0 to 2π. However, this is computationally expensive and the due to vibrations the exact fringe spacing and orientation might vary slightly Instead, we employ a method that aims to include new measurements based on minimal overlap with linear combinations of already included measurements. It is essentially a modified version of the Gram-Schmidt algorithm used to orthogonalize a matrix. A first image I_0 is selected based

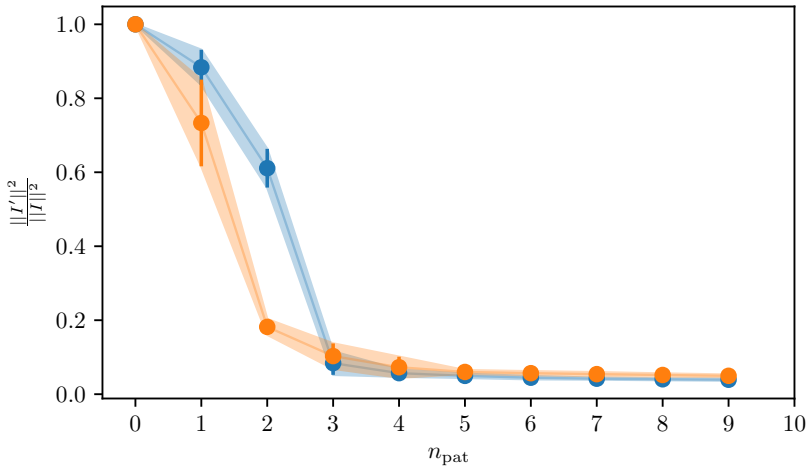

Fig. 4.7: l_2 norm of the remaining patterns in I'_n after selecting n_{pat} measurements using the described procedure, for all orientations of the dataset used to reconstruct the USAF sample. For the orange dataset, the background patterns $I_i^{r(0,1)}$ have been subtracted, indicating that typically only two patterns are required to extract most of the information. For the blue dataset, the raw measurements have been used without background subtraction, which seems to give slightly better results when more than three measurements have been included.

on minimal cross-correlation with all of the other images. The other images are orthogonalized with respect to this measurement by subtracting I_0 using the Gram-Schmidt procedure.

$$I'_n = I_n - \frac{\langle I_n | I_0 \rangle}{\langle I_n | I_n \rangle} I_0 \tag{4.28}$$

Where I_n is the intensity of the n-th measurement, and $\langle I_n | I_0 \rangle$ is the dot product of images I_n and I_0 both represented as a one-dimensional vector. After this operation, I'_n contains all the information in I_n that cannot be expressed by I_0. Therefore, the index n of the next measurement which gives the optimal amount of additional information is the one with the highest l_2 norm:

$$n_{\mathrm{next}} = \mathbf{argmax}_n \left(\|I'_n\|_2 \right) \tag{4.29}$$

where n_{next} is the index of the next frame to be included in the analysis. The procedure is repeated to get the desired number of measurements, replacing I_n with I'_n in Eq. (4.28) after every iteration.

In principle, a cosine-modulated interference pattern with an a priori unknown phase can be expressed using only two signals, a sine and a

cosine [78], provided that the background is measured as well. Therefore the minimal number of patterns would be two if we can select two measurements that are exactly $\pi/4$ out of phase. However, for improved robustness we choose to include four patterns in the analysis. We do observe that typically the first two images that are selected are about $\pi/4$ out of phase.

One way of investigating the amount of additional information in the measurements data is to look at the norm of $\sum_n I'_n$ after including every new measurement, shown in Fig. 4.7. As the background images were also measured, the intensity of beam 1 and beam 2 can be subtracted from I before the analysis. However, in both cases it seems that after including three images most of the information is present and adding more images does not significantly improve the image reconstruction.

4.7 ITERATIVE ALIGNMENT OPTIMIZATION

Even after the initial alignment as described in the main text, the objects might be shifted with respect to each other by a fraction of a pixel size. We adopted a straightforward alignment procedure that is typically used in Fourier ptychography to correct for small shifts, but other methods could be used as well [70, 71]

After processing all camera images of a particular fringe orientation, if the object was misplaced, the object estimate will have shifted a little bit in the direction of the misplaced object. Our algorithm relies on detecting this shift and numerically tilting the probe in order to compensate this difference. In similar methods, this stepsize is magnified, but in our case the feedback is strong enough that this did not help. The difference with the object before processing a particular fringe orientation is computed as $\Delta = O_{c,n} - O_{g,n}$. A new estimate of the object is computed by amplifying this difference:

$$O' = O_{g,n} + 5\Delta \tag{4.30}$$

This magnification is not strictly necessary, but it helps convergence. Then the optimal shift is found between $O_{g,n}$ and O' aligning the objects using FFT-based crosscorrelation using subpixel accuracy [59] as implemented in the scikit-image python package. Using Eq. (4.19), all probes for this grating orientation are tilted in order to optimize the overlap. Even though this algorithm will not work for large differences, it does converge for small angles.

4.8 REQUIREMENTS ON THE NUMBER OF DIFFRACTION PATTERNS

In the original implementation of PIE, the object was updated as defined in Eq. 4.9 after processing each probe-response pair. In our algorithm, we average all updates after processing all fringe patterns of a particular fringe orientation. To investigate the difference, we investigated how well the object is reconstructed when only a subset of the full measurement range is taken into account. The results are shown in Fig. 4.8.

As visible in the top row, including eight or nine different orientations has a minimal impact on the reconstructed result. However, when the number of images is reduced to six, the classical PIE algorithm with sub-pixel resolution starts to fail, even though mean-SR-PIE still provides acceptable image quality. The reconstruction artifacts resemble Fig. 4.3c, where the laser coherence is overestimated. When the number of measurements is decreased to only three, but the number of phases per orientation is increased to eight, the object is still properly constructed. In this case, increasing the grating angle intervals leads to an improved reconstruction. For only two orientations, the normal object reconstruction seems to fail completely for the normal s-PIE, while mean-SR-PIE is still able to reconstruct some features.

For more complicated samples such as the mosquito wing, this analysis does lead to different numbers for the minimum amount of required measurements, and it is to be expected that the required number of measurements is dependent on the complexity of the sample. Therefore we cannot claim a true "minimal" number of measurements, although it is reasonable to conclude that more than one fringe orientation is required for normal image reconstruction (as also indicated by [76]), and more than two fringe orientations for sub-pixel resolution. .

4.9 TABLE WITH RETRIEVAL PROPERTIES

The settings used for the reconstructions are listed in Table 4.1.

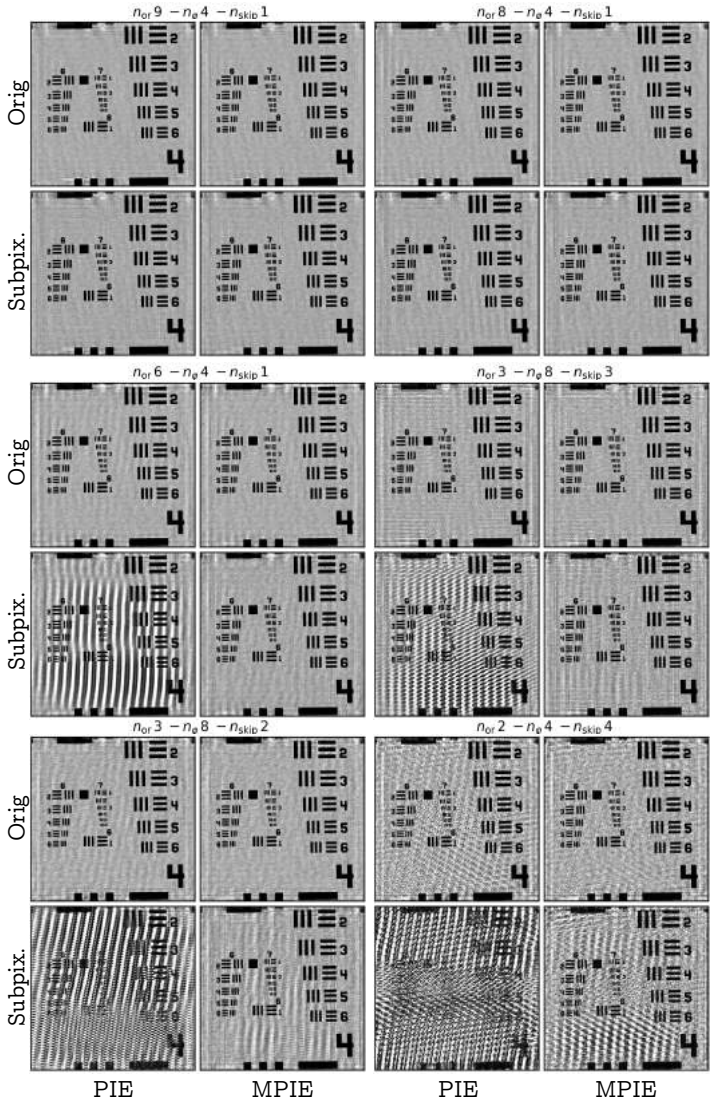

Fig. 4.8: Reconstruction results for different numbers of input measurements. Three parameters have been varied: 1) the number of orientations n_{or}, 2) the number of fringe patterns per orientation n_φ, and 3) the number of orientations that are skipped when selecting a subset n_{skip} (i.e. n_{skip}=2 means 2× larger angle between consecutive orientations). The left column in every image is the retrieval result for the regular (S)PIE, right column is retrieved using our mean-(SR)-PIE. The top row (Orig) is without sub-pixel resolution, bottom row (Subpix.) is with 2x2 sub-pixel resolution. The number of iterations has been adjusted in such a way that the total number of feedback loops have been processed is $n_{\text{its}} = 1836/(n_{\text{or}} \cdot n_\varphi)$.

Table 4.1: Overview of settings used for retrieval of all the objects in the paper. d: Automatically retrieved back-propagation distance. n_{or}: Number of fringe orientations measured. n_ϕ: Number of diffraction patterns selected per fringe orientation. n_{its}: Number of ptychographical iterations used for reconstruction. λ: Illumination wavelength. $\overline{C}$: Average coherence as extracted from the reference measurements. α: Angle between different grating orientations. CM: Coherence multiplier as defined in the main text.

Sample	d [mm]	n_{or}	n_ϕ	n_{its}	λ [nm]	$\overline{C}$	α (deg)	CM
Mosquito	1.053±0.002	9	4	51	450	0.63 ± 0.03	20	1
USAF	1.311±0.003	9	4	51	450	0.90 ± 0.03	10	0.95
Worm	1.361± 0.005	8	4	51	520	0.80 ± 0.02	15	0.95

Part II

IMAGING THROUGH MULTIMODE FIBERS

5

MULTIMODE-FIBER ENDOSCOPY

5.1 INTRODUCTION

Much though the human body appears to be a solid object, most of its organs are in fact more or less hollow. When a visual inspection of the interior of such an organ is required, a tiny camera attached to a cable can be inserted, which is called an endoscope. This turns a rather big surgery into a minimally invasive operation. Endoscopes are widely used nowadays to visualise areas that are difficult to reach otherwise. Essentially, an endoscope is no more complicated than a device that allows optical access to the interior of the specimen from the outside world. First endoscopes in use were no more complicated than a hollow tube called a *lichtleiter*, literally light guide, which was used to inspect natural cavities near the surface of the human body [83].

Technological advances have resulted in much more sophisticated endoscopes: flexible endoscopes with a higher resolution and a smaller diameter. Their increased length allows access to more remote areas of the human body. Most larger modern endoscopes feature a chip-on-a-tip design, shown in Fig. 5.1(a). A tiny camera plus a miniaturized lens are mounted on the distal end of an endoscope. The images recorded by the camera are electronically transmitted to the operator outside the body. While these devices offer a high resolution and can be made very flexible, the smallest diameters achieveable are still rather large compared to the smaller cavities in a body. Therefore their use is limited to imaging larger cavities, such as the gastro-intestinal tract.

For sensitive tissues, such as brain tissue, a high resolution is required together with a small device footprint. This requires a different design. Instead of an active endoscope in which the image is already recorded inside the patient, a passive image guide is employed. The device transfers the optical information directly from the distal end to the proximal end, after which the image can be sampled outside the body using a camera. One of the main advantages of such a design is the more elaborate optical setups that can be employed, as there are no footprint constraints to the optical setup outside the body. For instance, after a calibration procedure the imaging depth of focus at the distal

end can be controlled from the proximal end [84, 85]. Other examples include Raman imaging [86], extended depth of focusing [87], two-photon microscopy [88], superresolution imaging [89, 90], light-sheet microscopy [91–93] and higher order nonlinear microscopy [94–96]. These developments have paved the way for more advanced *in situ* analyses alleviating the need to do a biopsy.

A very direct way of transmitting an image is based on a multi-core imaging fiber. Multi-core imaging fibers are big fibers consisting of a large number of individual cores. Every core acts as an individual pixel, see Fig. 5.1(b). The image is sampled by the individual cores on the distal end and transmitted to the proximal end, where the fiber facet is imaged again. From an imaging point of view, the cores of the fiber should be as closely packed as possible. However, to prevent core-to-core coupling, a relatively big spacing between fiber cores is required. Depending on the diameter of the device, these devices can be made reasonably flexible. These fibers are typically arranged in a grid, but recent developments showed that using a more randomized structure increased the imaging capabilities and field of view [84].

In order to obtain an even higher resolution, a series of lenses can be used transmitting the image from inside the object to outside the object, Fig. 5.1(c). Although a higher resolution can be obtained, these devices are rigid, limiting the application areas. Replacing the lenses with an appropriately designed graded-index rod can enable a further resolution enhancement, Fig. 5.1(d). The refractive index profile of such a rod is parabolic. Therefore, a straight segment acts like a continuous lens, which is cut to the right length to enable imaging from the distal end onto the proximal end.

It becomes challenging to improve the performance of such a device. The fibers of a multi-core fiber require a certain diameter to guide the light efficiently, and minimum spacing is required in between the individual fiber cores to prevent crosstalk between neighboring fibers. Distal optics can be used to improve resolution, but they will decrease the field of view, keeping the same number of independent pixels. The resolution of a graded-index rod can be increased by increasing the steepness of the refractive index profile, similar to shortening the focal length of the lenses for the same diameter. As such, more lenses are required to transmit the image over the same distance, leading to increased imaging aberrations. As a grin rods typically suffer from positive spherical aberration, increasing the numerical aperture of a grin lens with a similar length will lead to a severely aberrated imaging system [97]. Therefore, even though the system might support a higher resolution, imaging aberrations will prevent it from being used in an effective way.

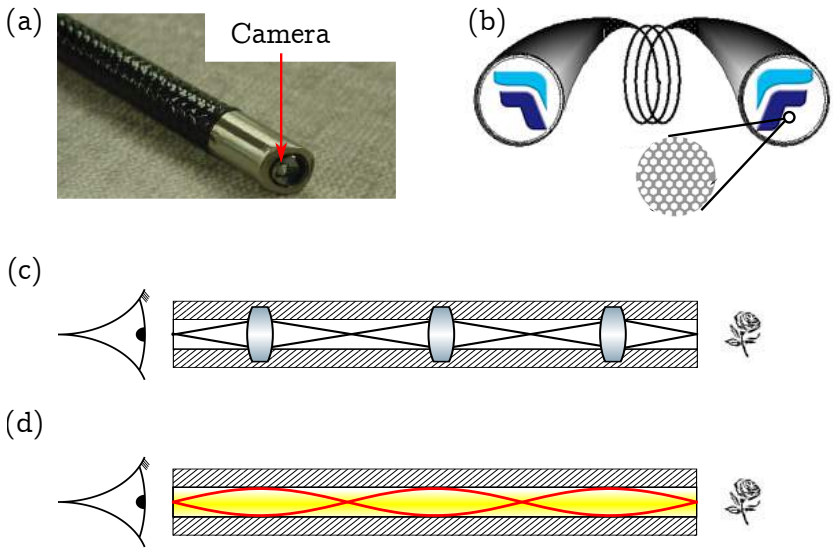

Fig. 5.1: Different endoscopic designs conceptually drawn. (a): Chip-on-tip endoscope. (b): multicore imaging fiber. (c): Lens array rigid endoscope. (d): Graded index rod lens. (a) and (b) were adopted from initial images which are a courtesy of Myriadfiber Inc.

Instead of attempting to achieve an optical imaging system with perfect imaging capabilities, as an alternative the imaging imperfections can be calibrated and compensated for using a device shaping the wavefront on the incident and/or returning light, conceptually drawn in Fig. 5.2, in a similar fashion as adaptive optics systems [98, 99]. For instance, using a low-order adaptive optics system it was shown that diffraction-limited resolution can be obtained with a long straight graded index rod for two-photon microscopy that was previously suffering from imaging aberrations [100]. When more severe aberrations are present, the required aberration corrections will in general be dependent on the imaging position on the distal end. In the most extreme case, the required aberration compensation to image a particular output field will be completely determined by the output position. However, if these aberrations are completely known, imaging is still possible in a number of ways, either using the known aberrations to project a series of spots across the distal end and measuring the overall reflectivity [91, 101, 102], making use of averaging techniques [92] or using optimization based approaches [103]. Even though this approach is much more elaborate than a simple imaging device, it is a very flexible approach and a lot of different imaging modalities have already been demon-

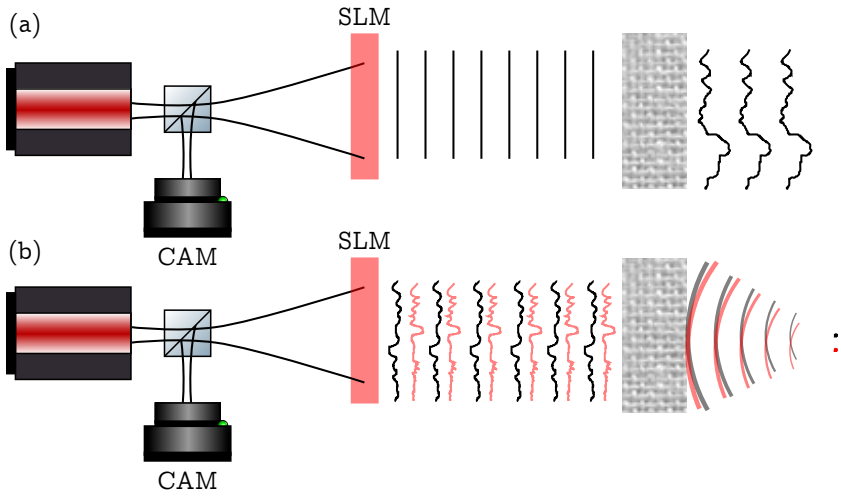

Fig. 5.2: Complex photonics concept for turning anything into a lens: Before correction, (a), a collimated beam hits a scattering sample. After propagating through the sample, a complex interference pattern appears. After calibrating the setup (b), the wavefront shaping device is able to cancel the aberrations induced by the system and as such the light on the distal end of the device can be focused into a spot. By changing the spatial pattern, the focal position can be scanned (indicated by the gray and the red spot). To image something hidden on the distal end, the backreflected light can be monitored on a camera.

strated. The major advantage of these techniques is that *anything* that guides the light from inside to outside can be turned into an endoscope, and detailed knowledge of the light-guiding material is not necessarily required.

As a convenient choice for an endoscope, a flexible multimode fiber can be used. In a multimode fiber, light can travel in different paths through the fiber, and the resulting beam on the distal end is the result of complex interference of light traveling through all possible pathways. The exact optical behaviour is determined by the refractive index profile of the waveguide. There are a wide range of optical fiber designs available, but the most common designs are step index fibers (Fig. 5.3(a)), in which the refractive index profile resembles a box with a width and a height, or a graded index refractive index profile (Fig. 5.3(b)), in which the refractive index profile resembles a parabola. When an image is projected onto the distal end of the fiber, in general a complex interference pattern appears on the proximal end, which is called a speckle pattern. Even though this process might appear to be random, it is deterministic: when the same field is injected into the fiber on one end, and the fiber is fixed in the same position, the same speckle pattern will appear every time. When light transport through

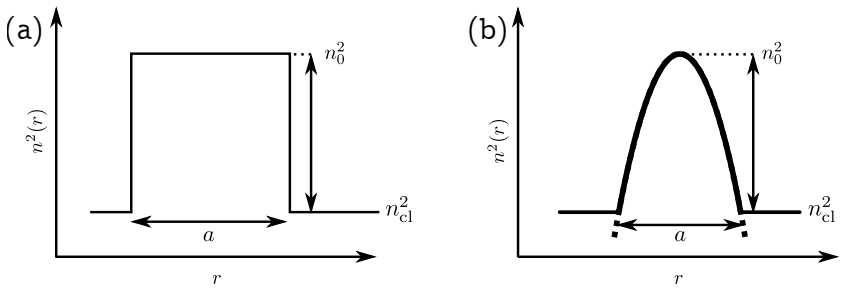

Fig. 5.3: Two common refractive index profiles for optical fibers, a step index fiber (a) and a graded index fiber (b).

the fiber is known, for instance because it has been measured, this knowledge can be employed to reconstruct what was illuminating the distal end of the fiber, resulting in an imaging system through a fiber.

Another advantage is that multimode fibers are flexible, allowing easier access to difficult to reach areas. However, when the fiber is bent, the light transport through the fiber is affected and the system will have to be recalibrated, or the resulting images will suffer from severe artifacts. Therefore, even though the fiber itself is flexible, it must be held fixed in between calibration and subsequent imaging, which presents a severe limitation to the applicability.

Optical fibers are not random media, but very carefully engineered waveguides. In 2015, it was shown that for step index fibers it is possible to predict the system response rather than measure it, provided detailed knowledge about the fiber refractive index profile is available [104]. Also, changes to the system response when the fiber is bent can be predicted. This opens up a lot of new possibilities as the requirement that the fiber cannot be moved is now reduced to that the bends have to be known. Nevertheless, this method requires accurate knowledge of the curvature of the fiber, which can be difficult to obtain if the endoscope is hidden inside a moving body.

In the next chapter we will explain why graded index optical fibers are much more resilient to bending than the more commonly used step-index optical fibers. The chapter is a verbatim copy of the original publication. As it presumes background knowledge both in complex photonics as well as in waveguide theory, the required mathematical toolbox is introduced shortly here. The interested reader can find background information in Refs. [104–107]. In chapter 8, further improvements to the employed optimization technique are sketched.

5.2 TRANSMISSION MATRIX APPROACH

Previously we mentioned that the required aberration compensation for every output point can be characterized. For a practical realization, the inverse problem is easier to measure: for every input point, we measure the resulting output field. Afterwards, we can invert this relationship. For linear optics, the resulting output field of any incident wave entering a system can be written as a matrix-vector equation [108]:

$$E_{\text{out}} = T \cdot E_{\text{in}} \,. \tag{5.1}$$

Here, E_{in} is a column vector where the entries constitute the field sampled across a 2D grid and E_{out} is the output wavefield. T is called the transmission matrix and it specifies the complex transformation from the input location to the output location. In this case, E_{in} and T are both represented in a point basis, where every entry represents a point on a 2D grid. Therefore the entries in T are determined by the complete optical system, including any misalignments, free-space propagation, or multiple scattering occurring in between the input plane and the output plane. The columns of this matrix represent the resulting field after focusing a beam in a particular position. The rows represent the required fields in order to focus on a particular output position. As an example, consider a system where light propagates from location $z = 0$ over a small distance to $z = L$ through free space. In this case, every column of the transmission matrix will correspond to Fresnel propagation from $z = 0$ to $z = R$ for a spot sampled across the proximal end. The structure of the transmission matrix is dependent on the optical system and we will show that we can use a model to explain the observed transmission matrix.

A number of techniques exist to measure the transmission matrix [25, 109–114]. We will measure the columns of the transmission matrix directly. A spot is scanned across the proximal end and the resulting field is measured in amplitude and phase by interfering with an external reference beam, shown schematically in Fig. 7.1. It is important to keep track of any drifts between the reference beam and the imaging beam, and an in-house calibration technique was used, in which the drifts are calibrated so they can be compensated for during subsequent analysis.

A big advantage of directly measuring the transmission matrix of an optical system is that it allows a lot of flexibility during postprocessing. Using Eq. 5.1, for any incident field, the resulting field can be

computed. Therefore, the transmission matrix only has to be measured once before it can be employed for all kinds of analysis. For instance, misalignments in the optical setup can be calibrated out afterwards. In the coming experiments it will be crucial that the location and angle of incidence of light hitting the waveguide are accurately known on both proximal and distal end. As it is not possible to align this with sufficient precision a priori, these parameters will be retrieved from the measured transmission matrix.

5.3 WAVEGUIDE ANALYSIS

In this section a short overview of waveguide theory is given, more specifically how to predict the transmission matrix of a waveguide with a known refractive index profile. We then explain how to incorporate the effect of small deviations from the refractive index profile on the observed transmission matrix using first-order perturbation theory. Lastly we expand on how to verify a measured transmission matrix to a model of these waveguides.

5.3.1 *Light propagation through a waveguide*

In general, when a particular electric field is coupled into a waveguide such as an optical fiber, the resulting output field has a different spatial structure. However, some fields remain unperturbed up to an overall phase delay [104, 106, 115]. We call these spatial field distributions propagation invariant modes (PIMs), or eigenmodes of the system, and they are solutions to the Helmholtz equation for that waveguide [116, 117].

In the next chapters we will consider waveguides with a perfectly parabolic refractive index profile extending to infinity.

$$n^2(r) = n_0^2 \left(1 - \frac{r^2}{b^2}\right), \tag{5.2}$$

Here, $n(r)$ is the refractive index profile, r extends to infinity, n_0 is the refractive index on the axis and b is a scaling parameter. In real fibers, n becomes constant beyond a certain radius (in the cladding), which we will not take into account. This medium will act as a continuous lens. When a collimated Gaussian beam is coupled into such a waveguide, it will be focused after propagating a distance $2\pi b/4$. However, for a very specific beam diameter, the natural divergence of the beam will be exactly counteracting the focusing behavior of the waveguide, leading to a beam that is unaffected by propagation. We call this the lowest

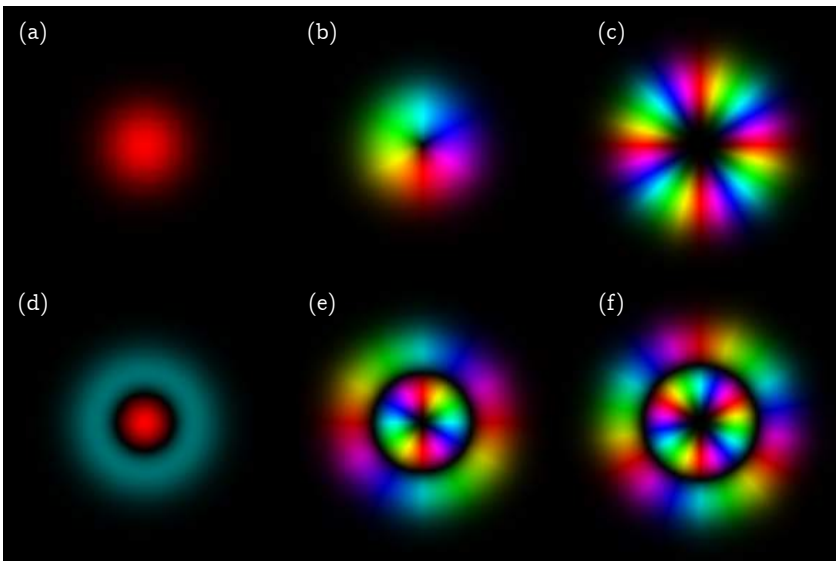

Fig. 5.4: Example Laguerre gaussian fiber modes. (a)-(f): ψ_{00}, ψ_{10}, ψ_{40}, ψ_{01}, ψ_{21}, and ψ_{31}.

order PIM, or the ψ_{00} mode, as we will see later. The size of this beam is determined by the steepness of the refractive index profile.

The ψ_{00} PIM is just one of the many waveguide solutions. The other guided modes are given by [118, 119]:

$$\begin{aligned}\psi_{l,m}(r,\varphi,z) &= \sqrt{\frac{\alpha}{2\pi}\frac{2m!}{(m+|l|)!}}\exp\left(-\frac{\alpha r^2}{2}\right)\\ &\times \left(\alpha r^2\right)^{|l|/2} L_m^{|l|}(\alpha r^2)e^{il\varphi}\, e^{i\beta_{l,m}z}. \qquad (5.3)\\ \psi_{l,m}(r,\varphi,z) &= \psi_{l,m}(r,\varphi,z=0)\, e^{i\beta_{l,m}z} \qquad (5.4)\end{aligned}$$

Here, $L_m^{|l|}$ are associated Laguerre polynomials, $\alpha = kn_0/b$, $k = 2\pi/\lambda$ is the vacuum wave number, $l \in \mathbb{Z}$ is the orbital angular momentum (OAM) index of the PIM, and the index $m \in \mathbb{N}_0$ determines the number of radial nodes [106], and z is the coordinate along the fiber. A few example modes are shown in Fig. 5.4. These modes are orthogonal when integrated over the surface over the fiber.

$$\int_A \psi_{lm}(r,\phi,z)\psi^*_{l'm'}(r,\phi,z)\,\mathrm{d}A = \delta_{ll'}\delta_{mm'} \qquad (5.5)$$

When a fiber mode ψ_{lm} is launched into a waveguide, after propagating a distance L it will acquire an overall phase of $\exp(\imath\beta_{lm}L)$, but the transverse spatial profile will be unaffected.

The propagation constants of these PIMs will be dependent on their spatial structure, where the lowest order mode has the highest propagation constant. The propagation constant of every mode is given by

$$\begin{aligned}\beta_{l,m} &= \sqrt{k^2 n_0^2 - 2\alpha(|l| + 2m + 1)} \\ &\approx kn_0 - \frac{|l| + 2m + 1}{b}. \end{aligned} \tag{5.6}$$

When an electric field is coupled into a fiber which cannot be described as a single eigenmode, multiple fiber modes will be excited based on the spatial overlap between the incident field and the fiber modes. At the distal end, all of these modes interfere after acquiring their respective modal phase, resulting in a complicated interference pattern that is usually referred to as a speckle pattern. More specifically: the incident electric field is decomposed into its modal constituents and their modal phases are computed based on the fiber length.

$$C_{lm} = \int_A \psi_{lm}(x,y) E_{in}(x,y)\, \mathrm{d}x\, \mathrm{d}y \tag{5.7}$$

$$E_{\text{out}} = \sum_{l,m} C_{lm} \psi_{lm}(x,y) e^{i\beta_{l,m} z} \tag{5.8}$$

Where $\psi_{lm}(x,y) = \psi_{lm}(x,y,z=0)$ is the (l,m)-th mode evaluated at $z = 0$ sampled in Cartesian coordinates. . E_{in} is the incident electric field on the fiber, C_{lm} is a vector with the modal coefficients of E_{in}, A extends over the surface of the fiber and E_{out} is the output electric field.

Eqs. (5.7) and (5.8) represent a basis transformation from a basis of points into a basis in PIMs with coefficients C_{lm}, propagation in this basis, and an inverse transformation from PIMs to a point basis.

A transmission matrix is essentially a prediction of the responses of the waveguide for every point sampled on a grid. To predict the transmission matrix of a piece of fiber of length L across an $N \times N$ grid, we create a discrete representation by sampling every point across a 2D grid on the proximal end and compute the resulting output field on the distal end across another 2D grid in a point basis. This can be efficiently written down in terms of linear algebra, using the following notation.

$$\Psi = \left(\vec{\psi}_{-l0} \ \dots \ \vec{\psi}_{l0} \ \vec{\psi}_{-l1} \ \dots \ \vec{\psi}_{lm} \right) \tag{5.9}$$

Where $\vec{\psi}_{lm}$ is a column vector defined as

$$\vec{\psi}_{lm} = \frac{1}{B_{lm}} \left(\psi_{lm(0,0)} \ \psi_{lm(0,1)} \ \dots \ \psi_{lm(0,N)} \ \psi_{lm(1,0)} \ \dots \ \psi_{lm(N,N)} \right)^T .$$

Here, $\vec{\psi}_{lm}(x,y) = \psi_{lm}(x,y,z=0)$ as defined in Eq. (5.3) and B_{lm} is a normalisation constant, defined as$B_{lm} = \|\psi_{lm}(x,y;z=0)\|_2$. In other words, the columns of Ψ consist of fiber eigenmodes sampled across an $N \times N$ grid reshaped into a $1 \times N^2$ vector. Upon propagation, all modes acquire an overall modal phase, which can be conveniently expressed as a diagonal matrix. Using this notation, the expected output field of a waveguide for any input field E_{in} in a point basis can be written as a series of matrix products:

$$E_{\text{out}} = \Psi_{\text{d}}^{\dagger} M \Psi_{\text{p}} E_{\text{in}} \tag{5.10}$$

$$M = \text{diag}\left(\exp\left(\imath \beta_{lm} L\right)\right) . \tag{5.11}$$

Here, Ψ_{p} is a mode matrix sampled on the proximal end and Ψ_{d} is a mode matrix sampled on the distal end. When the sampling on proximal and distal end is identical, Ψ_{p} and $\Psi_{\text{d}}$are identical, but in a practical experiment the sampling might be different and the number of pixels on the proximal end (N^2) might be different from the number of pixels sampled on the distal end (N_2^2). There is no added value in having $N^2 \neq N_2^2$ but in an experimental setting this might not be avoidable, for instance because the camera pixel size cannot be chosen freely. A preprocessing step is employed to make sure that pixels that do not carry any information are not taken into account, and to make sure that $N \approx N_2$. Eq. (5.10) can be recognized as a basis transform: The incident electric field is decomposed from a point basis into a PIM basis, propagation through the waveguide is computed by adjusting the modal phases, and they resulting output field is computed by changing back into the original point basis. The first three components of Eq. (5.10) represent the transmission matrix in a point basis: They specify the waveguide response to a general input field E_{in}.

$$T^{\text{mod}} = \Psi_{\text{d}}^{\dagger} M \Psi_{\text{p}} \tag{5.12}$$

Where T^{mod} is the expected transmission matrix of the system with shape $N^2 \times N_2^2$. An interesting point is the attainable resolution when imaging through a waveguide with a fixed number of guided modes. For intensity imaging, the ultimate resolution attainable is restricted to four times the number of guided modes, due to the squaring inherent

in converting fields into intensities, which was demonstrated experimentally using an optimization-based imaging approach [103].

5.3.2 *Refractive index profile deviations*

Even though the refractive index profile of an optical fiber is usually of a very high quality, fibers are not perfect and this can affect the modal propagation constants, which becomes more apparent for longer fibers. In many cases, there is a small dip in the center of the core of a graded index fiber [120], which affects all modes with any intensity in the core. In this case, the proposed fibermodes are no longer true eigenmodes of the fiber. In this section we will cover how to use first-order perturbation theory to predict the effect of a small modulation in the refractive index profile on the propagation velocities of the guided modes. To that end, we will only compute the changes in propagation speeds, but we will not consider any modal coupling based on the refractive index profile alterations.

We express the new refractive index profile as the old refractive index profile plus a refractive index aberration function $\Delta n(r)$.

$$n^2(r) = n_0^2(r) + \Delta n(r) \tag{5.13}$$

Where $n_0(r)$ is the refractive index profile of the idealized waveguide as defined in Eq. (5.2), and $n(r)$ the actual refractive index profile. Separating $\Delta n(r)$ into a shape $dn(r)$ which is normalized and a strength s, we get:

$$n^2(r) = n_0^2(r) + s\, dn(r) \tag{5.14}$$

The new propagation speeds can be calculated by computing the overlap integral between the individual modes and the refractive index profile aberrations [107]:

$$\beta_{new}^2(l,m) = \beta^2(l,m) + \beta_{abb}^2(l,m) \tag{5.15}$$

$$\begin{aligned} \beta_{abb}^2(l,m) &= k_0^2 \left\langle l,m \left| n^2(r) - n_0^2(r) \right| l,m \right\rangle && (5.16)\\ &= k_0^2 \left\langle l,m \left| \Delta n(r) \right| l,m \right\rangle && (5.17)\\ &= s\, k_0^2 \left\langle l,m \left| dn(r) \right| l,m \right\rangle && (5.18) \end{aligned}$$

Where $\langle l,m|$ is mode l,m in Dirac notation. Expanding this into integral form:

$$\beta^2_{abb}(l,m) \quad = \quad s\, k_0^2 \int_0^{2\pi} \mathrm{d}\theta \int_0^R r\, \mathrm{d}r \psi_{l,m} dn(r) \psi^*_{l,m} \tag{5.19}$$

We only investigate the effect of a radially symmetric aberration, and as such any angular dependence can be discarded.

$$\beta^2_{abb}(l,m) = s\, 2\pi k_0^2 \int_0^R \mathrm{d}r\; r R^2_{l,m}(r) dn(r)\;. \tag{5.20}$$

By definition, first order perturbation theory only incorporates a change in the propagation constants, but no coupling between the PIMs. In general, care must be taken when the system has degenerate states, such as in our case, where all modes that have the same combined mode number $|l| + 2m$ will have the same propagation constant. Therefore, these modes could be expected to couple strongly to each other. However, we only consider radially symmetric aberrations. Any modes that share the same combined mode number will have a different orbital angular momentum, and as such these modes will not couple for a circularly symmetric aberration.

5.4 MODEL VERIFICATION

Using our model it is possible to predict the transmission matrix of a perfectly straight waveguide that is perfectly aligned within the system, even in the case of refractive index profile aberrations. In order to verify that the observed behavior is supported by the model, we have to check that the proposed PIMs are indeed eigenmodes of the system. Therefore, we compute M and monitor its diagonality.

$$M = \Psi_d T^{\mathrm{meas}} \Psi_{\mathrm{p}}^{\dagger} = \Psi_d \left(\Psi_{\mathrm{d}}^{\mathrm{f}\dagger} M^{\mathrm{f}} \Psi_{\mathrm{p}}^{\mathrm{f}} \right)^{\mathrm{meas}} \Psi_{\mathrm{p}}^{\dagger} \tag{5.21}$$

Here, M is the extracted experimentally measured transmission matrix in a PIM basis, which in the ideal case will be a diagonal matrix. T^{meas} is the measured transmission matrix in a point basis, which can be expanded to $\left(\Psi_{\mathrm{d}}^{\mathrm{f}\dagger} M^{\mathrm{f}} \Psi_{\mathrm{p}}^{\mathrm{f}} \right)^{\mathrm{meas}}$, a transformation from fields to actual fibermodes ($\Psi_{\mathrm{p}}^{\mathrm{f}}$), which may or may not be the proposed PIMs, modal propagation through the fiber (M^{f}) and the inverse transformation into fields ($\Psi_{\mathrm{d}}^{\mathrm{f}}$). This is an important result: In order to test wether a particular set of modes are indeed propagation invariant eigenmodes, we perform a basis transformation into the predicted PIMs and confirm that the resulting matrix is indeed diagonal. When the proposed PIMs

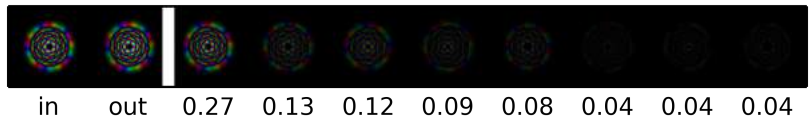

Fig. 5.5: Simulation of a waveguide presented with a perfectly sampled PIM ($l = 5, m = 5$), but displaced by 1% of the core diameter. Left: Input and output field after propagating through a fiber. Right: Decomposition of the output field into other modes with their relative coefficients, normalized to one.

are identical to the PIMs in the waveguide, $\Psi_d \Psi_d^{f\dagger}$ and $\Psi_p \Psi_p^{f\dagger}$ become identity matrices and M will equal M^f. This resembles finding the eigenvectors and eigenvalues of a matrix, but in this case the required eigenvectors are already known, and a standard diagonalization of T^{meas} would in general lead to a superposition of fiber eigenmodes which is dependent on the exact fiber length and on any misalignment parameters.

In order to excite just a single PIM, the waveguide has to be presented with a field with the exact matching spatial profile. In addition, the field has to be perfectly centered and there should be no tilt with respect to the waveguide axis. Unless all of these conditions are met, more than one waveguide will be excited and as such the system will appear to have modal coupling. However, this is an experimental inaccuracy rather than an indication of a faulty waveguide or an inaccurate estimation of fiber PIMs. For small misalignments, these kinds of modal couplings have even been used for cavity alignment [121]. A simulation of presenting a graded-index waveguide with an misaligned mode is shown in Fig. 5.5. In practice, it is usually not possible to align the imaging setup with sufficient accuracy that this kind of apparent mode coupling can be eliminated and as such an optimization technique is required to estimate the misalignments in the system based on the measured transmission matrix.

5.4.1 *Optimization of misalignment parameters*

To reconstruct misalignments in the optical setup, the experimentally measured transmission matrix is used as a feedback for an optimization technique. The optimization techniques employed in this section are covered extensively in Ref. [104]. A short overview is given here.

First of all, there are ten degrees of freedom in which the system can be misaligned, five on both ends:

- Position (3D): The center of the fiber might not coincide with

the estimated center of the waveguide, laterally or axially. These represent the first three degrees of freedom.

- Angle (2D) or tilt: The incidence angle of the light entering the waveguide might not be perfectly parallel to the fiber propagation direction, representing the last two degrees of freedom.

The algorithm that was employed to discover these misalignment parameters resembles a gradient-descent algorithm. Ψ_p is extended to $\Psi_p(\Delta r_p, \Delta\theta_p)$ accounting for a possible shift Δr_p and tilt $\Delta\theta_p$ of the proposed PIMs, and an analogous extension is made for Ψ_d. We then optimize these degrees of freedom in order to maximize the diagonality of matrix M^{meas} as defined by Eq. (5.21). To estimate the diagonality of the mode matrix, we observe the relative power on the diagonal of M.

$$P = \sum_i |M_{ii}|^2 \,/\, \sum_{i,j} |M_{ij}|^2 \tag{5.22}$$

The algorithm picks a misalignment parameter $(\Delta r_p, \Delta r_d, \Delta\theta_p, \Delta\theta_d)$ in a randomized order and attempts to find a new location that maximizes P. The PIMs are then resampled in the new set of misalignment parameters and the next misalignment parameter is optimized. Additionally, the steepness of the refractive index profile (b in Eq. 5.2) is not known with sufficient resolution. Therefore an additional optimization is run in which Ψ_p and Ψ_d are scaled in order to find the optimal steepness, but only after the performance metric P reaches a performance of about 20%. As with any gradient-descent optimization algorithm, it will only converge to a global optimum if the landscape is convex. It is very probable that faster solutions exist, or solutions that avoid getting stuck in local minima, and in Chapter 8 an alternative optimization method will be suggested. A discussion on the stability of the proposed solution is presented in Sec. 7.3. In principle, aberrations in the imaging system on either proximal or distal end, for instance caused by aberrations of the lenses employed for the imaging, could affect modal preservation as well, but they are presumed to be small.

5.4.2 *Optimizing refractive index aberrations based on measured transmission matrices*

After the final misalignment parameters have been found, the modal transmission amplitudes and phases are extracted from the diagonal of the extracted transmission matrix in a PIM basis.

$$A_{l,m}^{\text{meas}} \exp\left(\imath \phi_{l,m}^{\text{meas}}\right) = \text{diag}\,(M) \tag{5.23}$$

Here $A_{l,m}^{\text{meas}}$ are the transmitted amplitudes and $\phi_{l,m}^{\text{meas}}$ the wrapped modal phases that are extracted from M with the final misalignment parameters. These measured modal phases have to be matched to the model. Rather than attempting to unwrap ϕ_{lm}^{meas}, we look at the phasor sum of the phase difference between the estimated phases and the measured phases:

$$\text{PA}(L) = \left| \sum_i M_{ii} \exp\left(-i\beta_i L\right) \right|^2 / \left(\sum_i |M_{ii}| \right)^2 . \tag{5.24}$$

Here, PA is called the phase agreement normalized between zero and one, and L is the proposed fiber length. When the measured phases match the estimated phases, PA will be close to one, else it will be smaller. Eq. 5.24 is optimized subject to L to find an accurate estimate of the fiber length. In order to take refractive index profile aberrations into account, β_i has to take into account the refractive index profile aberrations. Therefore, we optimize

$$\text{PA}(L, \Delta n(r)) = \left| \sum_i M_{ii} \exp\left(-i(\beta_i + \delta\beta_i(\Delta n(r))L\right) \right|^2 / \left(\sum_i |M_{ii}| \right)^2 . \tag{5.25}$$

Here, $\delta\beta_i$ is the aberration induced additional propagation speed for the i-th l, m mode. A convenient set of basis functions for $\Delta n(r)$ should not contain any quadratic component that can be expressed by $n_0(r)$, and preferably it should be orthogonal when integrating over the cross section of the fiber. Therefore, we choose to employ radially symmetric orthogonal Zernike polynomials, as the lower two Zernike modes correspond to the refractive index profile itself and can easily be excluded.

This concludes a rather technical summary of the required mathematical toolbox in order to combine waveguide theory with complex photonics. In the next chapter these techniques will be used to verify a model that also predicts that these kind of fibers are much more resilient to bending, making them very suitable candidates for micro-endoscopy.

6

ROBUSTNESS OF LIGHT-TRANSPORT PROCESSES TO BENDING DEFORMATIONS IN GRADED-INDEX MULTIMODE WAVEGUIDES

Dirk E. Boonzajer Flaes, Jan Stopka, Sergey Turtaev, Johannes F. de Boer, Tomáš Tyc, Tomáš Čižmár

This chapter has been published as: "Boonzajer Flaes, D.E., Stopka, J., Turtaev, S., de Boer, J.F., Tyc, T., and Čižmár, T. (2018). Robustness of Light-Transport Processes to Bending Deformations in Graded-Index Multimode Waveguides. Phys. Rev. Lett. 120, 233901" [122]. The supplemental material is presented in the next chapter. As such, the references to the supplemental material have been replaced with the appropriate references to the appropriate sections in the next chapter. Other than that, no changes have been made to the original text save for the addition of section titles.

6.1 ABSTRACT

Light transport through a multimode optical waveguide undergoes changes when subjected to bending deformations. We show that optical waveguides with a perfectly parabolic refractive index profile are almost immune to bending, conserving the structure of propagation-invariant modes. Moreover, we show that changes to the transmission matrix of parabolic-index fibers due to bending can be expressed with only two free parameters, regardless of how complex a particular deformation is. We provide detailed analysis of experimentally measured transmission matrices of a commercially available graded-index fiber as well as a gradient-index rod lens featuring a very faithful parabolic refractive index profile. Although parabolic-index fibers with a sufficiently precise refractive index profile are not within our reach, we show that imaging performance with standard commercially available graded-index fibers is significantly less influenced by bending deformations than step-index types under the same conditions. Our work thus predicts that the availability of ultraprecise parabolic-index fibers will make endoscopic applications with flexible probes feasible and free from extremely elaborate computational challenges.

6.2 INTRODUCTION

With the availability of high-performance spatial light modulation, new imaging techniques based on holographic control of light through multimode fibers (MMFs) has emerged recently [103, 123, 124]. With extremely compact dimensions, MMF-based imaging techniques are particularly suited to various forms of endoscopy. Several techniques of endomicroscopy, especially laser-scanning-based approaches [91, 102] including multiphoton excitation [96], superresolution [90], as well as wide-field techniques such as bright-field, dark-field, and light-sheet microscopy [91–93], have already been demonstrated.

These approaches have been treating MMFs as random media [108, 125] and therefore they required a calibration step, in which the light transport through MMF is quantitatively analyzed. This is typically based on interferometric approaches [124] or by employing phase conjugation [101], and it consists of a sequence of measurements where the number of measurements exceeds the number of modes allowed to propagate through the MMF. These measurements then lead to the reconstruction of a transmission matrix (TM) [79, 124, 126, 127] – a linear relation between conveniently chosen representations of input and output modes containing the complete information about light transport through the MMF. During this procedure and subsequent imaging, the MMF is required to remain locked to the same position (contortion) since any deformation would introduce changes to the TM and as a result affect the imaging quality [91, 128, 129].

In 2015, it was shown that commercially available step-index MMFs, at length scales relevant for imaging applications, are of sufficient quality to allow for prediction of the TM based on numerical simulations [104]. Moreover, this study demonstrated that the influence of significant bending deformations can be theoretically predicted and taken into account in imaging applications. However, implementing such corrections is computationally very demanding and it requires very precise knowledge of the fiber layout.

In this work we show that employing MMFs with a perfect parabolic refractive index profile (PI) eliminates both of these problems. Unlike in step-index MMFs, bending of PI MMFs is not associated with cross-coupling of power between idealized propagation invariant modes (PIMs).

Moreover, the influence of bending is equivalent to a minuscule increase in fiber length to a good approximation, regardless of the radius of curvature and the length of the bent segment. The associated deformation operators describing the changes to the TM due to bending are diagonal in the representation of PIMs and commute with

one another. Therefore, the order of bends in the fiber is unimportant, and the deformation operatior for any three-dimensional adiabatic contortion of a PI MMF can be expressed upon the knowledge of only two parameters, one describing the overall curvature, the other the overall twist. Below we introduce a rigorous theoretical model for light propagation through PI-MMFs undergoing bending, which results in conservation of PIMs. We then experimentally verify conservation of PIMs using a large core parabolic-index medium with a high-quality refractive index pattern. Furthermore, we demonstrate that commercially available graded-index MMFs suffer from strong deviations from the parabolic refractive index profile. Finally, we demonstrate that even with the manufacturing imperfections, the imaging performance of graded-index MMFs is indeed significantly less affected by deformation when compared to step-index MMFs.

6.3 THEORETICAL CONSIDERATIONS

We consider an idealized fiber with cylindrically symmetric refractive index $n(r)$ satisfying

$$n^2(r) = n_0^2\left(1 - \frac{r^2}{b^2}\right), \tag{6.1}$$

where radial coordinate r extends to infinity. Here, n_0 is the refractive index on the axis and b is a scaling parameter. In real fibers, n becomes constant beyond a certain radius (in the cladding), which, however, affects only the highest order guided modes. Solving the scalar Helmholtz equation for a straight waveguide [116, 117] leads to identification of scalar PIMs as

$$\begin{aligned}\psi_{l,m}(r,\varphi,z) &= \sqrt{\frac{\alpha}{2\pi}\frac{2m!}{(m+|l|)!}}\exp\left(-\frac{\alpha r^2}{2}\right)\\ &\times \left(\alpha r^2\right)^{|l|/2} L_m^{|l|}(\alpha r^2)e^{il\varphi}\, e^{i\beta_{l,m}z}.\end{aligned} \tag{6.2}$$

Here, $L_m^{|l|}$ are associated Laguerre polynomials, $\alpha = kn_0/b$, $k = 2\pi/\lambda$ is the vacuum wave number, $l \in \mathbb{Z}$ is the orbital angular momentum (OAM) index of the PIM, and the index $m \in \mathbb{N}_0$ determines the number of radial nodes [106]. The propagation constants are

$$\begin{aligned}\beta_{l,m} &= \sqrt{k^2n_0^2 - 2\alpha(|l|+2m+1)}\\ &\approx kn_0 - \frac{|l|+2m+1}{b},\end{aligned} \tag{6.3}$$

where the approximation corresponds to the weak-guidance approximation [106].

As detailed in the Supplemental Material (Sec. 7.1), full vectorial solution of a fiber, uniformly bent in the xz plane with curvature ρ, leads to similar PIMs, but shifted towards the outer side of the bend, and with propagation constants modified as:

$$\begin{aligned}\beta'_{l,m,\sigma} &= kn_0\left(1+\frac{\rho^2 b^2}{2}\right)\\ &\quad -\left(\frac{1}{b}+\frac{9\rho^2 b}{4}\right)(|l|+2m+1)\\ &\quad -\frac{l\sigma+1}{2kn_0 b^2}\,,\end{aligned} \tag{6.4}$$

where $\sigma = \pm 1$ for the right- and left-handed circular polarization state, respectively, and making the same weak-guidance approximation as for Eq. (6.3). The first term is the same for all PIMs, corresponding just to an unimportant global phase. The mode-dependent phase change is given by the other two terms. The total phase accumulated by the PIM (l, m, σ) upon propagating the distance L in the fiber is $\beta'_{l,m,\sigma}L$; its mode-dependent part is

$$\phi = -L\left(\frac{1}{b}+\frac{9\rho^2 b}{4}\right)(|l|+2m+1) - \frac{L(l\sigma+1)}{2kn_0 b^2}\,. \tag{6.5}$$

The first part of the phase is the same as if the fiber were straight but of length $L' = L(1+9\rho^2 b^2/4)$ instead of L. On the other hand, the second part corresponding to spin-orbital interaction (SO) is the same as in a straight fiber of the original length L. To demonstrate that the effect of fiber bending is equivalent to a slight fiber stretching, we compare the phase ϕ with the phase ϕ' of the mode with the same indices (l, m, σ) in a straight fiber ($\rho = 0$) of length L'. The difference is

$$\phi - \phi' = \frac{9\rho^2 L(l\sigma+1)}{8kn_0}\,. \tag{6.6}$$

This difference becomes of order of π for fiber lengths of order of hundreds of meters for practical fibers and curvatures of order of cm^{-1}. The effect of bending is indeed equivalent to a slight increase of the fiber length, combined with a slight shift of the center of the PIMs towards the outer side of the bend. The spin-orbital interaction is typically much larger than the effect of the bend. For strong bending (the condition is given in Sec. 7.1) a solution in Cartesian coordinates would be required.

When the fiber is not bent uniformly but the curvature and the orientation of the curvature changes along the fiber, there may also be a torsion. Since the fiber deformation is a result of forces (or more precisely, torques) between neighboring parts of the fiber, these changes are not abrupt but smooth. Thanks to the adiabatically changing curvature, the PIMs are continuously adapting to the new bend conditions. Therefore, if we send an arbitrary PIM into one fiber end, its center will become shifted transversely from the fiber axis to different directions and by different amounts according to the actual fiber curvature, but its form will be retained. Therefore, the cross talk between the PIMs will stay very small. The effective length of the fiber is calculated by summing the effective lengths of infinitesimal fiber elements for which the curvature can be considered to be constant, which gives

$$L' = L + \frac{9b^2}{4} \int_0^L \rho^2(z)\,\mathrm{d}z\,. \tag{6.7}$$

In case of torsion, there will be an additional effect of geometric phase that will rotate the whole pattern by the angle corresponding to the solid angle swept by the fiber axis. For moderate curvatures, the influence of an arbitrary contortion is therefore governed by just two parameters: an effective change of fiber length and a rotation of the pattern.

6.4 EXPERIMENTAL RESULTS

Before attempting to verify the predicted behavior, we verify that the considered modes are indeed supported by the waveguide. We start with a 56–mm–long glass rod with a highly accurate parabolic index profile (PI rod), with a diameter of 350 µm and a numerical aperture of 0.12. To characterize the rod, a laser focus (circularly polarized, 1064 nm) is scanned over the proximal end of the rod using a spatial light modulator (SLM). The optical field leaving the distal end is captured (by means of phase-shifting interferometry using an external reference pathway [102, 124]) for every input position, schematically depicted in Fig. 6.1, and explained more thoroughly in Sec. 7.2. The resulting field is stored in the columns of a transmission matrix. For any incident field E_{in}, such as a PIM, the expected output field E_{out} is computed using $E_{\mathrm{out}} = \mathrm{TM} \cdot E_{\mathrm{in}}$ [79, 108, 113].

On the measured TM, we performed a basis transformation from the representation of points to the representation of PIMs, as defined by Eq. (6.2), shown in Fig. 6.1(a). As PIMs should remain conserved, this matrix should be diagonal. However, PIMs are very sensitive to alignment and mode preservation can only be expected for a perfectly

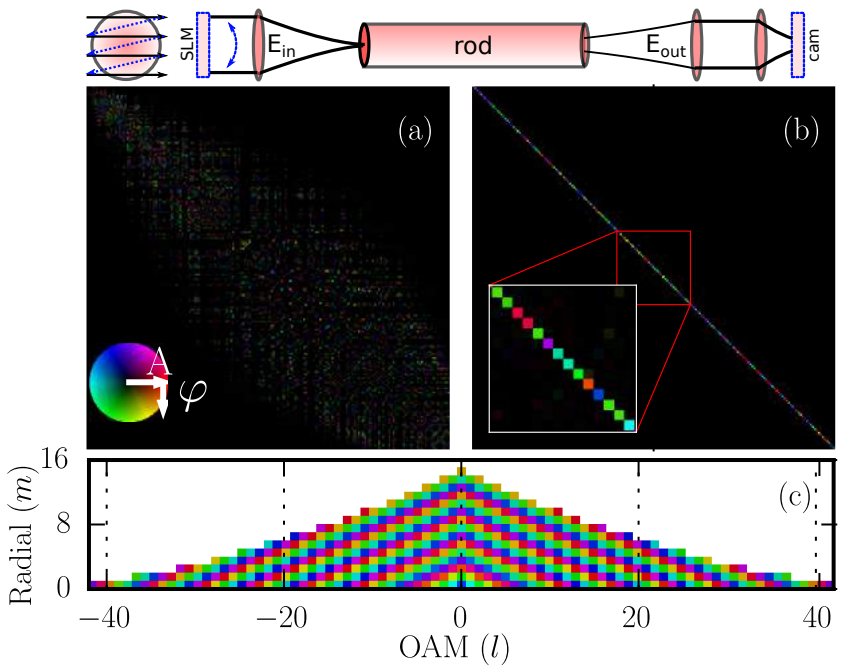

Fig. 6.1: Top: Diagram of transmission matrix measurement. A SLM is used to project a series of focal spots across a grid on the proximal end of the rod. The distal end output fields are measured and stored in the columns of a TM. (a) TM of the PI rod before numerical alignment, in a propagation-invariant mode (PIM) basis, ordered by l and then m in Eq. (6.2), as per Fig. 1(c) of Ref. [104]. Amplitude and phase color scale indicated in lower left. For clarity, only every third mode is displayed. (b) TM after numerical alignment. Inset shows zoomed in area around the diagonal, demonstrating that only the diagonal carries significant power. (c) Measured phases and amplitudes of PIMs.

aligned system. Further deviations are expected due to parameters of the rod being known with limited precision. While it is impossible to align the system with sufficient accuracy and ascertain refractive index profile parameters with sufficient precision, alignment errors and refractive index parameters can be corrected numerically through an optimization procedure (Ref. [104] and Sec. 7.3).

We optimized five degrees of freedom on both rod facets, three corresponding to the spatial location of the rod and two to the incidence angle. Lastly, we optimized the steepness of the refractive index profile (b), which determines the overall scaling of all PIMs.

After numerical optimization of the alignment parameters, Fig. 6.1(b), the TM in the PIM basis (M) appears to be diagonal, indicating almost no cross talk between the PIMs. The optimization procedure maximizes the relative power on the diagonal $P = \sum_i |M_{ii}|^2 / \sum_{i,j} |M_{ij}|^2$.

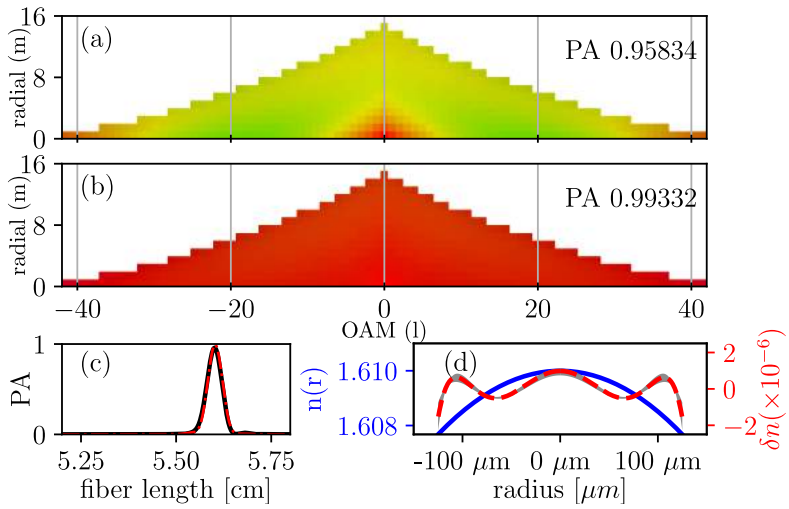

Fig. 6.2: (a) Modal phase difference between expected and measured PIMs after optimizing PI rod length, assuming a parabolic refractive index profile. PA is given in the figure. (b) Phase difference between expected modal phases and measured modal phases after fitting fine scale modulations to the refractive index profile. (c) PA as a function of rod length before (black) and after (red) optimizing refractive index profile. (d) Refractive index profile (blue), the detected perturbation (red), with 95% confidence interval indicated in gray, see Sec. 7.3. All color scales are the same as in Fig. 6.1.

Before alignment, P was only about 1.4%; however, after numerical optimization, P reached 95%. The overall phase delay measured of all different PIMs, which we call the modal phase, is plotted in Fig. 6.1(c). Modes with the same combined mode number $|l| + 2m + 1$ arrive with roughly the same modal phase, which is in accordance with the predicted propagation constants by Eq. (6.3).

Sampling all modes that are supported by the rod was unfeasible due to acquisition time. Therefore several selection criteria were applied, as explained in Sec. 7.2. Because the measured TM does not cover the full extent of the rod, some misalignment parameters can be coupled, depending on the waveguide length, which is discussed in Sec. 7.3.

To quantitatively evaluate the agreement between the measured and expected modal phases, the phase agreement was computed in the following way:

$$PA(L) = \left| \sum_i M_{ii} \exp\left(-i\beta_i L\right) \right|^2 / \left(\sum_i |M_{ii}| \right)^2 . \tag{6.8}$$

Here PA is the phase agreement, β_i is the expected propagation constant for the ith l, m mode, and L is the rod length. This quantity represents the squared ratio between the phasor sum and the amplitude sum of the modal phase differences. According to Eq. (6.3), the optimization procedure cannot optimize both L and n_0 simultaneously as their influence is indistinguishable. Therefore, only L was optimized and we used a fixed value for n_0 provided by the manufacturer.

Phase agreement reached 95.8% after optimizing L, with residual modal phase differences shown in Fig. 6.2(a). They are caused by small deviations to the refractive index profile from the parabolic refractive index profile.

To estimate this deviation, we employ first order perturbation theory to compute the altered propagation speeds for a refractive index profile with a small perturbation, and optimize the shape of this perturbation on phase agreement. As a convenient basis, we chose Zernike polynomials Z_4^0, Z_6^0 and Z_8^0. After optimization, PA exceeds 99.3%, with residual phase aberrations shown in Fig. 6.2(b). This results in a slightly different optimal rod length L [Fig. 6.2(c)]. The optimized refractive index profile is shown in Fig. 6.2(d). We can therefore conclude that for the PI rod the model agrees very well with the observed TM.

However, PI rods do not allow bending by a significant amount. To verify our bending predictions we progressed to a graded-index MMF. These fibers typically suffer from a dip in the refractive index profile near the core axis. We measured the TM of 20 mm of 50-µm-diameter graded-index MMF, using the same setup but with slightly altered imaging optics (see Table 7.1). The TM in PIM modes before and after alignment is shown in Figs. 6.3(a) and 6.3(b). Although the fiber is shorter, the refractive index profile is much steeper and so individual modes acquire larger phase differences (Sec. 7.2).

The optimization procedure increased the power preserved in PIMs from 5.4% to 53%, significantly less than could be measured for the PI rod. Analogous modal analysis of a step-index fiber showed over 95% conservation of modal power [104]. Repeating the experiment with longer fiber lengths did not significantly improve modal preservation. In Fig. 6.3, lower left, some typical fiber modes reveal that output modes are severely distorted. Low order radial PIMs perform better than higher order ones, especially those with a high orbital angular momentum, even though we suspect that they suffer from fiber ellipticity. Clearly, the optical performance of a 'real-life' graded-index fiber does not match the performance of a perfectly parabolic refractive index medium. We suspect that this is caused by imperfections in the refractive index profile of the GRIN MMF.

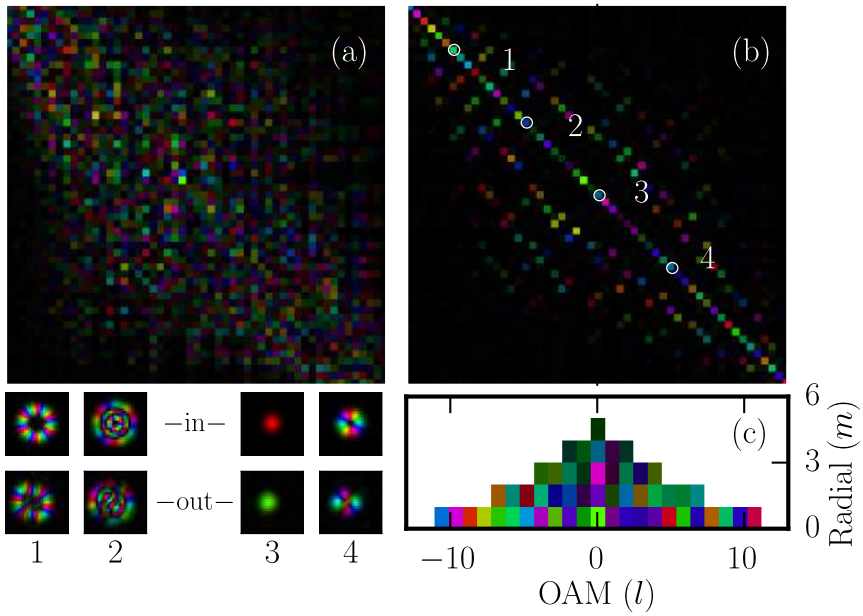

Fig. 6.3: Initial TM of the graded-index fiber in a PIM basis before (a) and after (b) the optimization procedure. (c) Measured phase retardations. Lower right: Predicted responses for the $(l,m) = (-6,0),(-3,2),(0,0)$ and $(2,0)$ modes at the output facet of the fiber. All color scales are the same as in Fig. 6.1.

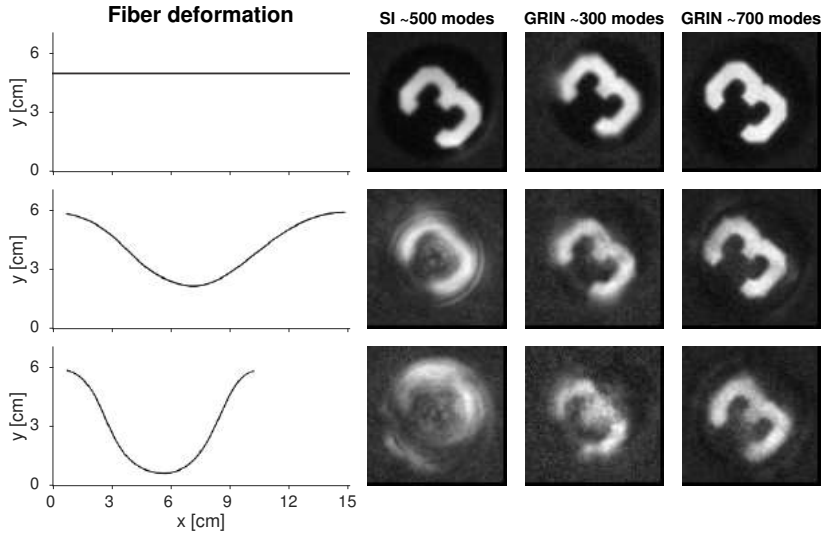

Fig. 6.4: Bending sensitivity of imaging performance for a step-index MMF and two different graded-index (GRIN) MMFs. The TM is measured for a straight fiber and used to image a sample object with three different fiber layouts.

Despite these deviations, the refractive index profile of such fibers is much closer to the parabolic distribution than step-index types, and shall exhibit better resilience to bending [130]. To verify this, we conducted a spot-scanning imaging experiment. The required input fields to scan a spot over the distal end of the fiber are measured for a straight fiber. Afterwards these input fields are projected and the total transmitted intensity through a transmissive part of a reflective sample inserted on the distal end is recorded. The fiber is then bent, but the input fields for a straight fiber are projected, repeating the imaging experiment as if no bending had taken place. Such an experiment was conducted for a step-index and two graded-index fibers with a comparable number of modes, shown in Fig. 6.4. This leads to severe imaging aberrations when employing the step-index MMF. However, the imaging performance is much less affected in the graded-index MMFs, where the fiber with a larger number of modes seems more bending resilient. The effective length increase according to Eq. 6.5 is only 17 µm, for the tight bend, too small for a significant effect in imaging. We attribute the decrease in imaging quality to limitations of the refractive index profile. Numerical simulations reveal that the effect becomes significant for longer fiber lengths (Sec. 7.4).

6.5 DISCUSSION

In this chapter we show that parabolic-index multimode fibers are very resilient to bending deformation. When bending curvatures are relatively small, our theoretical study indicates that all possible three-dimensional contortions can be expressed by two free parameters describing overall curvature and overall torque. The foundations of the theoretical model have been experimentally verified using a graded-index rod with a very precise refractive index profile. As this medium does not lend itself to bending deformations, we have progressed to analogous studies on commercially available fiber. These have indicated very strong deviations from the ideal parabolic refractive index profile, dramatically exceeding those of the graded-index rod as well as those observed in our previous studies in step-index fibers [104]. Since the insufficient quality of the fiber precluded a direct experimental verification of the bending resilience, we have provided a further semiempiric proof by studying the bending influence on the imaging quality achieved while using different types of fibers, clearly showing a superior performance of graded-index MMFs. This work thus demonstrates an urgent need to develop new graded-index MMFs with a higher–quality refractive index profile. This will enable numerous new possibilities in minimally invasive imaging, including highly advanced observations or optogenetic stimulation in awake and unrestrained animal models.

6.6 ACKNOWLEDGEMENTS

D. E. B. F. and J. F. de B. acknowledge support from the Netherlands Organisation for Scientific Research (NWO) with a Vici (JFdB) Grant No. 918.10.628. S. T. acknowledges funding from the EU FP7 People Programme (Marie Curie Actions) under REA Grant Agreement No. 608144. T. T. acknowledges support of Grant No. P201/12/G028 from the Czech Science Foundation.
T. T. and T. Č. acknowledge support from the European Regional Development Fund through Project No. CZ.02.1.01/0.0/0.0/15_003/0000476. T. Č. acknowledges European Research Council (ERC), Grant No. 724530, the University of Dundee, and Scottish Universities Physics Alliance (PaLS initiative) for financial support.

7

SUPPLEMENTAL MATERIAL GRADIENT-INDEX BENDING

Dirk E. Boonzajer Flaes, Jan Stopka, Sergey Turtaev, Johannes F. de Boer, Tomáš Tyc, Tomáš Čižmár

7.1 PROPAGATION INVARIANT MODES IN A BENT FIBER

To describe the effect of fiber bending on light modes propagating through a fiber quantitatively, we will initially consider scalar waves and account for polarization later. A scalar wave Ψ is governed by the Helmholtz equation $(\Delta + k^2 n^2)\Psi = 0$, where n is the refractive index. The wave can be separated as $\Psi = \psi(x, y)\exp(i\beta z)$, where z is the coordinate along the fiber axis, β is the propagation constant, and ψ is governed by the transverse equation

$$[\Delta_\perp + k^2 n^2 - \beta^2]\psi = 0\,. \tag{7.1}$$

Here $\Delta_\perp = \partial_x^2 + \partial_y^2$ denotes the transverse part of the Laplacian. For the parabolic refractive index profile, defined by Eq. (5.2), Eq. (7.1) separates both in Cartesian and polar coordinates. The PIMs separated in polar coordinates are given by Eq. (6.2) with propagation constants (5.6).

Now consider scalar waves in a uniformly bent fiber in the xz plane with curvature ρ, with the center of curvature at the point $(1/\rho, 0, 0)$. The local propagation constant is then no longer uniform across the fiber cross-section, but depends on x as $k_z(x) = \beta'/(1-\rho x)$, where β' is the propagation constant on the axis of the bent fiber [104]. Replacing β by $k_z(x)$ in Eq. (7.1) and using Eq. (5.2), we get the following equation for the bent fiber scalar PIMs:

$$\left[\Delta_\perp + k^2 n_0^2\left(1 - \frac{x^2+y^2}{b^2}\right) - \frac{\beta'^2}{(1-\rho x)^2}\right]\psi = 0\,. \tag{7.2}$$

If we make a substitution $x = x' - \Delta x$, where $\Delta x \equiv \beta'^2\rho/(\alpha^2 + 3\beta'^2\rho^2)$ and α is defined under Eq. (6.2), we get, after neglecting terms of the order ρ^4 and higher, the equation

$$\left[\Delta_\perp + k^2 n_0^2 - \alpha^2(x'^2 + y^2) - 3\beta'^2\rho^2 x'^2 + \frac{\beta'^4\rho^2}{\alpha^2} - \beta'^2\right]\psi = 0\,. \tag{7.3}$$

Eq. (7.3) corresponds in its form to Eq. (7.1) with x replaced by x', with β^2 replaced by $\beta'^2 - \beta'^4\rho^2/\alpha^2$, and with an additional term $3\beta'^2\rho^2x'^2\psi$. This shows that the effect of fiber bending is threefold. First, the center of the effective index profile is shifted in the negative x-direction (i.e., towards the outer side of the bend) by the distance Δx defined above; the modes in the bent fiber will, accordingly, also be shifted by Δx towards the outer side of the bend. Second, the steepness of the parabolic index profile in the x-direction gets slightly increased due to the additional term $3\beta'^2\rho^2x'^2$ in Eq. (7.3); for small curvatures ρ this term can be regarded as a perturbation. Third, there appears a term $\beta'^4\rho^2/\alpha^2$ that will lead to an additional shift of the propagation constants.

Next we have to account for the influence of light polarization. As it is well known, the polarization influences propagation constants, which is an effect known as spin-orbital (SO) interaction. For a straight fiber, the corresponding equation for electromagnetic waves still separates in cylindrical coordinates but no more in Cartesian ones. For the parabolic index profile (5.2) in the weakly-guided regime, the propagation constants (5.6) are shifted due to SO interaction by the amount [106]

$$\Delta\beta_{l,m,\sigma} = -\frac{l\sigma + 1}{2kn_0b^2}\,, \tag{7.4}$$

where $\sigma = \pm 1$ for the right- and left-handed circular polarization state, respectively.

Now if the fiber is bent, both effects of the SO interaction and the effective change of the refractive index described above are present simultaneously. For small curvatures, the SO interaction is dominant and the effect of fiber bending can be regarded as a small correction; then we can use perturbation theory of the first order to evaluate the effect of the additional term $3\beta'^2\rho^2x'^2$ in Eq. (7.3). For that, we need to evaluate the mean value of x'^2 for the LG PIMs. This can be done if we employ the equivalence of Eq. (7.1) with the stationary Schrödinger equation for a 2D harmonic oscillator with frequency α (when $\hbar$ and particle's mass are set to unity). Then the operator $\Delta_\perp - \alpha^2(x'^2 + y^2)$ in Eq. (7.3), up to the factor $-1/2$, is equal to the Hamiltonian $-\Delta_\perp/2 + \alpha^2(x'^2 + y^2)/2$ of a 2D harmonic oscillator with equilibrium position $(x, y) = (-\Delta x, 0)$. Now, by the virial theorem, the mean potential energy $\langle\alpha^2(x'^2 + y^2)/2\rangle$ comprises half of the oscillator total energy, i.e., of $\alpha(|l| + 2m + 1)$ in case of the LG state $|l, m\rangle$. Moreover, the probability distribution in the LG states is isotropic, so the energy is distributed equally between the x and y degrees of freedom. From

these facts we find that $\langle x'^2 \rangle = (|l| + 2m + 1)/(2\alpha)$. Going back to Eq. (7.3) and substituting the relevant terms, we get

$$k^2 n_0^2 - 2\alpha Q - \frac{3\beta'^2 \rho^2 Q}{2\alpha} + \frac{\beta'^4 \rho^2}{\alpha^2} - \beta'^2 = 0\,, \tag{7.5}$$

where we have denoted $Q = |l| + 2m + 1$ for convenience. When we solve this equation for β', neglect terms of the fourth order in ρ and take advantage of Eq. (5.6), we get finally for the propagation constants of the PIMs in the bent fiber

$$\beta' = \beta + \rho^2 \left(\frac{k n_0 b^2}{2} - \frac{9b(|l| + 2m + 1)}{4} \right), \tag{7.6}$$

where β is the propagation constant (5.6) of the PIM in the straight fiber with the same numbers l, m. Using Eq. (7.4) and expanding the square root, we can write the total propagation constant for the vector PIM (l, m, σ) as

$$\beta'_{l,m,\sigma} = k n_0 \left(1 + \frac{\rho^2 b^2}{2} \right) - \left(\frac{1}{b} + \frac{9\rho^2 b}{4} \right) (|l| + 2m + 1) - \frac{l\sigma + 1}{2 k n_0 b^2}\,. \tag{7.7}$$

We can also compare the order of correction to propagation constants due to bending and due to SO interaction. A simple analysis shows that the two corrections, namely $9\rho^2 b Q/4$ and $(l\sigma + 1)/(2kn_0 b^2)$, become comparable for curvatures of $\rho = 1/\sqrt{2kn_0 b^3}$, which is about $(1\text{ cm})^{-1}$ for a typical fiber. The above analysis is valid for curvatures smaller than this.

7.2 EXPERIMENTAL DETAILS

7.2.1 *Waveguide characteristics*

The PI-rod has been manufactured using a process where initially a glass rod is taken with a constant refractive index profile, which is then doped using a salt bath, resulting in a very smooth parabolic refractive index profile. The rod has a diameter of 350 µm (Selfoc LRL–035–P375–o–o–o–o), with a NA of 0.12. The manufacturer of the PI rod specifies that the quality of the refractive index profile goes down in the outer 20-30% of the rod.

The graded index fiber is a standard communication graded-index fiber, with an NA of 0.275, which is manufactured using an MCVD process, for which it is difficult to prevent a characteristic dip in the core of the refractive index profile.

Common optical components		
Item	**Part number**	
L1, L7, L8	A240TM-C	
L2	AC254-400-C-ML	
L3	AC254-300-C-ML	
L5	AC254-150-C-ML	
SMF	P1-980A-FC-1	
QWP1, QWP2	WPC10M-1064	
HWP	WPC10M-1064	
NPBS1, NPBS2	CM1-BS014	
M1-3	BB1-E03	
Altered optical components		
Item	**Fiber**	**Rod**
MMF/GL	GIF50C	LRL-035-P375
MO1	Plan N 20x	UPLSAPO 10x
MO2	Plan N 20x	Plan N 10x
L4	AC254-200-C-ML	AC254-150-C-ML
L6	AC254-150-C-ML	AC254-150-A-ML

Table 7.1: List of optics involved in the experiment. Common components have been listed in the top half, optics that were changed to measure either fiber or rod have been listed in the lower half. All part numbers except for the microscope objectives are Thorlabs part numbers. All microscope objectives were manufactured by Olympus.

Spot-scanning fibers		
Fiber	**Part number**	**# modes**
SI fiber	FG050UGA	500
GI fiber 1	GIF50C	300
GI fiber 2	GIF625	700

Table 7.2: Fibers employed for the spotscanning experiment as described in Fig. 6.4. All part numbers are Thorlabs part numbers.

Even though the rod (5.6 cm) is longer than the fiber (20 mm), the refractive index profile of the fiber is much steeper. To properly compare waveguide lengths we compare the modal phase difference between subsequent waveguides modes, which scales with L/b. When a pattern is projected on the proximal end of a graded-index medium, it is imaged again inside the rod after a length $2\pi b$, called the pitch length. The pitch length of the graded index rod is about 1.4 cm, whereas the pitch length of the fiber is about 1 mm. Therefore the rod is about 3.7 pitches long while the fiber is roughly 20 pitches long. For an ideal comparison, the waveguides would have been cut to the same pitch length. However, cutting a fiber of only a millimeter would have not been possible, and a rod with a length of roughly 28 cm would also be very difficult to handle or manufacture.

7.2.2 *Experimental setup*

The optical setup for the fiber analysis is analogous to the setup used in Ref. [104]. Since our study only exploits one circular polarization (which has been shown to remain conserved while light propagates through a fiber) our system only uses a single circular polarization pathway, which is shown in Fig. 7.1. There is a 45° rotation angle between the camera and the SLM, which is taken into account in the analysis. The SLM is located in the far-field of the frontal fiber facet. To measure the transmission matrix, a hologram is displayed on the SLM creating two points in the far-field, one of which is imaged onto the frontal fiber facet, called the scanning beam, while the other one is coupled into a single mode fiber and used as a reference. The scanning beam is sequentially repositioned across the facet of proximal end, and the resulting output field distribution is obtained by interfering the output field with a reference beam on the camera. More details on this procedure can be found in [104, 124]. As the number of scanning points is limited due to the relatively slow update rate of the SLM, the spacing of the focal points on the proximal end and the pixel size on the distal end have to be optimized for the medium under investigation, as explained below.

7.2.3 *Modal cutoff conditions*

To properly design the optical system required to characterize the waveguides, it is important to know the sampling requirements on the setup. This is determined by the number of modes that travel through the waveguide. While for a step-index fiber a clear cutoff of supported

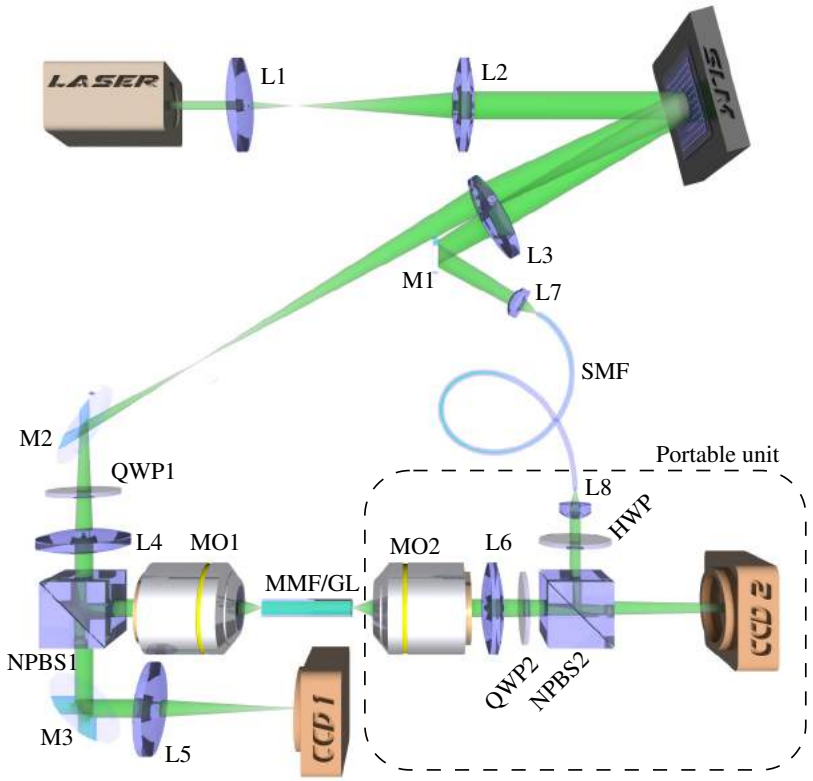

Fig. 7.1: Optical setup employed to measure transmission matrices. Electronic components: CCD 1 and 2: Basler piA640-210gm. SLM: Boulder Nonlinear Systems / Meadowlark Optics HSDPM512 DVI. Optical components are dependent on the MMF under investigation, and are listed in Table 7.1. When measuring the fiber, optics were present between L3 and L4 to control polarization of the input state, as in Ref. [104], which were not used and which are not shown. They did not support scanning a larger field of view, and have been removed for the rod measurements. To employ the system with a bent fiber, the imaging setup on the distal end is designed as a portable unit and can be moved on the table.

modes [106] can be defined, this is not obvious for a parabolic refractive index profile, extending to infinity. However, our waveguides have a finite spatial extent and as such the number of modes will be limited to modes that mainly travel within the core of the waveguide. PIMs that are very near the edge of the air–glass or core/cladding interface will likely be severely distorted. Therefore we confined the analysis to the central part of the rod only. To limit our analysis to modes that are properly guided, we demand that 99% of the amplitude of the mode falls within 75% of the core diameter in the case of the rod (the area with a high quality refractive index profile as specified by the manufacturer), and within the full core diameter in case of the fiber. In case of the graded index rod this means that the highest radial mode number we expect to be undistorted by boundary effects to be at $m_{\max} = 15$ for $l = 0$, and $|l_{\max}| = 44$ for $m = 0$, shown in Fig. 7.2, top.

7.2.4 *Optical design considerations*

Ideally, the transmission matrix should be measured with a large enough spatial extent and a sufficiently fine spacing that all the modes of interest up to and including $m_{\max}$ and $l_{\max}$ can be sampled and analyzed. However, with our current setup, this would result in a transmission matrix size that is not feasible due to technical limitations, mainly with respect to the acquisition time. The number of scanned points on the proximal end was limited to 85×85 points. Therefore, it is important to optimize the sampling area and pixel spacing of the transmission matrix measurement in such a way that the optimal amount of information can be extracted from the minimal number of measurements.

If a PIM is not properly sampled, the fiber is not presented with a perfect eigenmode. Similar to presenting the fiber with a misaligned mode, this will lead to apparent mode coupling, as discussed in the main article. In order to excite a given mode with sufficient resolution on the proximal end, and in order to detect a mode unambiguously on the distal end, similar selection criteria were employed as for determining the highest supported PIMs in the preceding section: The physical extent of the PIM needs to be sampled (real space condition), and this area has to be scanned with a sufficiently fine spacing that all features within the PIM are sufficiently expressed (Fourier space condition). To check the real space condition, a larger field of view was sampled, verifying that no more than 1% of the total amplitude of the PIM was present outside of the sampled area. To check the Fourier space condition, every mode was sampled at a half the pixel spacing, and the 2D fast Fourier transform (FFT) was computed. In this case, a

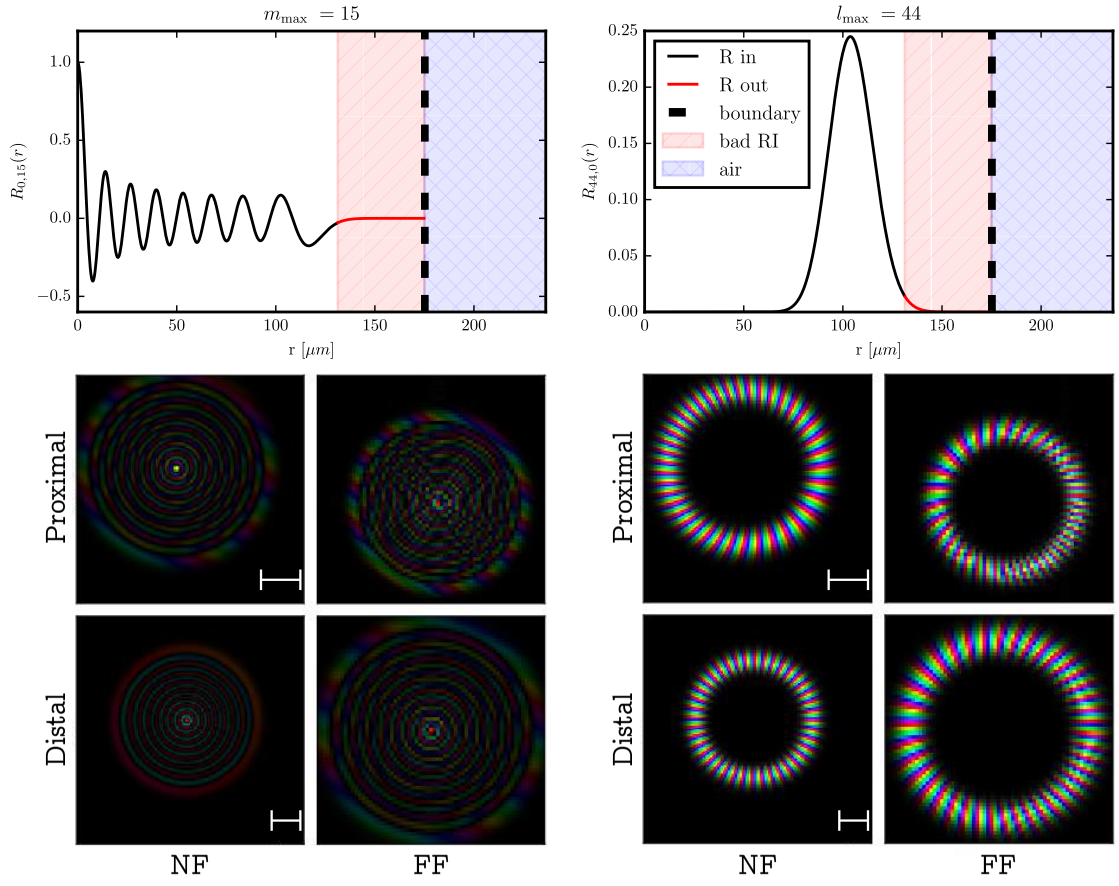

Fig. 7.2: Top: Radial part $R_{l,m}(r)$ of the highest supported radial (left) and angular (right) PIM for the graded-index rod. Blue shading indicates the area outside of the rod, red shading indicates the area with a low-quality refractive index profile. The black line indicates the amplitude of the radial part, red indicates the amplitude outside in the area with a low-quality refractive index. Bottom: Sampling of highest order radial (left; $l = 0, m = 13$) and angular (right; $l = 42, m = 0$) PIM included in the analysis after optimal alignment of the rod. Both groups of four represent the different constraints, and the black square indicates the area that has been sampled while measuring the transmission matrix. For both groups of four: Top left: PIM sampled on the proximal end of the fiber (real space constraint on proximal end) , Bottom left: same PIM sampled on the distal end of the fiber (real space constraint on distal end). Top right: Far-field of the PIM sampled on the proximal end (Fourier space constraint on proximal end). Bottom right: Far-field of the PIM sampled on the distal end (Fourier space constraint on distal end). For a PIM to be properly guided, it needs to fit within all of these images. In this case, the Fourier space constraint on the distal end is just met for the PIMs under investigation. Also, the PIMs hit the edge of our sampled domain on the proximal end. Scalebars represent $50\,\mu\mathrm{m}$.

mode was discarded if more than 1% of the total amplitude of the PIM was outside the area dictated by half the Nyquist frequency. The exact cutoff conditions are therefore dependent on the magnification of the imaging systems, and on the alignment parameters.

In order to optimize the design of the optical setup, for every available combination of lenses the number of modes that could be sampled and analyzed was computed, and the combination of optics that led to the highest number of excitable modes was used.

For the available combinations of optics, the optimal pixel pitch on the proximal end was 4.6 µm. On the distal end, the sampling was fixed at 6.2 µm, due to the curvature of the reference beam. The highest supported radial and angular PIM after optimizing alignment are shown in Fig. 7.2, bottom. In both cases the PIM approaches the edge of the scanned area by the SLM, as well as containing features which are too fine to be sampled properly on the camera.

Even though it was impossible to excite all supported PIMs, the final modal cutoff conditions for perfect alignment ran between $|l| = 42$ for $m = 0$, and $m = 13$ for $|l| = 0$. This represents a significant fraction of all the PIMs of interest.

7.3 OPTIMIZATION ALGORITHMS

7.3.1 *Misalignment parameters*

After measuring the transmission matrix in a point basis, the correct alignment parameters still have to be found in order to understand the transmission matrix in terms of PIMs. The optimization strategy is very similar to the one used in Ref. [104], but not identical. A brief overview of the procedure is given here and the differences are highlighted.

First, after measuring the transmission matrix TM in a point basis, the same method as described in the methods section of Ref. [104] was used for the initial alignment, resulting into a matrix of 3969 (63×63) input points by 4096 (64×64) output points for circular polarized light. Unlike the previous system, only a single polarization was taken into account. Therefore, spin-orbit interaction cannot be distinguished from a rotation between SLM and camera and it was not analyzed in the procedure.

Initially, after converting the TM into a mode basis, the power on the diagonal (modal performance) is still only around 1%, due to residual misalignment. Therefore, a separate alignment procedure is employed to find the optimal location and size of the PIMs. In total, this optimiza-

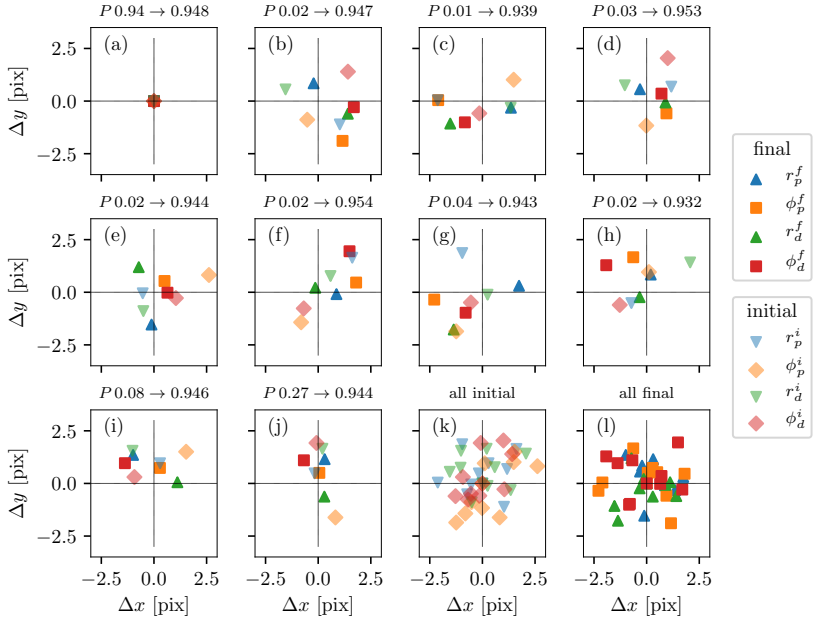

Fig. 7.3: Indication of stability of the solution to perturbing input misalignments, relative to the optimized position used in the paper. (a): Optimized alignment used in the further analysis. (b-j): Final alignment parameters after perturbing the final state in (a) by a total of 10 pixels, as discussed in the text. The initial and final performance P is printed on top of the figure. (k): All perturbed initial alignment parameters. (l): All final alignment parameters. Labels: r_p, r_d represent spatial alignment parameters on proximal and distal end, ϕ_p, ϕ_d are the angular misalignments. Even though the final P is on a similar level, different initial misalignment parameters lead to different final misalignment parameters.

tion procedure needs to find eleven parameters: waveguide location (3D) on proximal and distal end, and angle of incidence (2D) on proximal and distal end, and the overall steepness of the refractive index profile (1D). Instead of attempting to optimize all of these parameters at the same time, only the parameters corresponding to a particular domain, (for instance proximal position or distal angle) are optimized at the same time for reasons of computational efficiency. The procedure is iteratively repeated until it converges using a Nelder-Mead simplex algorithm. As this is a minimization algorithm, instead of the relative power on the diagonal P, $-P$ was used as a cost function. Previously P^{-1} was used. This was not seen to have any significant influence on the result. Also, previous work employed explicit minimization of PIMs close to the diagonal, which was not implemented in our analysis.

One of the challenges of the optimization routine is that it takes

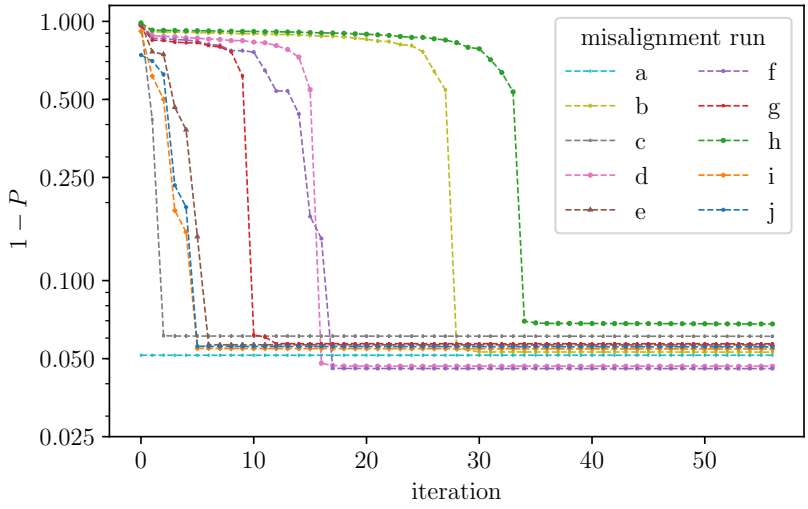

Fig. 7.4: Optimization trace for input misalignments (a-j) in Fig. 7.3. The performance is plotted after optimizing every invididual misalignment parameter. Even though there is a small variation in the number of steps required to find the misalignment, the final modal performances P are very similar.

very long to converge, especially if a lot of modes are involved. The previous routine attempted to optimize misalignment parameters using all supported PIMs at the same time, but we found that a reasonably accurate guess can be obtained by first selecting only a few low-order modes and doing a few rapid iterations based on those. Then the number of modes can be increased for a more accurate estimate. After every iteration, the l_{max} was increased by two and m_{max} by one until the sampling limit was reached. Optimizing the refractive index profile steepness was only started after 20 iterations of the optimization routine. Previously, the fiber parameters needed a different optimization metric in order not to lead to solutions featuring a small number of PIMs. This is not required for the analysis of the graded index waveguide.

As the modal cutoff conditions of the waveguide are determined by the pixel spacing it is important to be cautious about sampling artefacts, which could lead to apparent mode coupling. In previous work, all the modes were computed for a single location and shifting the center and tilt of all the modes was achieved using an interpolation matrix $\mathbf{C}$. This might lead to interpolation artefacts, however. Therefore we chose to sample the modes after every step of the iteration using Eq. (6.2).

Due to technical constraints with respect to the experimental setup, complete characterization of the rod was not possible, as the number

of modes that can propagate in the rod exceed the number of modes that we can analyze using our sampled transmission matrix. Therefore, some inaccuracy of the final misalignment parameters is to be expected, and multiple combinations of misalignment parameters can lead to similar performance. In order to give an idea of the accuracy of the reconstructed alignment parameters, we perturbed the final alignment parameters of the optimization routine in 2D, and ran the optimization routine again using the perturbed misalignment parameters as the initial locations. To keep the optimization time within a couple of hours, the sum of the disturbances was kept at 10 pixels. This is a large enough disturbance that P is initially only a few percent, but it is not so much disturbed that the optimization strategy takes more than an hour. If the system was fully determined, different initial conditions would lead to the same final conditions. However, as we show in Fig. 7.3 and 7.4, the final misalignment parameters differ for varying input misalignments.

The grin rod is acting like very good lens and as such, depending on the length or the rod, some of the misalignment parameters are coupled. For instance, if the waveguide were replaced with an imaging system imaging the frontal facet onto the distal facet, it would always be possible to shift the input modes by the same amount as the output modes, provided that the analyzed modes do not hit the edges of the lens. Therefore, when the lens is larger than the analyzed area there are multiple combinations of misalignment parameters that lead to very similar performance. Future research could exploit this ambiguity in order to come up with a faster optimization scheme. The final P is very similar (Fig. 7.4) and for our analysis this ambiguity is mainly an indication that the rod is of a very high optical quality.

7.3.2 *Changes to the refractive index profile optimization routine*

The procedure used to fit the refractive index profile abberations, as shown in Fig. 6.2, was nearly identical to the one used in Ref. [104]. For abberating functions, a basis of Zernike modes $Z_n(r/r_0)$ was employed, where r_0 is a scaling factor, fixed at 125 µm, the effective radius that was analyzed. We repeated the analysis for all the final locations indicated in Fig. 7.3. This only resulted in very small deviations in the resulting refractive index modulations, indicated in Fig. 7.5. The confidence interval was taken as two times the standard deviation in the individually optimized refractive index profiles.

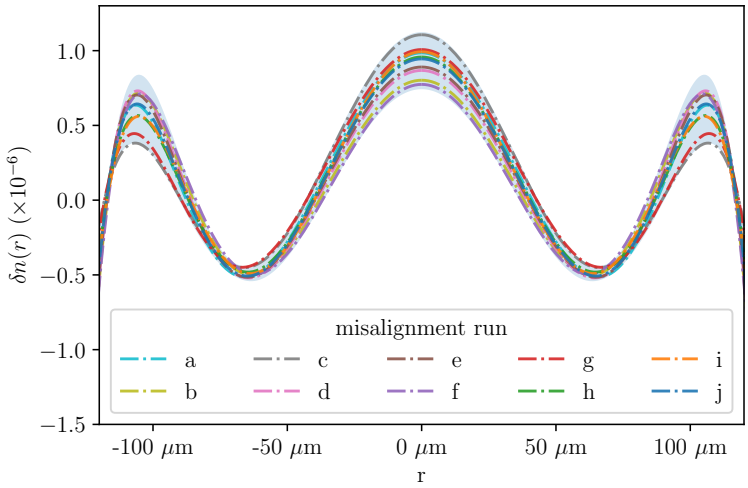

Fig. 7.5: Optimized refractive index profile differences for different optimization runs as described in Fig. 7.3. The shaded region indicates the 95% confidence interval. The final parameters have a small influence on the resulting refractive index profile.

7.4 SPOT-SCANNING EXPERIMENT

The experimental procedure for the spot-scanning experiment was identical to the one outlined in Ref. [104, Supplementary movie 7]. It consists of the following steps:

1. Using the setup in Fig. 7.1, acquire a transmission matrix T for the fiber, allowing for some room in between the distal end of the MMF and MO2 for later sample insertion.
2. Insert the sample (the transmissive part of a reflective USAF target) between MMF and MO2.
3. Using the SLM, display the required input fields (columns of $T^{\dagger}$) sequentially in order to scan a spot on the distal end of the fiber.
4. At every spot position, record the total transmitted intensity on CCD2 (sum of all camera pixel values).
5. Arrange the measured intensities by focal location, forming an image (Fig. 6.4).

As described in Ref. [104], it would also be possible to employ the only open port of NPBS1 to do "true" endoscopic imaging, but it requires careful calibration of the internal reflections in the setup, and it is not essential to demonstrate the bending sensitivity. To bend the fiber, the

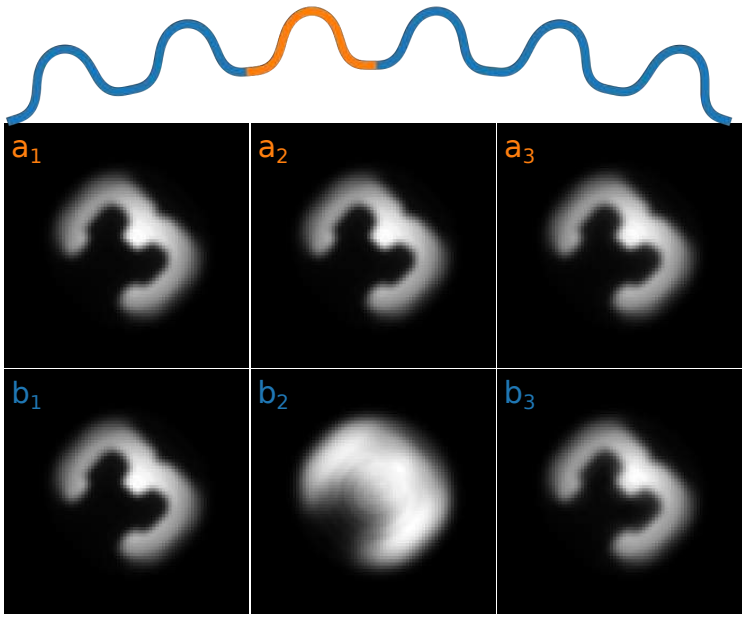

Fig. 7.6: Simulation of the scanning imaging experiment in Fig. 6.4, tight bend, for the fiber indicated as GRIN∼300 modes. Top: Indication of simulated fiber layout for the short fiber (the single orange sigment) and the long fiber (blue, six copies of the short segment). a_1: simulated imaging performance for a straight fiber, a_2: bent fiber using the straight fiber TM, a_3: imaging using the length correction described by Eq. (6.7). $b_{1,2,3}$: Same simulation for the long fiber. For the long fiber, the bending compensation clearly results in the restoration of the image quality.

portable unit in the setup can be moved towards MO1, and only the imaging experiment was repeated. The fiber parameters are shown in Table 7.2.

To compare the theoretical imaging performance with the experimental results for the strongest bend in Fig. 6.4, a mathematical simulation of imaging through a bent fiber is performed, by numerically reproducing the process of the scanning imaging experiment. The brightness of the i-th pixel of resulting image can be computed as

$$I_i = \left| PS^\dagger T' T^{-1} S v_i \right|^2 . \tag{7.8}$$

Here P is a binary mask representing the target, T is the calculated TM of the straight fiber in the PIM basis, T' is the calculated TM of the same fiber bent according to the experiment calculated in the basis of PIMs of the straight fiber, S is a matrix representing the transformation from the basis of focused spots into the basis of PIMs (the converse

transformation is represented by $S^{\dagger}$) and v_i is a vector in the basis of focused spots representing the spot at the position of i-th pixel.

The TM of the bent fiber T' is calculated as a product of 300 TMs of short segments of fiber with constant curvature. T can be modified to account for the effective length increase as described by Eq. (6.7). However, the effective length increase is only 17 µm, and as such the effect is minimal. Results of the simulation are shown in Fig. 7.6a. We attribute the decreased imaging performance observed in the experiment to imperfections in the refractive index profile. To demonstrate the expected performance of the bending correction for an ideal parabolic-index MMF, we simulate the imaging procedure for a longer fiber consisting of six identical copies of the short geometry, shown in Fig. 7.6b, using 1800 segments. In this case it is clear that the applied correction for the effective length increase leads to almost complete restoration of the original image quality.

8

IMPROVEMENTS ON THE MISALIGNMENT PARAMETER OPTIMIZATION ROUTINE

The optimization technique employed in the previous chapters to find misalignment parameters is very slow, requiring up to hundreds of hours of computation to converge. For practical applications that make use of the modal structure in a fiber, it would be very useful to have a faster optimization technique. In this section, we will first attempt to understand the current behavior of the optimization algorithm and then employ this knowledge to design a much faster routine.

All of the optimization traces in Fig. 7.4 show a sudden increase in performance, after which the performance level remains almost stationary. In these plots, the initial alignment location is already in the neighborhood of an optimum which was found earlier. When starting from the initial position, a long time is spent without a significant increase in modal performance, after which suddenly a sudden increase is found. It seems that the current optimization algorithm requires a very long time to reach the vicinity of the optimal location.

To better understand the current behavior of the optimization algorithm, it would be of great benefit to be able to map out the optimization landscape. The performance P is defined as $P = \sum_i |M_{ii}|^2 / \sum_{i,j} |M_{ij}|^2$, where M is the experimentally measured transmission matrix after transforming it into a mode basis based on the current estimate of the misalignment parameters. As there are ten spatial degrees of freedom, plotting the corresponding ten-dimensional landscape will not be feasible. However, our optimization routine only optimizes one location at a time: either position or angle on proximal or distal end. Therefore, P can be plotted when all parameters are kept constant except the alignment parameter of interest, which can aid us in understanding the behavior of the optimization routine.

A simplification of P can greatly reduce the required computation time to map out the optimization landscape. Instead of monitoring the relative power on the diagonal of M, we monitor the absolute power on the diagonal

$$P' = \sum_i |M_{ii}|^2 \ . \tag{8.1}$$

P' will have a similar performance as P when the misalignments are small relative to the waveguide diameter, as the denominator of P is fairly stable for misalignments. For small mismatches in fiber alignment, a misaligned PIM will mainly couple to neighboring PIMs with similar radial and angular mode indices [121]. Therefore, in general a mismatch in alignment parameters will lead to apparent coupling to other PIMs, including higher order PIMs. As long as these higher-order PIMs are sampled in the mode matrices Ψ_p and Ψ_d, the power will remain conserved. As such, the overall power in M, $\sum_{i,j} |M_{ij}|^2$ will remain stationary. However, for large misalignments the behavior of P and P' will be different.

The diagonal of M can be computed explicitly using

$$M_{ii} = \sum_{x,y} \Psi^*_{\mathrm{d},i}(x,y) E_{\mathrm{out},i}(x,y) \,, \tag{8.2}$$

where

$$E_{\mathrm{out},i} = T^{\mathrm{meas}} \Psi^\dagger_{\mathrm{p},i} \,. \tag{8.3}$$

Where the inner product is written explicitly, and x and y are the pixel coordinates. $\Psi_{\mathrm{p},i}$ is the i-th ψ_{lm} mode sampled on the proximal end, and $\Psi_{\mathrm{d},i}$ is the analogous mode on the distal end. To investigate the landscape of P', M_{ii} has to be computed for all shifts and tilts on the proximal and distal ends. Equation (8.2) can be expanded to take into account a misaligned fiber tilted with a steepness of (k_x, k_y) in the following way:

$$M_{ii}(k_x,k_y) = \sum_{x,y} \Psi^*_{\mathrm{d},i}(x,y) E_{\mathrm{out},i}(x,y) \times \exp\left(-\frac{2\pi\imath}{N}\left(k_x x + k_y y\right)\right) \,. \tag{8.4}$$

This is very similar to the definition of a discrete Fourier transform. For any discrete signal a_x sampled at positions x, the discrete Fourier transform is given by

$$A_k = \sum_{x=0}^{N-1} a_x \exp\left(-2\pi\imath \frac{xk}{N}\right) \tag{8.5}$$

where A_k is the discrete Fourier transform of a_x, k is the frequency index and N is the length of the signal. The extension to two-

dimensional Fourier transform is straightforward. In our case, $a_{xy} = \Psi^*_{\mathrm{d},i}(x,y)E_{\mathrm{out},i}(x,y)$, and M_{ii} can be rewritten for any tilt as

$$M_{ii}(k_x,k_y) = \mathcal{F}\left[\Psi^*_{id}(x,y)E_{\mathrm{out},i}(x,y)\right](k_x,k_y)\,, \tag{8.6}$$

where $\mathcal{F}[\cdot](k_x,k_y)$ indicates the 2D Fourier transform along the spatial coordinates, returning a function of variables k_x and k_y. As we expect the optimal misalignment to be somewhere in the neighborhood of the current location, and since the number of pixels in every image is quite limited, we will perform a discrete Fourier transform (DFT). Using Eq. (8.6), the optimization landscape $P'(k_x,k_y) = \sum_i \left|M_{ii}(k_x,k_y)\right|^2$ for the phase tilt on the distal end can be computed in a single operation, which only requires a few seconds on a standard laptop. Using the Fourier shifting theorem, Eq. (8.6) is extended to compute the performance for a shift on the distal end.

$$M_{ii}(\delta_x,\delta_y) = \mathcal{F}^{-1}\left[\left[\mathcal{F}\left[\Psi^*_{id}(x,y)\right]\mathcal{F}\left[E_{\mathrm{out},i}(x,y)\right]\right]\right](\delta_x,\delta_y) \tag{8.7}$$

Where $\mathcal{F}^{-1}[\cdot](\delta_x,\delta_y)$ represents the inverse Fourier transform along the angular coordinates k_y,k_x. This is very similar to frequency domain based subpixel image registration [59]. Essentially, M_{ii} is nothing else than the cross-correlation between the expected field exiting the fiber and the measured field for either a tilt or a shift. Equation (8.3) can be rearranged in order to compute the fitting landscape for tilts and shifts on the proximal end as well. In principle, it is possible to extend this method to take into account Fresnel propagation as well but this has not been implemented yet. In order to achieve a normalized score between zero and one, Ψ and E_{out} are divided by their l_2 norm. Therefore, P' equals the normalized cross-correlation between all expected and predicted PIMs averaged over all PIMs included in the analysis.

The fitting landscape for the distal tilt angle P' is shown in Fig. 8.1 for the graded-index rod analyzed in the preceding chapters. The waveguide is presumed to be centered in the sampled area, similar to the original location of the optimization algorithm. The defocusing parameters that were found in the original optimization routine have been employed. The most striking feature is that two peaks are visible instead of one. This is something we observe when more than one parameter is misaligned. As visualized in Fig. 8.1(a-c), the width of the peaks is dependent on the number of included modes. At the moment it is unclear why two maxima appear, but it seems that they are related to a discrepancy between the optimal location for modes with positive and negative orbital angular momentum, as shown in Fig. 8.1(d-f).

Knowledge of the optimization landscape now allows us to better understand the behavior of our original optimization routine. which

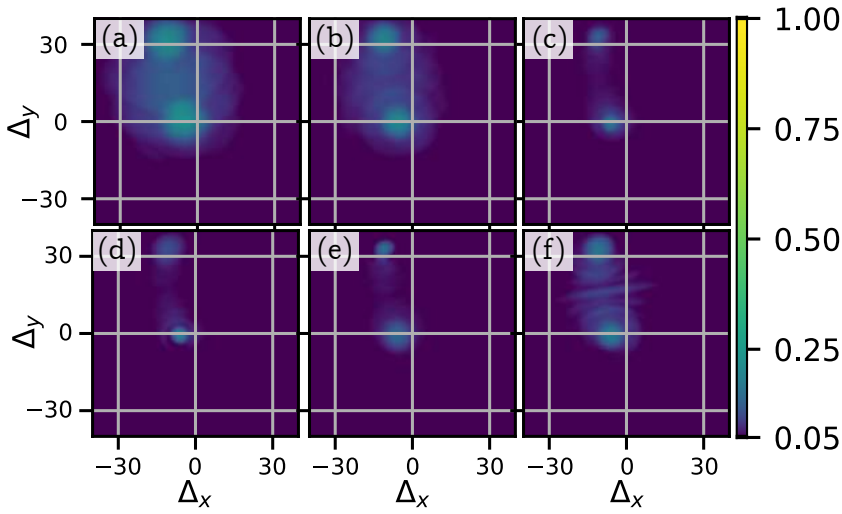

Fig. 8.1: Optimization landscape as defined by Eq. (8.1) for tilts ranging from -35 to +35 pixels on the distal end. The origin indicates the current performance, and any offset indicates the performance when the tilt on the proximal end is shifted by (Δ_x, Δ_y) pixels. All other parameters are fixed at the initial position in the center of the sampled domain. The shape of the landscape is determined by the modes included in the analysis. (a): Only modes with $Q = |l| + 2m + 1 < 5$ included. (b): $Q < 10$. (c): $Q < 63$. (d): Only modes with $l < 0$, $m < 14$. (e): Only modes with $l > 0$, $m < 14$. (f): Only modes with $l = 0$, $m < 14$.

optimizes a single alignment domain at a time. Therefore, excluding misalignment in the axial direction, it is essentially the same as mapping out the landscape, and moving to the closest peak. This behavior has been simulated and it is shown in Fig. 8.2. After the first two iterations, all misalignment locations are close to a local optimum, and the algorithm stagnates. After running 20 optimization iterations, the performance has not improved significantly, even though P' is only around 4%. The spacing between the different maxima does seem to gradually decrease, however. After a large number of iterations the different peaks will probably start to overlap, which is the moment at which the performance suddenly increases. However, this requires hundreds of iterations. Including a smaller number of modes in the analysis leads to broadened peaks in the optimization landscape and will likely increase the initial convergence speed.

The fundamental problem is that the optimization routine gets stuck in a local optimum from which it only slowly improves. Essentially, the only reason the algorithm converges is that the two peaks influence each other, as the tails of the peaks overlap with each others maxima, shifting the maximum location slightly in the direction of the other peak. To circumvent these local minima, all of the parameters could be

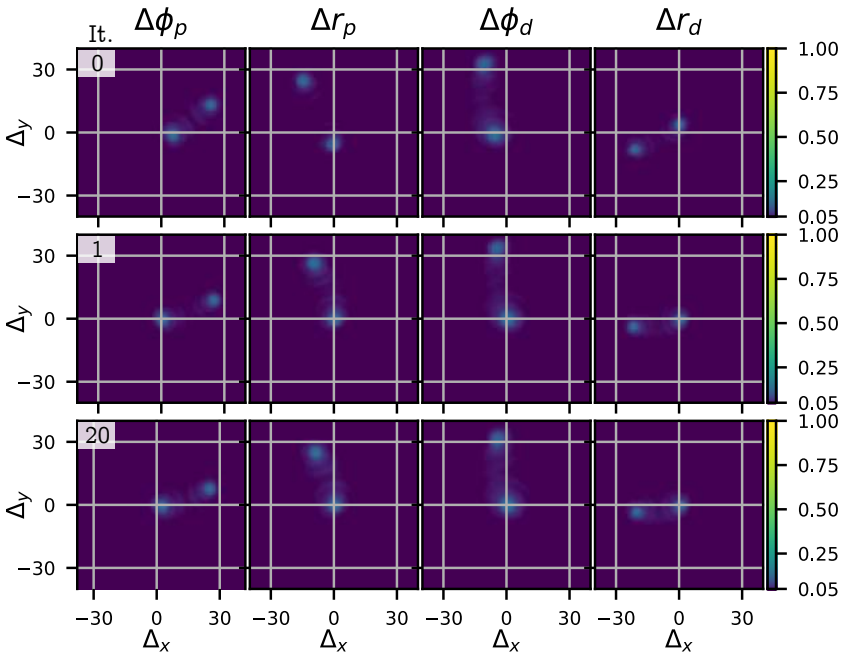

Fig. 8.2: Behavior of original optimization routine. Every row represents an iteration of the algorithm, indicated in the top left. From left to right: current fitting landscape for waveguide center (Δr_p) and tilt ($\Delta\phi_p$) at the proximal end, phase tilt ($\Delta\phi_d$) and center (Δr_d) at the distal end. In the first iteration, phase tilt on the proximal end is shifted to one of the local maxima. Afterwards, all misalignment parameters are close to a local optimum, and further iterations hardly change any alignment parameter. After 20 iterations, the two maxima in the fitting landscapes are slightly closer together. As such, it is probable that after a large number of iterations the maxima start to overlap.

optimized at the same time, but this is computationally demanding.

Access to the local fitting landscape can be employed to give a better estimate of the best step towards global optimization of the performance. Instead of attempting to optimize performance in a single domain, a step is computed that will move the fiber location in between the two peaks. This point is based on the optimal cross-correlation between the performance map and its mirror image for that particular misalignment parameter. As it is relatively fast to compute the fitting landscape, the required step can be computed for all misalignment parameters, yielding four different possible steps. The step that maximizes the improvement in performance with respect to the current location is selected. In this way, we favor optimizing a domain in which the two peaks are close together, or even a single peak, provided that it is not aligned properly already. The performance of this algorithm is shown in Fig. 8.3. Our new optimization routine only requires two

iterations to optimize the location, requiring only a few minutes to converge. For the first six iterations only the modes up to $(|l|, m) = (22, 10)$ are used, after which all modes up to $(|l|, m) = (42, 13)$ are included.

The final performance of the new algorithm is slightly worse than the original implementation as defined by P, and reaches a maximum around 85% modal conservation. Nevertheless, this could be achieved in only a few minutes, where the majority of the time was spent computing the mode matrices after every misalignment correction, which can be avoided. It is probable that a further improvement in performance can be obtained by employing a more careful stepsize and increasing the number of iterations. As such, real-time alignment starts to be feasible where after acquisition of a transmission matrix only a few minutes are required to optimize the alignment.

A number of improvements can still be made to reach a performance level similar to the original algorithm. First of all, the determination of which alignment step to take can probably be improved. Furthermore, the expected modal phases could be incorporated in P', which might alleviate the twin peak problem. A careful selection of which fiber modes to include in the alignment could possibly enable another order-of-magnitude improvement convergence speed , as especially the highest order modes represent a tight confinement.

Essentially, the optimization routine outlined here is based on image registration between the expected image and the image predicted by the transmission matrix. Initial simulations seem to suggest that a system could be designed that enables on-line alignment of the fiber parameters without requiring any interferometric stability. A mode is projected on the proximal end of the fiber, and the intensity of the resulting field is recorded at the distal fiber facet and in the far-field of the distal fiber facet. Based on the similarity between the measured intensity and the modeled intensity for a number of modes, the misalignment parameters can be reconstructed.

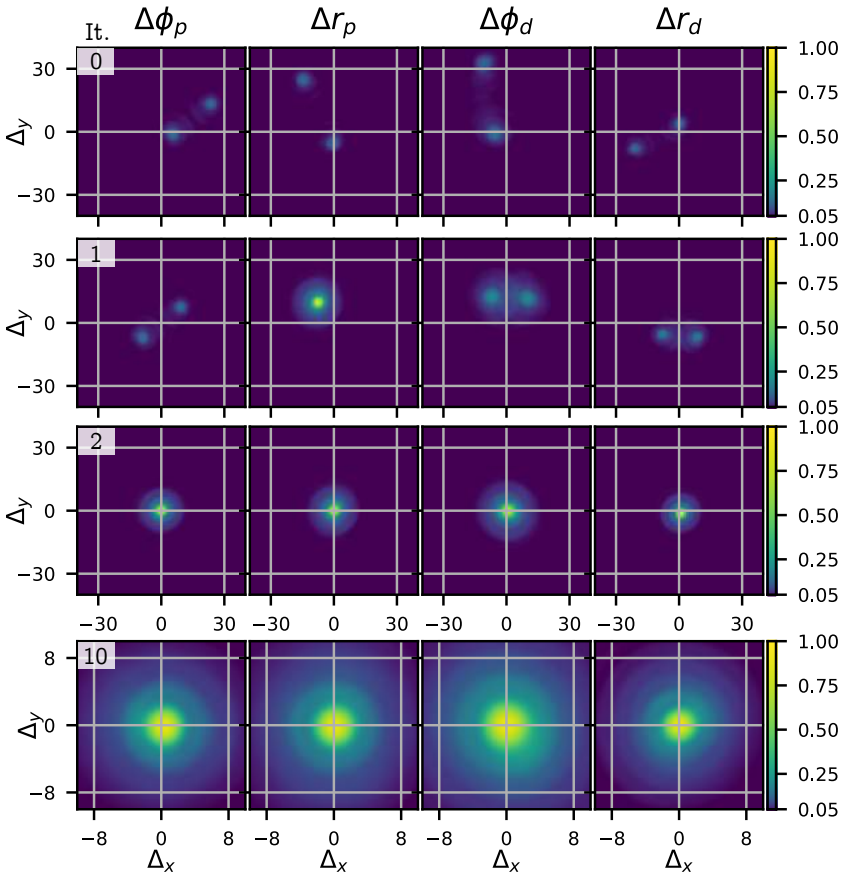

Fig. 8.3: Performance of the new optimization routine as discussed in the text. . Rows represent the performance after 0, 1, 2, and 10 iterations, indicated in the top left corner. At iteration 0, the phase tilt on the proximal end is adjusted to center the two peaks around the origin. Afterwards, only the center on the proximal end still has to be centered. For iterations 1-5, only modes up to $|l|, m = 22, 10$ are used to speed up computing the mode matrices. Afterwards, all modes are employed. The final performance reached $P = 87.2\%$ after 10 iterations.

BIBLIOGRAPHY

[1] M. R. Teague, *J. Opt. Soc. Am.* **1983**, *73*, 1434–1441 (cit. on pp. 2, 13).

[2] J. Frank, S. Altmeyer, G. Wernicke, *J. Opt. Soc. Am. A* **2010**, *27*, 2244–2251 (cit. on pp. 2, 6).

[3] J. R. Fienup, *Appl. Opt.* **1982**, *21*, 2758–2769 (cit. on pp. 2, 8, 13).

[4] B.-Z. Dong, Y. Zhang, B.-Y. Gu, G.-Z. Yang, *J. Opt. Soc. Am. A* **1997**, *14*, 2709–2714 (cit. on p. 2).

[5] S. Marchesini, H. He, H. N. Chapman, S. P. Hau-Riege, A. Noy, M. R. Howells, U. Weierstall, J. C. H. Spence, *Phys. Rev. B* **2003**, *68*, 140101 (cit. on pp. 2, 38).

[6] J. M. Rodenburg, H. M. Faulkner, *Appl. Phys. Lett.* **2004**, *85*, 4795–4797 (cit. on pp. 2, 8, 38).

[7] V. Elser, *arXiv:math/0111080* **2001** (cit. on pp. 2, 8).

[8] J. Zhong, L. Tian, P. Varma, L. Waller, *IEEE Trans. Comput. Imaging* **2016**, *2*, 310–322 (cit. on pp. 2, 39).

[9] F. Zernike, *Physica* **1942**, *9*, 974–986 (cit. on p. 3).

[10] R. Allen, G. David, *Z. Für Wiss. Mikrosk. Mikrosk. Tech.* **1969**, *69*, 193–221 (cit. on p. 3).

[11] P. Gao, B. Yao, I. Harder, N. Lindlein, F. J. Torcal-Milla, *Opt. Lett.* **2011**, *36*, 4305–4307 (cit. on p. 3).

[12] T. H. Nguyen, M. E. Kandel, M. Rubessa, M. B. Wheeler, G. Popescu, *Nat. Commun.* **2017**, *8*, 210 (cit. on p. 3).

[13] G. Popescu, L. P. Deflores, J. C. Vaughan, K. Badizadegan, H. Iwai, R. R. Dasari, M. S. Feld, *Opt. Lett.* **2004**, *29*, 2503–2505 (cit. on p. 3).

[14] Z. F. Phillips, M. Chen, L. Waller, *PLOS ONE* **2017**, *12*, e0171228 (cit. on p. 3).

[15] M. K. Kim in *Digital Holographic Microscopy*, Springer Series in Optical Sciences, Springer, New York, NY, **2011**, pp. 149–190 (cit. on p. 3).

[16] J. Goodman, *Introduction to Fourier Optics*, W. H. Freeman, **2005** (cit. on p. 4).

[17] E. Cuche, F. Bevilacqua, C. Depeursinge, *Opt. Lett. OL* **1999**, *24*, 291–293 (cit. on pp. 5, 13, 43).

[18] E. Cuche, P. Marquet, C. Depeursinge, *Appl. Opt.* **2000**, *39*, 4070 (cit. on p. 5).

[19] T. Tahara, T. Kanno, Y. Arai, T. Ozawa, *J. Opt.* **2017**, *19*, 065705 (cit. on p. 5).

[20] D. Gabor, *Proc. R. Soc. Math. Phys. Eng. Sci.* **1949**, *197*, 454–487 (cit. on pp. 5, 10).

[21] K. Khare, P. T. S. Ali, J. Joseph, *Opt. Express* **2013**, *21*, 2581–2591 (cit. on p. 6).

[22] J. R. Fienup, *Appl. Opt.* **2013**, *52*, 45–56 (cit. on pp. 6, 8, 38).

[23] J. Bertolotti, E. G. van Putten, C. Blum, A. Lagendijk, W. L. Vos, A. P. Mosk, *Nature* **2012**, *491*, 232–234 (cit. on p. 6).

[24] H. Yilmaz, E. G. van Putten, J. Bertolotti, A. Lagendijk, W. L. Vos, A. P. Mosk, *Optica* **2015**, *2*, 424 (cit. on p. 6).

[25] A. Drémeau, A. Liutkus, D. Martina, O. Katz, C. Schülke, F. Krzakala, S. Gigan, L. Daudet, *Opt. Express* **2015**, *23*, 11898 (cit. on pp. 6, 67).

[26] V. Elser, I. Rankenburg, P. Thibault, *PNAS* **2007**, *104*, 418–423 (cit. on p. 6).

[27] G. Liu, P. D. Scott, *J. Opt. Soc. Am. A* **1987**, *4*, 159 (cit. on p. 6).

[28] J. R. Fienup, *Opt. Lett.* **1978**, *3*, 27–29 (cit. on pp. 6, 11, 38).

[29] D. W. Noom, D. E. Boonzajer Flaes, E. Labordus, K. S. Eikema, S. Witte, *Opt. Express* **2014**, *22*, 30504–30511 (cit. on pp. 6, 12, 38).

[30] A. M. Maiden, J. M. Rodenburg, *Ultramicroscopy* **2009**, *109*, 1256–1262 (cit. on pp. 6, 43).

[31] A. Maiden, D. Johnson, P. Li, *Optica* **2017**, *4*, 736 (cit. on pp. 6, 41, 42).

[32] J. Qian, C. Yang, A. Schirotzek, F. Maia, S. Marchesini, *Inverse Probl. Appl. Contemp Math* **2014**, *615*, 261–280 (cit. on p. 6).

[33] M. Stockmar, P. Cloetens, I. Zanette, B. Enders, M. Dierolf, F. Pfeiffer, P. Thibault, *Sci. Rep.* **2013**, *3* (cit. on pp. 6, 38).

[34] L. J. Allen, M. P. Oxley, *Opt Commun.* **2001**, *199*, 65–75 (cit. on pp. 6, 8, 13).

[35] R. Saxton, W. Gerchberg, *OPTIK* **1972**, *35*, 237–246 (cit. on p. 8).

[36] J. R. Fienup, C. C. Wackerman, *J. Opt. Soc. Am. A* **1986**, *3*, 1897–1907 (cit. on p. 8).

[37] P. Bao, F. Zhang, G. Pedrini, W. Osten, *Opt. Lett.* **2008**, *33*, 309 (cit. on p. 8).

[38] D. W. E. Noom, K. S. E. Eikema, S. Witte, *Opt. Lett.* **2014**, *39*, 193–196 (cit. on pp. 8, 13, 14, 25, 38).

[39] P. Thibault, A. Menzel, *Nature* **2013**, *494*, 68–71 (cit. on pp. 8, 35, 39).

[40] J. Rodenburg, A. Hurst, A. Cullis, *Ultramicroscopy* **2007**, *107*, 227–231 (cit. on pp. 8, 41).

[41] G. Corkidi, B. Taboada, C. D. Wood, A. Guerrero, A. Darszon, *Biochemical and Biophysical Research Communications* **2008**, *373*, 125–129 (cit. on p. 11).

[42] L. Tian, J. Wang, L. Waller, *Opt. Lett.* **2014**, *39*, 1326 (cit. on p. 12).

[43] I. Sencan, A. F. Coskun, U. Sikora, A. Ozcan, *Sci. Rep.* **2015**, *4* (cit. on p. 12).

[44] G. Zheng, S. A. Lee, Y. Antebi, M. B. Elowitz, C. Yang, *PNAS* **2011**, *108*, 16889–16894 (cit. on pp. 12, 50).

[45] W. Bishara, T.-W. Su, A. F. Coskun, A. Ozcan, *Opt. Express* **2010**, *18*, 11181 (cit. on pp. 12, 50).

[46] O. Mudanyali et al., *Lab. Chip* **2010**, *10*, 1417– (cit. on p. 12).

[47] A. Greenbaum, A. Ozcan, *Opt. Express* **2012**, *20*, 3129–3143 (cit. on p. 13).

[48] T. E. Gureyev, S. Mayo, S. W. Wilkins, D. Paganin, A. W. Stevenson, *Phys. Rev. Lett.* **2001**, *86*, 5827–5830 (cit. on p. 13).

[49] K. A. Nugent, *J. Opt. Soc. Am. A* **2007**, *24*, 536–547 (cit. on p. 13).

[50] D. W. E. Noom, D. E. Boonzajer Flaes, E. Labordus, K. S. E. Eikema, S. Witte, **2014**, Media 1, DOI 10.1364/OE.22.030504.m001 (cit. on p. 15).

[51] D. W. E. Noom, D. E. Boonzajer Flaes, E. Labordus, K. S. E. Eikema, S. Witte, **2014**, Media 2, DOI https://doi.org/10.1364/OE.22.030504.m002 (cit. on p. 16).

[52] D. W. E. Noom, D. E. Boonzajer Flaes, E. Labordus, K. S. E. Eikema, S. Witte, **2014**, Media 3, DOI https://doi.org/10.1364/OE.22.030504.m003 (cit. on p. 18).

[53] H. Kogelnik, T. Li, *Appl. Opt. AO* **1966**, *5*, 1550–1567 (cit. on p. 18).

[54] H. A. Ilhan, M. Doğar, M. Özcan, *J. Microsc.* **2014**, *255*, 138–149 (cit. on p. 25).

[55] Z. Ren, Z. Xu, E. Y. Lam, *Optica OPTICA* **2018**, *5*, 337–344 (cit. on p. 26).

[56] M. Sanz, J. A. Picazo-Bueno, J. García, V. Micó, *Opt. Express* **2015**, *23*, 21352–21365 (cit. on pp. 28, 38).

[57] M. Sanz, J. Á. Picazo-Bueno, L. Granero, J. García, V. Micó, *Sci. Rep.* **2017**, *7*, 43291 (cit. on pp. 28, 33).

[58] M. Odstrcil, P. Baksh, S. A. Boden, R. Card, J. E. Chad, J. G. Frey, W. S. Brocklesby, *Opt. Express* **2016**, *24*, 8360 (cit. on pp. 28, 43).

[59] M. Guizar-Sicairos, S. T. Thurman, J. R. Fienup, *Opt. Lett.* **2008**, *33*, 156 (cit. on pp. 29, 45, 57, 105).

[60] L. Loetgering, R. Hammoud, L. Juschkin, T. Wilhein, *EPL* **2015**, *111*, 64002 (cit. on p. 29).

[61] For Instance, OmniVision OV2744, http://www.ovt.com/sensors/OV2744, **2018** (cit. on p. 29).

[62] G.-Z. Yang, B.-Z. Dong, B.-Y. Gu, J.-y. Zhuang, O. K. Ersoy, *Appl. Opt. AO* **1994**, *33*, 209–218 (cit. on p. 33).

[63] L. Waller, M. Tsang, S. Ponda, S. Y. Yang, G. Barbastathis, *Opt. Express* **2011**, *19*, 2805 (cit. on p. 33).

[64] D. J. Batey, PhD thesis, University of Sheffield, **2014** (cit. on pp. 35, 50).

[65] L.-H. Yeh, J. Dong, J. Zhong, L. Tian, M. Chen, G. Tang, M. Soltanolkotabi, L. Waller, *Opt. Express* **2015**, *23*, 33214 (cit. on p. 36).

[66] D. E. Boonzajer Flaes, S. Witte, *Opt. Express* **2018**, *26*, 31372 (cit. on p. 38).

[67] I. Yamaguchi, T. Zhang, *Opt. Lett.* **1997**, *22*, 1268–1270 (cit. on pp. 38, 48).

[68] W. Harm, C. Roider, A. Jesacher, S. Bernet, M. Ritsch-Marte, *Opt. Express* **2014**, *22*, 22146–22156 (cit. on p. 38).

[69] R. M. Clare, M. Stockmar, M. Dierolf, I. Zanette, F. Pfeiffer, *Opt. Express* **2015**, *23*, 19728 (cit. on p. 38).

[70] F. Zhang et al., *Opt. Express* **2013**, *21*, 13592–13606 (cit. on pp. 39, 46, 57).

[71] P. Dwivedi, S. Konijnenberg, S. Pereira, P. Urbach, *Ultramicroscopy* **2018**, DOI 10.1016/j.ultramic.2018.04.004 (cit. on pp. 39, 46, 57).

[72] N. Burdet, X. Shi, D. Parks, J. N. Clark, X. Huang, S. D. Kevan, I. K. Robinson, *Opt. Express* **2015**, *23*, 5452 (cit. on pp. 39, 42).

[73] P. Li, T. Edo, D. Batey, J. Rodenburg, A. Maiden, *Opt. Express* **2016**, *24*, 9038–9052 (cit. on p. 39).

[74] L. Loetgering, H. Froese, T. Wilhein, M. Rose, *Phys. Rev. A* **2017**, *95*, DOI 10.1103/PhysRevA.95.033819 (cit. on pp. 39, 45).

[75] M.-C. Zdora, P. Thibault, T. Zhou, F. J. Koch, J. Romell, S. Sala, A. Last, C. Rau, I. Zanette, *Phys. Rev. Lett.* **2017**, *118*, DOI 10.1103/PhysRevLett.118.203903 (cit. on p. 39).

[76] C. Falldorf, C. von Kopylow, R. B. Bergmann, *J. Opt. Soc. Am. A* **2013**, *30*, 1905 (cit. on pp. 39, 58).

[77] A. M. Maiden, M. J. Humphry, F. Zhang, J. M. Rodenburg, *J. Opt. Soc. Am. A* **2011**, *28*, 604–612 (cit. on pp. 39, 50).

[78] J. Vargas, J. A. Quiroga, T. Belenguer, *Opt. Lett.* **2011**, *36*, 1326 (cit. on pp. 43, 57).

[79] S. M. Popoff, G. Lerosey, R. Carminati, M. Fink, A. C. Boccara, S. Gigan, *Phys. Rev. Lett.* **2010**, *104*, 100601 (cit. on pp. 48, 78, 81).

[80] T. Čižmár, M. Mazilu, K. Dholakia, *Nat. Photonics* **2010**, *4*, 388–394 (cit. on p. 48).

[81] M. G. L. Gustafsson, *J. Microsc.* **2000**, *198*, 82–87 (cit. on p. 50).

[82] M. Lei, X. Zhou, D. Dan, J. Qian, B. Yao in Frontiers in Optics 2016 (2016), Paper FF3A.5, Optical Society of America, **2016**, FF3A.5 (cit. on p. 50).

[83] P. Rathert, W. Lutzeyer, W. E. Goddwin, *Urology* **1974**, *3*, 113–118 (cit. on p. 62).

[84] S. Sivankutty, V. Tsvirkun, G. Bouwmans, D. Kogan, D. Oron, E. R. Andresen, H. Rigneault, *Opt. Lett.* **2016**, *41*, 3531–3534 (cit. on p. 63).

[85] V. Tsvirkun, S. Sivankutty, G. Bouwmans, O. Katz, E. R. Andresen, H. Rigneault, *Opt. Lett.* **2016**, *41*, 4771–4774 (cit. on p. 63).

[86] Y. Komachi, H. Sato, K. Aizawa, H. Tashiro, *Appl. Opt.* **2005**, *44*, 4722 (cit. on p. 63).

[87] A. Orth, M. Ploschner, I. S. Maksymov, B. C. Gibson, *Opt. Express* **2018**, *26*, 6407–6419 (cit. on p. 63).

[88] D. B. Conkey, N. Stasio, E. E. Morales-Delgado, M. Romito, C. Moser, D. Psaltis, *J. Biomed. Opt.* **2016**, *21*, 045002 (cit. on p. 63).

[89] F. Wang, H. S. S. Lai, L. Liu, P. Li, H. Yu, Z. Liu, Y. Wang, W. J. Li, *Opt. Express* **2015**, *23*, 16803–16811 (cit. on p. 63).

[90] G. P. J. Laporte, N. Stasio, C. Moser, D. Psaltis, *Opt. Express* **2015**, *23*, 27484 (cit. on pp. 63, 78).

[91] T. Čižmár, K. Dholakia, *Nat. Commun.* **2012**, *3*, 1027 (cit. on pp. 63, 64, 78).

[92] Y. Choi, C. Yoon, M. Kim, T. D. Yang, C. Fang-Yen, R. R. Dasari, K. J. Lee, W. Choi, *Phys. Rev. Lett.* **2012**, *109*, 10.1103/PhysRevLett.109.203901 (cit. on pp. 63, 64, 78).

[93] M. Plöschner, V. Kollárová, Z. Dostál, J. Nylk, T. Barton-Owen, D. E. K. Ferrier, R. Chmelík, K. Dholakia, T. Čižmár, *Sci. Rep.* **2015**, *5*, 18050 (cit. on pp. 63, 78).

[94] F. Akhoundi, Y. Qin, N. Peyghambarian, J. K. Barton, K. Kieu, *Biomed. Opt. Express* **2018**, *9*, 2326–2335 (cit. on p. 63).

[95] N. V. Kuzmin, P. Wesseling, P. C. d. W. Hamer, D. P. Noske, G. D. Galgano, H. D. Mansvelder, J. C. Baayen, M. L. Groot, *Biomed. Opt. Express* **2016**, *7*, 1889 (cit. on p. 63).

[96] E. E. Morales-Delgado, D. Psaltis, C. Moser, *Opt. Express* **2015**, *23*, 32158 (cit. on pp. 63, 78).

[97] T. A. Murray, M. J. Levene, *J. Biomed. Opt.* **2012**, *17*, 021106 (cit. on p. 63).

[98] M. J. Booth, B. R. Patton in *Fluorescence Microscopy*, (Eds.: A. Cornea, P. M. Conn), Academic Press, Boston, **2014**, pp. 15–33 (cit. on p. 64).

[99] M. J. Booth, *Philos. Trans. R. Soc. Lond. Math. Phys. Eng. Sci.* **2007**, *365*, 2829–2843 (cit. on p. 64).

[100] F. Bortoletto, C. Bonoli, P. Panizzolo, C. D. Ciubotaru, F. Mammano, *PLoS ONE* **2011**, *6*, e22321 (cit. on p. 64).

[101] I. N. Papadopoulos, S. Farahi, C. Moser, D. Psaltis, *Opt. Express* **2012**, *20*, 10583–10590 (cit. on pp. 64, 78).

[102] S. Bianchi, R. D. Leonardo, *Lab Chip* **2012**, *12*, 635–639 (cit. on pp. 64, 78, 81).

[103] R. N. Mahalati, R. Y. Gu, J. M. Kahn, *Opt. Express* **2013**, *21*, 1656–1668 (cit. on pp. 64, 72, 78).

[104] M. Plöschner, T. Tyc, T. Čižmár, *Nat. Photonics* **2015**, *9*, 529–535 (cit. on pp. 66, 68, 74, 78, 82, 84, 87, 88, 92, 93, 96, 99, 100).

[105] Z. H. Wang, H. Zhang, J. P. Meunier, *Microw. Opt. Technol. Lett.* **2003**, *37*, 433–436 (cit. on p. 66).

[106] A. . Snyder, J. Love, *Optical Waveguide Theory*, 1st ed., Springer, **1983** (cit. on pp. 66, 68, 69, 79, 80, 89, 94).

[107] J. P. Meunier, J. Pigeon, J. N. Massot, *Opt. Quantum Electron.* **1981**, *13*, 71–83 (cit. on pp. 66, 72).

[108] I. M. Vellekoop, A. P. Mosk, *Opt. Lett.* **2007**, *32*, 2309–2311 (cit. on pp. 67, 78, 81).

[109] T. R. Hillman, T. Yamauchi, W. Choi, R. R. Dasari, M. S. Feld, Y. Park, Z. Yaqoob, *Sci. Rep.* **2013**, *3*, DOI 10.1038/srep01909 (cit. on p. 67).

[110] M. Kim, W. Choi, Y. Choi, C. Yoon, W. Choi, *Opt. Express* **2015**, *23*, 12648 (cit. on p. 67).

[111] S. M. Popoff, G. Lerosey, R. Carminati, M. Fink, A. C. Boccara, S. Gigan, *Phys. Rev. Lett.* **2010**, *104*, 100601 (cit. on p. 67).

[112] E. G. van Putten, A. P. Mosk, *Physics* **2010**, *3*, DOI 10.1103/Physics.3.22 (cit. on p. 67).

[113] J. Yoon, K. Lee, J. Park, Y. Park, *Opt. Express* **2015**, *23*, 10158–10167 (cit. on pp. 67, 81).

[114] M. Plöschner, B. Straka, K. Dholakia, T. Čižmár, *Opt. Express* **2014**, *22*, 2933–2947 (cit. on p. 67).

[115] D. Marcuse, *J. Opt. Soc. Am.* **1978**, *68*, 103–109 (cit. on p. 68).

[116] D. Gloge, *Appl Opt.* **1971**, *10*, 2252–2258 (cit. on pp. 68, 79).

[117] E. Snitzer, *J Opt Soc Am* **1961**, *51*, 491–498 (cit. on pp. 68, 79).

[118] D. Gloge, *Appl. Optics* **1971**, *10*, 2252–2258 (cit. on p. 69).

[119] E. Snitzer, *J. Opt. Soc. Am.* **1961**, *51*, 491–498 (cit. on p. 69).

[120] E. Khular, A. Kumar, A. K. Ghatak, B. P. Pal, *Opt Commun.* **1977**, *23*, 263–267 (cit. on p. 72).

[121] D. Z. Anderson, *Appl. Opt.* **1984**, *23*, 2944 (cit. on pp. 74, 104).

[122] D. E. Boonzajer Flaes, J. Stopka, S. Turtaev, J. F. de Boer, T. Tyc, T. Čižmár, *Phys. Rev. Lett.* **2018**, *120*, 233901 (cit. on p. 77).

[123] R. D. Leonardo, S. Bianchi, *Opt. Express* **2011**, *19*, 247–254 (cit. on p. 78).

[124] T. Čižmár, K. Dholakia, *Opt Express* **2011**, *19*, 18871–18884 (cit. on pp. 78, 81, 92).

[125] I. M. Vellekoop, A. Lagendijk, A. P. Mosk, *Nat Photon* **2010**, *4*, 320–322 (cit. on p. 78).

[126] J. Carpenter, B. J. Eggleton, J. Schröder, *Opt. Express* **2014**, *22*, 96–101 (cit. on p. 78).

[127] S. Popoff, G. Lerosey, M. Fink, A. C. Boccara, S. Gigan, *Nat Commun* **2010**, *1*, 81 (cit. on p. 78).

[128] S. Farahi, D. Ziegler, I. N. Papadopoulos, D. Psaltis, C. Moser, *Opt Express* **2013**, *21*, 22504–22514 (cit. on p. 78).

[129] D. Loterie, D. Psaltis, C. Moser, *Opt. Express* **2017**, *25*, 6263 (cit. on p. 78).

[130] A. M. Caravaca-Aguirre, R. Piestun, *Opt. Express* **2017**, *25*, 1656 (cit. on p. 86).

ACCEPTED PUBLICATIONS

[1] D. W. Noom, D. E. Boonzajer Flaes, E. Labordus, K. S. Eikema, S. Witte, *Opt. Express* **2014**, *22*, 30504–30511.

[2] D. E. Boonzajer Flaes, J. Stopka, S. Turtaev, J. F. de Boer, T. Tyc, T. Čižmár, *Phys. Rev. Lett.* **2018**, *120*, 233901.

[3] D. E. Boonzajer Flaes, S. Witte, *Opt. Express* **2018**, *26*, 31372.

9

ABSTRACT

The microscope is one of the most influential scientific instruments developed to date. Since the invention of the device around 1600 by among others Dutch amateur optician Antoni van Leeuwenhoek, its impact on research over a great variety of academic disciplines has been second to none. The essential idea behind the microscope remains virtually unchanged over the past 400 years: one or more lenses are employed in order to project an enlarged image of the specimen of interest onto a detector. Traditionally this detector was the eye of the observer, but nowadays a camera has become the standard. Apart from a steady improvement in lens quality and the use of cameras rather than direct observation by the eye, we still use the microscope as it was invented four centuries ago. One of the many virtues of a microscope is that it does not presume many stringent properties of the specimen under observation. It can be any color, composition or form – but it must be thin and it must have contrast. A slice, rather than a chunk.

So even this hugely popular device has its drawbacks. The first has to do with the nature of many biological samples: in sliced form they are more or less transparent, and do not produce a useful picture. There are two ways to overcome this problem. The traditional way is staining the specimen with contrasting liquid. There are well known limitations and drawbacks to this system however. A more recent method is to base the image on the phase of the light exiting the sample, rather than the intensity. Obtaining quantitative phase information can be challenging however, and requires an expensive setup. Another limitation is the requirement that the focal plane should be decided upon before imaging. There is no way the focal plane can be changed or adapted once the image has been obtained, unless quantitative phase measurements have been obtained.

First part of the thesis: lensless imaging

In the first part of this thesis, we will explore two setups as an alternative to the traditional microscopy described above. These alternatives provide specific advantages as well as new limitations when compared to regular microscopy. The common ground of both approaches is that no lenses are involved. Using different wavelengths The first setup

makes use of illuminating a sample at three different wavelengths with three different lasers. The diffracted light is captured on a camera chip, without any intermediate lenses involved. From the three images, a picture of the object is reconstructed using a computer algorithm. This enables an extremely simple, low-cost and portable microscope. As the focusing distance is simply a parameter of the reconstruction algorithm, it can be chosen afterwards. We have shown that we can produce live images of a biological specimen with a resolution of up to two micrometers.

A limitation in this setup is that it requires achromatic samples - samples that appear the same for all wavelengths. Therefore, a thin slice of a plant root or a young nematode can be reconstructed, but an older nematode or a flower with lots of brilliant colours will not work. In the next chapter we discuss and show a different setup, which does not rely on illuminating with multiple wavelengths. In this case, a grating is employed to project a series of stripes across the object. The relative position of the stripes and the orientation of the stripes is changed, and a number of acquisitions are obtained. Once more, these individual images hardly resemble the object, and we developed a computer algorithm to reconstruct these measurements into a single object estimate. Once more, we show a setup capable of reaching a resolution of around two micrometer. However, this technique is rather slow to implement and as such it should mainly be seen as a proof that illuminating with an interference pattern is sufficient to reconstruct a large and extended object.

Multimode fiber endoscopy

The second part of this thesis is devoted to exploring the practical use of lensless imaging by applying the principle to minimally invasive imaging in the form of endoscopy. A classical microscope can probe the surface of a sample, but probing inside samples forms a challenge. The light reflected from deeper layers of the sample is scattered by the upper layers that it has to travel through on its way to the lens of the microscope. Although various techniques have been developed to increase the depth of field and to compensate for scattering induced by the top layers of the sample, the imaging depth with a traditional microscope is still limited to at most a few centimeters.

To image deep inside sensitive but remote areas, such as the brain or the heart, an endoscope is inserted. Here the challenge is to minimize the damage induced by this probe, by making it very small in diameter. Most modern endoscopes consist of a miniaturized version of a microscope, where a tiny lens and a tiny imaging chip are placed

on the distal end of the endoscope. The resulting image is then electronically transmitted to a screen, to be viewed by the operator. The lens and imaging chip can not be miniaturized further than roughly a millimeter however. There is no conceivable way at present to further decrease the footprint of an endoscope – unless the lens and imaging chip are left out.

As a radically new design, we explored employing a multimode optical fiber as a very thin endoscope. A multimode optical fiber is able to guide light to the area of interest, and to guide the captured light back to the optical setup, which can then be placed outside the body. Provided that the exact optical characteristics of the fiber are known, imaging at the distal end can be performed in various ways.

When an image is projected onto one end of the fiber, it will come out distorted even after a few millimeters of propagation. A crude way of understanding this behavior is that a standard fiber (a step-index fiber) relies on total internal reflection. Light rays entering the fiber reflect from the boundaries of the fiber and end up with the same angle as they entered but in a randomized position and orientation. All of these rays interfere, creating a complicated pattern that we call a speckle pattern. Reconstructing an image purely based on the speckle pattern is a challenge. Careful calibration does not solve the bending problem In order to perform an imaging experiment through such a device, the optical behavior of the fiber could be carefully calibrated, using a setup on the distal end of the fiber. As soon as the optical behavior of the device is accurately known, imaging can be performed in a number of ways. However, the exact optical properties depend strongly on the exact way in which the fiber is bent and twisted (the so called contortion of the fiber). Therefore, problems tend to arise in a practical setting, because the way that the fiber is bent is not known before it is inserted into the body. The case for parabolic refractive index profile fibers Trying to overcome this issue, we used multimode optical fibers which are designed in a different way. We found that a particular class of fibers, called parabolic refractive index profile fibers, are almost immune to bending.

Therefore, it should be possible to calibrate a straight piece of fiber and then bend the fiber without affecting the imaging performance. In practice however, the refractive index profile of these fibers turned out to be of insufficient quality to verify our predictions in a quantitative way. However, we were able to analyze a rigid rod with an accurate refractive index profile which confirmed the theory really well.

Future developments

The techniques employed in the first part of this work could eventually be combined with the results about bending properties as described and analyzed in the second part. This, however, will be a topic for further research.

10 ACKNOWLEDGMENTS

The acknowledgements section is not included in the online version of this document.

COLOPHON

This document was typeset using `classicthesis` style developed by André Miede. The style was inspired by Robert Bringhurst's seminal book on typography *"The Elements of Typographic Style"*. It is available for LaTeX and LyX at https://bitbucket.org/amiede/classicthesis/.

Employed open-source software

A lot of this research would have been a lot harder had it not been for the terrific open source scientific ecosystem available nowadays. All of the data analysis that I have performed was written in Python, and I used a lot of open-source packages. It is my personal opinion that most of them absolutely outperform their commercial counterparts and I am very grateful for all these volunteers who have made my PhD so much more enjoyable in the background. Although I cannot remember all of the packages I either learnt from or was helped by, the main software packages that I have used are listed below.

Package/program name	Available at
Python	https://www.python.org/
Scipy	https://www.scipy.org/
Scikits-imaging	http://scikit-image.org/
Numpy	http://www.numpy.org/
OpenCV	https://opencv.org/
Git	https://git-scm.com/
PyOpenCL	https://documen.tician.de/pyopencl/
PyCUDA	https://documen.tician.de/pycuda/
LyX	https://www.lyx.org/
PyQTGraph	http://www.pyqtgraph.org/
Jupyter notebook	https://jupyter.org/
pyfits	https://pythonhosted.org/pyfits/